THE UNIVERSITY *of* EDINBURGH

Osmosis: a Molecular Dynamics Computer Simulation Study

Thomas Lion

Doctor of Philosophy
The University of Edinburgh
July 2013

Abstract

Osmosis is a phenomenon of critical importance in a variety of processes ranging from the transport of ions across cell membranes and the regulation of blood salt levels by the kidneys to the desalination of water and the production of clean energy using potential osmotic power plants. However, despite its importance and over one hundred years of study, there is an ongoing confusion concerning the nature of the microscopic dynamics of the solvent particles in their transfer across the membrane. In this thesis the microscopic dynamical processes underlying osmotic pressure and concentration gradients are investigated using molecular dynamics (MD) simulations.

I first present a new derivation for the local pressure that can be used for determining osmotic pressure gradients. Using this result, the steady-state osmotic pressure is studied in a minimal model for an osmotic system and the steady-state density gradients are explained using a simple mechanistic hopping model for the solvent particles. The simulation setup is then modified, allowing us to explore the timescales involved in the relaxation dynamics of the system in the period preceding the steady state. Further consideration is also given to the relative roles of diffusive and non-diffusive solvent transport in this period.

Finally, in a novel modification to the classic osmosis experiment, the solute particles are driven out-of-equilibrium by the input of energy. The effect of this modification on the osmotic pressure and the osmotic flow is studied and we find that active solute particles can cause reverse osmosis to occur. The possibility of defining a new "osmotic effective temperature" is also considered and compared to the results of diffusive and kinetic temperatures.

Declaration

I declare that this thesis was composed by myself, that the work contained herein is my own except where explicitly stated otherwise in the text, and that this work has not been submitted for any other degree or professional qualification except as specified.

Parts of this work have been published in Lion and Allen (2012) [83] and Lion and Allen (2012) [84].

(*Thomas Lion, July 2013*)

Acknowledgements

The work completed during the course of this thesis would not have been possible were it not for the support and guidance of many individuals. Firstly, my principle supervisor, Rosalind Allen, whose guidance and encouragement throughout the past three and a half years can not be overstated. Your office door was always open to discuss the implications of this or that result, even if it was five o'clock on a Friday. I would also like to thank my second supervisor, Davide Marenduzzo, whose advice, particularly on some of the active simulations, was invaluable. During my PhD I managed to go to several excellent schools and conferences which broadened my soft matter horizons. Through these events I met some great people and I am particularly thankful for the input and feedback I received on my work on these occasions.

Special thanks are due to all of the people in 2510 and later on in 2509 – you could not imagine a nicer bunch of people to work alongside. For useful discussions in the latter years, I particularly want to thank Rob Concannon, who was always available to chat through some maths, and Kym Eden, the resident computer and programming guru – why didn't we just do it all in Python from the start?

For their continual love and support my thanks go out to my parents, my brother, Michael, and my sister, Rebecca. You were always there for me and helped me to get to where I am today – thank you. Finally, I want to express my immense gratitude to my partner, Lea. Together we managed to get each other through the ups and downs of a PhD – this was no mean feat. Thank you for always being there, your support means everything to me.

Contents

List of Figures

List of Tables

Chapter 1

Introduction

Osmosis is the physical phenomenon in which a concentration difference of impermeant solute molecules across a semi-permeable membrane produces a difference in solvent density, and in pressure, across the membrane. It is the driving force behind many phenomena in nature, including water uptake by plants and the regulation of salt levels in the blood. Osmosis also lies at the heart of many important phenomena in chemical physics, including the Donnan effect [8] (in which charged particles distribute themselves unevenly across a semi-permeable membrane), the depletion interaction [136] (where an attractive force, proportional to the osmotic pressure, is generated between two colloidal particles immersed in a polymer solution) and, recently, mechanisms for generating self-propelled particles [25, 159]. Furthermore, industrial applications based on osmosis, such as osmotic power and desalination plants [1, 52, 109, 144], are also generating much current interest. Although the thermodynamics of osmosis is well understood, the physical principles which underlie the microscopic dynamics of the solvent particles remain the subject of debate [42, 170]. This leads to difficulties in understanding certain important non-equilibrium phenomena for which osmosis plays a significant role [25, 48, 135, 141, 159]. Because these phenomena are non-equilibrium, a thermodynamic description is not valid. Thus, a clear picture of the underlying molecular dynamical mechanisms is an essential prerequisite for understanding osmotic phenomena in these systems. Yet such a picture is largely lacking, even though the dynamical basis of osmosis has been the subject of over 100 years of discussion, by scientists from a variety of different disciplines. In this thesis molecular dynamics (MD) simulations are used to better understand the phenomenon of osmosis both at equilibrium, and in a non-equilibrium version of the osmosis experiment, where the solute particles are made active by the input of energy

into the system.

1.1 Early experiments and the law of van 't Hoff

The scientific study of osmosis goes back more than 100 hundred years to the mid 18^{th} century. By covering a vessel containing alcohol with a piece of pig's bladder and immersing this within a bath containing water, Abbé Nollet observed the net transfer of water across the bladder into the alcoholic solution, a process which would, occasionally, result in the bursting of the bladder [108]. The original volumes describing his work, however, were, until recently[1], notoriously difficult to acquire [91]. Therefore, it was approximately eighty years before Henri Dutrochet became aware of the phenomenon [33, 34]. It was Dutrochet who named the process osmosis[2] and designed the first osmometer, shown in Figure 1.1(a), which he used to record the rise in the level inside a capillary tube having placed lavender oil and olive oil on either side of a semi-permeable membrane (comprising a pig's bladder); an effect he was not able to reconcile with the capillary action.

With the development of artificial membranes by Graham, Traube and Pfeffer [51, 116, 157] in the mid to late 19^{th} century, more accurate experiments into the phenomenon could be conducted. By precipitating copper ferrocyanide onto the porous walls of an earthenware pot, Pfeffer [116] was able to construct a robust semi-permeable membrane that allowed the passage of water, but inhibited the flow of sucrose molecules across it; see Figure 1.1(b). In his studies Pfeffer noted, as Nollet and Dutrochet had before him, that upon placing differing concentrations of sucrose solutions on either side of the membrane, water would flow from the less to the more concentrated solution, producing a difference in the pressures of the two solutions: the osmotic pressure.

The results of Pfeffer were brought to the attention of van 't Hoff, a Dutch chemist who, in 1887, used the kinetic theory of gases to formulate a theory for the osmotic pressure of a solution [62]. He supposed that the solute particles behaved as if they were a gas, unaffected by the surrounding solvent. Thus, van 't Hoff proposed that the pressure difference should, at low solute concentration, simply obey the ideal gas law of Clapeyron,

[1] A digital copy has recently been made available (24/08/2009) courtesy of the French National Library. However, only the original document, in French, is available.

[2] He actually named it endosmosis, where osmo is Greek for push or thrust and endo is Greek for inwards.

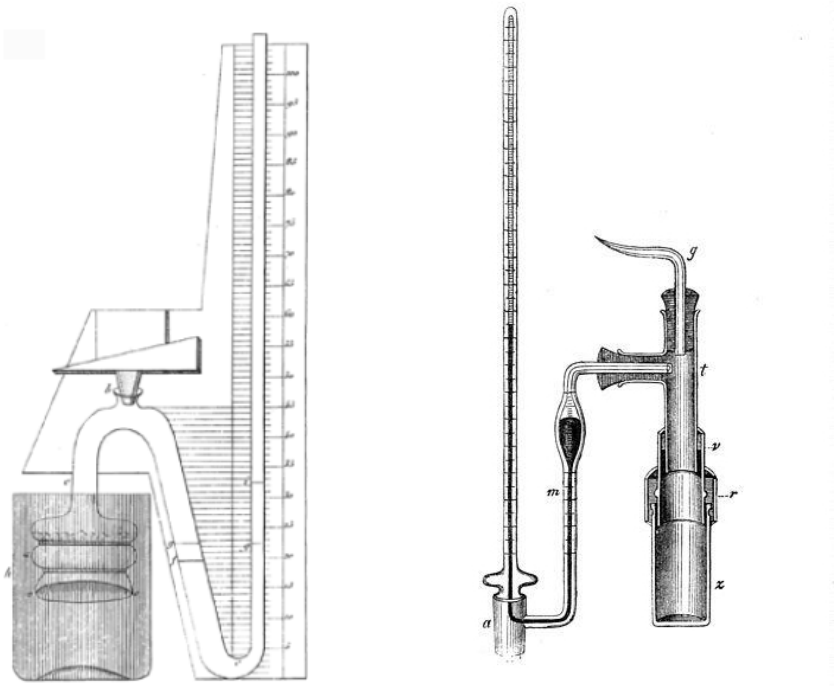

(a) Dutrochet osmometer. **(b)** The Pfeffer cell.

Figure 1.1 Panel (a) shows an example of an early osmometer developed by Dutrochet. The diagram is taken from [163], but was originally published in [35]. In panel (b) a sketch is shown of a Pfeffer cell [116], the first device capable of making accurate measurements of the osmotic pressure of a solution. In (a) and (b) a U-shaped manometer tube is connected to the osmosis experiments to measure the osmotic pressure. In the first case, (a), a pig's bladder is used for the membrane, whereas in (b) the Pfeffer cell utilises a more robust artificial membrane (see main text for further details).

$$\Delta P = k_B T \Delta c_s. \tag{1.1}$$

In the above equation, ΔP is the resulting pressure difference, Δc_s the concentration difference of impermeant solute particles across the membrane, k_B Boltzmann's constant, and T the temperature at which the experiment is conducted. This same result was later (in 1897) re-derived by Gibbs who demonstrated that the van 't Hoff relation can be reached by setting the chemical potential of the solvent equal across the membrane [46]; the thermodynamic origin of the osmotic pressure is then the entropy of mixing between the solute and solvent particles. A version of this derivation (presented by Finkelstein [42]) proceeds as follows. The steady state is first established as the equivalence of solvent chemical potentials in the two compartments,

$$\tilde{\mu}_w^{(1)} + RT \log X_w^{(1)} + P^{(1)} \bar{V}_w = \tilde{\mu}_w^{(2)} + RT \log X_w^{(2)} + P^{(2)} \bar{V}_w, \tag{1.2}$$

where $\tilde{\mu}_w$ is the standard chemical potential of the solvent, R, T and P are the gas constant, the temperature and the pressure, respectively, X_w is the mole fraction of the solvent and $\bar{V}_w$ its partial molar volume. The above definition of the steady state corresponds to chemical equilibrium and is consistent with there being zero net flux of particles across the membrane; it is the definition of the steady state which we will use throughout this thesis. It is then assumed that compartment 2 contains only solvent and compartment 1 contains solvent + solute, with an equal total molar concentration. Because the standard chemical potential is a constant, and since there is only pure solvent in compartment 2 (so that $X_w^{(2)} = 1$), Eq.(1.2) can be re-written as follows:

$$\Delta P \equiv P^{(1)} - P^{(2)} = -\frac{RT}{\bar{V}_w} \log X_w^{(1)}. \tag{1.3}$$

Assuming also that the solution is dilute, *i.e.* that $X_s << 1$ — where X_s is the mole fraction of the solute in the solution — allows us to re-write Eq.(1.3) as:

$$\Delta P \approx \frac{RT}{\bar{V}_w} X_s. \tag{1.4}$$

Finally, by writing the mole fraction as $X_s \equiv \frac{n_s}{n_s+n_w}$, where n_i denotes the number of moles of species i, and also using $n_s << n_w$, we arrive at the van 't Hoff relation:

$$\Delta P \approx RT \frac{n_s}{\bar{V}_w n_w} = RT \frac{n_s}{V_w} = RT c_s. \tag{1.5}$$

Although this derivation does not assume the solute to behave as an ideal gas (as van 't Hoff did), it does rely on two other assumptions to reproduce the law of van 't Hoff. First, the activity of the solvent,

$$a_w = \gamma_w X_w, \tag{1.6}$$

was assumed to be equal to its mole fraction, X_w – *i.e.* the activity coefficient, $\gamma_w = 1$. This implies that the solvent behaves in an ideal manner, *i.e.* that the details of the solvent-solute and solvent-solvent interactions are not important. Secondly, we assumed that the solution is dilute, *i.e.* $X_w \to 1$. Often in experimental work involving non-ideal, real solutions, the van 't Hoff law is abandoned in favour of an alternative relation based on experimental measurements [102]:

$$\Delta P = iMRT. \tag{1.7}$$

In Eq.(1.7), the molarity, M, is used as a measure of the concentration (Avagadro's constant, N_A, relates the number and molar concentrations, $M = c_s/N_A$) and i is a dimensionless "van 't Hoff factor", that describes deviations from the condition of ideality discussed above. Equation (1.7) predicts, as Eq.(1.1) does, that the osmotic pressure will, at low solute concentrations, vary linearly as a function of increasing solute concentration, a prediction that has been reproduced in both experiment and simulation [102, 103, 156].

The derivations discussed so far, however, do not specify the microscopic, mechanical forces that transport the solvent particles across the membrane, from the less to the more concentrated solution, both prior to and during the osmotic steady state. For a complete understanding of the solvent dynamics at the membrane, that adequately captures the observations made by Nollet, Dutrochet and countless others since, a model must first be developed that attempts to explain the particle dynamics on simple, yet mechanical, grounds, without recourse to thermodynamical concepts.

In an important step towards understanding osmosis at the molecular level, McMillan and Meyer [96], in 1945, incorporated osmosis into the framework of statistical mechanics. This work showed that, in the presence of a solvent species (able to cross the membrane in either direction), the osmotic pressure of a solution could be expressed in terms of a potential of mean force between the solute particles. In other words, the solvent particles mediate the interactions between the solute particles. McMillan and Meyer provided an expression for the osmotic pressure in terms of a virial series:

$$\frac{\Delta P}{\rho k_B T} = 1 + B_2^* \rho + B_3^* \rho^2 + ... \ . \tag{1.8}$$

In Eq.(1.8), ρ denotes the concentration of the solute species and the B_i^* terms represent virial corrections to the osmotic pressure from the ideal van 't Hoff expression, due to interactions between solute particles, which are mediated by the solvent. For example the B_2^* term may be expressed as:

$$B_2^* = -\frac{2\pi}{3k_B T} \int_0^\infty r^3 g(r) \frac{dV}{dr} dr, \tag{1.9}$$

where $g(r)$ is the pairwise radial distribution function (see Section 2.2.2) between two solute particles radially separated by a distance r, and V is the solvent-mediated effective interaction (also referred to as the potential of the mean force) between two solute particles in the solution, assumed to be pairwise additive. Although Eq.(1.8) is expressed in terms of molecular level properties, such as the inter-particle potential — giving a deeper insight into the thermodynamic origins of osmosis — it does not make any predictions about the dynamics of the solvent particles.

To summarise, the relations outlined above allow us to compute the osmotic pressure of a given solution, both in terms of macroscopic variables, such as the temperature and molarity of a solution, but also in terms of variables on the atomic scale, such as the inter-particle potential. However, these relations do not provide any information on the microscopic dynamics of the solvent particles at the membrane, both prior to and during the steady state.

1.2 An ongoing confusion about the solvent flow

The dynamical mechanisms underlying the solvent flow across the membrane during osmosis have been debated since before van 't Hoff and Pfeffer. The debate has focused in particular on whether the transfer of solvent across the membrane proceeds via a diffusive or a mass flow and whether a detailed knowledge of the solvent-solvent and/or solute-solvent interactions at the membrane are necessary to explain the phenomenon of osmosis.

1.2.1 Diffusive versus mass solvent flow

The earliest discussions surrounding this issue date back to the mid 19^{th} century, when Brücke suggested [14] that the phenomenon of osmosis might be explained by repulsive and attractive physiochemical forces between the particles and the membrane. In his seminal work of 1855 [41] Fick contested this point. He used his newly derived law for liquid diffusion,

$$\vec{J} = -D\vec{\nabla}C, \tag{1.10}$$

where $\vec{J}$ is the flux (the amount of substance which crosses a unit area during a given

time interval), C is the concentration of particles at a particular spatial location and D is their diffusion coefficient, to argue for the "diffusion of salt solutions through porous partitions". He concluded that the theory of diffusion he had laid out would very likely, with or without modification, "serve as the foundation of a subsequent theory of these very dark phenomena". Given the impact that his theory has had in describing a multitude of biological phenomena, it is not surprising that osmosis is, to this day, regularly cited as a paradigmatic example of a diffusive process [97, 149].

However, various researchers have disputed whether osmosis really is a diffusive phenomenon [32, 60, 77, 92, 93, 123, 162]. Mauro [92, 93] produced data, see Figure 1.2(a), demonstrating that, for a concentration gradient of an uncharged macromolecule across an inert barrier, the flow of water proceeds faster than can be reconciled by purely diffusive processes. In one instance the diffusive component of the recorded flux constituted just $1/730^{th}$ of the overall flux (see table in Figure 1.2(a)). Instead he suggested that the transfer of water proceeds in an analogous manner to a mass flow of particles under the influence of a pressure gradient. This idea was actually suggested much earlier by Vegard [162], who described a similar phenomenon to Mauro and who also produced data, see Figure 1.2(b), suggesting that the flow of solvent can undergo a transition in more concentrated solutions, from an initially rapid solvent transfer across the membrane to a later slower rate of flow.

The equivalence between flows driven by a solute concentration gradient and those driven by a hydrostatic pressure gradient, as suggested by Mauro and others, may be mathematically expressed using the Kedem-Katchalsky relation [72, 73],

$$J_v = L_p(\Delta P - \Delta\Pi), \tag{1.11}$$

where the solvent flow, J_v, is expressed in terms of a membrane filtration coefficient, L_p, and the difference in the hydrostatic, ΔP, and osmotic, $\Delta\Pi$, pressures across the membrane. We shall see later on (Figure 3.2(b) in Section 3.1) that this expression should be modified in the case that the membrane is partially permeable to the solute particles.

The assertion that diffusive mechanisms could not account for the observed solvent flux in osmosis proved controversial [20, 30]. In particular, the debate focused on whether the simple experiments of Mauro could accurately determine the diffusive permeability of the solvent. It was suggested that, in an osmosis experiment, "unstirred layers" might exist close to the membrane which would affect the rate of solvent diffusion. Finkelstein

Flux in moles/sec. per dyne/cm.²

Membrane	Diffusion flux[4]	Total observed flux	Ratio diffusion /total
Group I	1.2×10^{-13}	8.8×10^{-11}	1/730
Group II	5.6×10^{-14}	3.1×10^{-12}	1/55
Group III	1.1×10^{-14}	3.9×10^{-13}	1/36

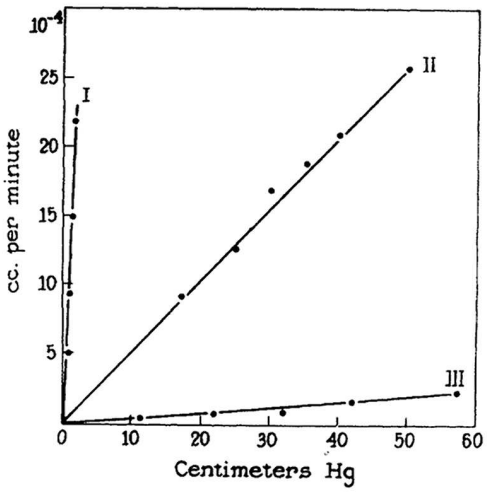

(a)

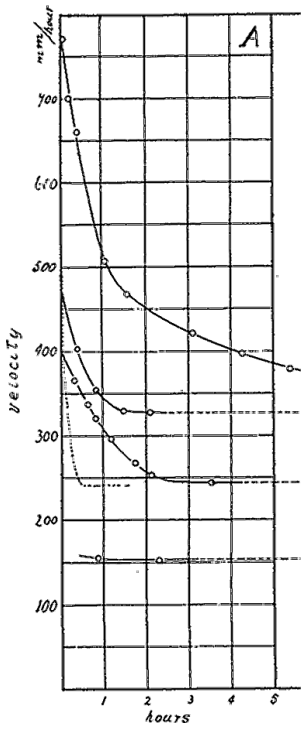

(b)

Figure 1.2 The tracer flux of particles across an inert barrier (a collodion membrane) is shown in panel (a). The table in (a) shows the results of the tracer flux for three different pore sizes. These results are plotted underneath the table as a function of the pressure difference across the membrane. In panel (b) the velocity of the water transfer across a copper ferrocyanide membrane versus time is shown for several solute concentrations. The upper data marks the most concentrated solutions and the lower data the most dilute solutions. The figures in (a) are taken from [93] and the graph in (b) from [162].

[42] describes how the solvent flux may be affected as follows. Given a membrane separating two stirred solutions, there is a region on either side of the membrane, of size δ_1 and δ_2, respectively, that remains unmixed. The observed diffusive permeability, $(P_{d_W})_{obs}$, may then be written as $\frac{1}{(P_{d_W})_{obs}} = \frac{1}{P_{d_W}} + \frac{\delta_1}{D_w} + \frac{\delta_2}{D_w}$, where P_{d_W} is the true diffusive permeability coefficient and D_w is the diffusion coefficient of the solvent. This relation may be re-arranged to read as follows:

$$(P_{d_W})_{obs} = \frac{1}{1 + P_{d_W}(\delta/D_w)} P_{d_W}, \tag{1.12}$$

where $\delta = \delta_1 + \delta_2$. Thus, as the thickness δ of the unstirred layers increases, $(P_{d_W})_{obs}$ decreases. In contrast, unstirred layers have only a much smaller effect on the observed osmotic permeability coefficient P_f, defined as $(P_f)_{obs} = P_f \mathrm{e}^{-v\delta_1/D_s}$, where D_s is the diffusion coefficient of the solute and v is the velocity of the flow. Consequently,

the presence of unstirred layers in an osmosis experiment may result in the ratio P_f/P_{d_W} being overestimated, leading to the incorrect conclusion that diffusion alone cannot account for the osmotic flow. The importance of this effect was emphasised by Dainty [28] and later by Finkelstein [42]. Dainty claimed that "no valid comparison of $L_pRT/\bar{V}_w$[3] with P_d has been made with any plant cells or tissue and it will prove a very difficult matter". Thus, despite the importance of understanding whether osmotic flow is diffusive or bulk-like, at the end of the 1970s the experimental situation remained unclear [56, 57, 61, 94, 147, 170].

The state of the debate was summarised by Finkelstein in 1987 [42] who emphasised the need for a kinetic theory of liquids to properly describe osmotic phenomena at the membrane. Finkelstein stressed the dependence of the membrane geometry on the resulting solvent flow, noting that a porous membrane develops a mass flow across it (assuming unstirred layers do not significantly contribute to the flow) that obeys Poiseuille's law, whereas in an oil membrane, for example, the flow is diffusive. He also pointed out that the solvent flow in very thin pores, as is often the case for biological membranes, is observed to occur [82] at a rate faster than can be reconciled using a purely diffusive explanation. However, at the same time, such flows can not be described using a continuum explanation in terms of Poiseuille's law, which requires layers of fluid to form within the pore. We shall see, however, in Section 3.1 that the solvent flow through molecularly narrow pores is a special case [70].

Thus, at the macroscopic level, our understanding of osmotic flow remains in a state of some confusion. We therefore turn our attention to the microscopic processes that take place at the membrane to develop a better understanding of the solvent dynamics.

1.2.2 Microscopic models for osmosis

A number of different models have been proposed to explain the detailed dynamics of the solvent flux during osmosis. These can be grouped into four different categories [173]: concentration-diffusion models, interaction energy models, solute bombardment models and finally solvent entrainment models.

In the solute bombardment model, originally proposed by van 't Hoff, the solute particles are treated as though they are an ideal gas and the solvent particles are essentially assumed to be invisible. The difference in the number of solute collisions on either side of the membrane is then said to constitute the osmotic pressure. Two

[3] Where $L_pRT/\bar{V}_w$ denotes the total solvent flux.

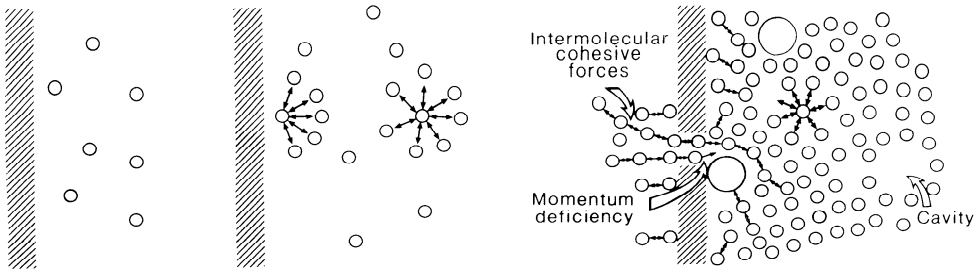

Figure 1.3 Diagram illustrating the "momentum deficiency" model of Kiil. The solutes' inability to access those regions around the pore mouth lead to a deficiency in bombardments here. Consequently the solvent in the rightmost diagram flows through the pore from left to right prior to the steady state. The image is taken from [75].

obvious arguments against this model are as follows [173]. First, liquids have internal cohesive forces, thus the pressure exerted against the membrane by the liquid will be far lower than that exerted by a gas. Secondly, in this model the solvent particles are assumed to be invisible, and therefore any difference in solvent force on the membrane is not considered, even though there will almost certainly be such a difference. For porous membranes, Kiil [74, 75] suggested, in a variant on the solute bombardment theory, that the solutes' inability to access the region around the pore mouth leads to a momentum deficiency which facilitates the flow of solvent from the less to the more concentrated solution prior to the steady state. A diagram to illustrate this model, taken from [75], is shown in Figure 1.3. This model does not, however, account for osmotic flow through non-porous membranes.

The second category of mechanistic models are concentration-diffusion models. These seek to explain osmosis on the grounds that, even though the solvent particles pass through the membrane in both directions, the concentration of solvent molecules is initially lower on the solution side and therefore solvent will tend to diffuse into the solution to balance the difference in solvent concentrations across the membrane. In this type of model the particle sizes will therefore play an important role in the resulting osmotic pressure. At higher solute concentrations, nanoscale simulations [105] (see Section 3.1.1) have demonstrated that such factors can play an important role in the resulting osmotic pressure. However, in the low solute concentration limit, the simulation results were found to be in agreement with experimental results [173], that is the osmotic pressure is independent of the solute and solvent properties. Thus, a model that seeks to explain osmosis on the basis of a gradient in the solvent density across the membrane should reproduce the van 't Hoff relation (Eq.(1.1)) for dilute solutions; a result which does not depend on the particle sizes. It is not clear that this

is the case for concentration-diffusion models.

In the third type of model, the movement of solvent particles through the membrane is explained as a process induced by a specific kind of solute-solvent, solvent-solvent or solvent-membrane interaction. Brücke proposed [14] that osmosis might be explained by an enhanced solvent-membrane interaction, resulting in the solvent being drawn across the membrane prior to the steady state. Hammel and Scholander [56] consider a model where the solvent in the solution comes under tension (a negative pressure) as the solutes diffuse away from the "free surface" of the solution. The resulting negative pressure draws solvent across the membrane, from the less to the more concentrated solution. However, the fact that the van 't Hoff law holds irrespective of the details of the inter-particle or particle-membrane interactions, and that osmosis has been noted to occur in systems comprising hard spheres [76], or those without solvent-membrane interactions [67], can be used as arguments against such models.

A fourth category of generic model considers "solvent entrainment" at the pore [40]. More specifically, interactions between the solvent and solute particles provide a "sucking force" that pulls the solvent particles across the membrane into the solution. In a slight variant on this type of model, Ben-Sasson and Grover [137] have suggested that the solutes act as micropumps and by reflecting off a pore mouth, the solutes suck the solvents across the membrane. Yoffe [173] expanded slightly on this, stating that as the solutes move away from the pore mouth, they leave a vacuum into which solvent particles can move. In Chapter 5 we shall test whether such processes occur in a simple, "minimal model" of osmosis.

In addition to the four categories of models proposed by Yoffe, I add here models based on the hopping of solvent particles at the entrances to porous membranes. One such model to explain osmosis (elaborating on the work of Ray [132]), based on the initial concentration gradient of solvent particles slightly inside the pore mouth and that just inside the solution, was proposed by Dainty [28, 29]. In Dainty's model, those solvent particles in the more concentrated solution are initially less likely to hop into the pore entrance than those in the less concentrated solution, as the solute particles block their passage into this region. Thus a deficit of particles at one end of the pore is established and consequently a pressure gradient develops inside the pore, which drives the solvent flow at a rate *faster* than diffusion. This explanation was proposed to describe the aforementioned results reported by Vegard and Mauro (see Section 1.2.1). However, the absence of a suitable kinetic theory of liquids meant the resulting osmotic pressure could only be derived to within a factor of two of experimental observation.

Furthermore, it fails to explain the flow of solvent in systems composed of non-porous membranes. As the first to derive the osmotic pressure using arguments removed from thermodynamics, however, Dainty was one of the first researchers to offer a possible insight into the mechanical processes operating at the opening to the pore. This enabled a significant step forward in our understanding of osmotic phenomena that was supported by later researchers in the field [146, 147]. More recently, Chou considered [21] the possibility that solute particles can partially permeate into the pores when deriving relations for the flux of particles in a single-file channel. It was found that, under these circumstances, the solvent flux through the pore can be significantly reduced and in extreme cases may even become negative. The decreased solvent flux through a partially solute permeable pore has since been observed in simulations [76] and will be discussed further in Section 3.1.

In this section we have seen that an abundance of different models exist, each of which seeks to explain osmosis and osmotic phenomena. For a true understanding of the solvent dynamics at the membrane, we should start at the molecular level. Yet there currently exists no clear consensus in the literature as to the mechanism that dictates the solvent flow, be it concentration based, entrainment based, or something else entirely. To resolve some of these issues, one of the goals of this thesis will be to clarify the fundamental mechanism responsible for driving the flow of solvent across the membrane both during and prior to the steady state in osmosis.

1.3 Mechanical derivations of the osmotic pressure

In Section 1.1 the van 't Hoff law was derived from thermodynamic and statistical mechanical considerations. Here I review some more recent attempts to derive this relation from purely mechanical principles. Aside from Dainty, who outlined a hopping model for porous membranes, it was not until the 1990s that a mechanical approach was considered by both Brady [11], using Brownian dynamical considerations and an implicit solvent, and Guell and Brenner [53, 54], who included the solvent explicitly when deriving the osmotic pressure starting from Newton's second law.

Brady's derivation begins with the N-body Langevin equation for a system of colloidal particles,

$$M \cdot \frac{d\vec{v}}{dt} = \vec{F}_H + \vec{F}_B + \vec{F}_P, \tag{1.13}$$

where M is a generalised mass/moment of inertia matrix and $\vec{v}$ is the particle's translational/rotational velocity vector. In this description the solvent is not modeled explicitly, but via effective Brownian and hydrodynamic forces on the colloids, represented by $\vec{F}_B$ and $\vec{F}_H$, respectively; the solvent therefore represents a continuum fluid imparting stochastic kicks to the colloidal particles here. The final term, $\vec{F}_P$, represents the colloid-colloid interactions, which are mediated by the solvent particles in the fluid. Brady subsequently demonstrated that, from Eq.(1.13), the osmotic pressure of attractive and repulsive colloidal suspensions could be derived for fluids at low Reynolds number. The resulting expression,

$$\frac{\Pi}{nk_BT} = 1 + 4\phi g(2) - \int \langle \vec{x}_2 \cdot \vec{\nabla}_2(\, V_p/kT)\rangle_2 P_2(\vec{r}_2|\vec{r}_1)\, d\vec{r}_2, \tag{1.14}$$

is analogous to the one derived previously by McMillan and Meyer [96] (Eq.(1.8)) from thermodynamical and statistical mechanical considerations. In Eq.(1.14), ϕ is the packing fraction, n is the number density and $g(2)$ is the pair distribution function for the colloids. The integral term, in which V_p is the inter-particle potential and P_2 is the two particle probability distribution function (*i.e.* the probability to find the given co-ordinates for particles 1 and 2 in the system's phase space), describes the virial corrections to the pressure expressed, as in Eq.(1.9), solely in terms of a solvent-mediated colloid-colloid interaction. Brady thus demonstrated for the first time that mechanical concepts, such as stochastic forces and Brownian motion, could be used in deriving the osmotic pressure of a colloidal suspension, without reference to the solvent chemical potential and other thermodynamic concepts.

An alternative derivation for the osmotic pressure starting from Newton's second law and explicitly including the solvent was outlined by Guell and Brenner [53, 54]. They considered a system in which a porous membrane separates two solvent-containing reservoirs bounded by pistons that are held fixed. At time $t = 0$, a single Brownian tracer particle, that is prohibited from accessing the membrane region of the system, is introduced into one of the reservoirs to represent a solute particle. The authors were then able to write down three equations describing Newton's second law for the solvent particles, the solute particle and the pistons. The solute-membrane force in this setup is

$$\vec{F}_{MP} = -k_BT\vec{\nabla}' E(\vec{x}', \vec{\omega}'). \tag{1.15}$$

In Eq.(1.15), E describes a dimensionless potential characterising the solute-membrane interaction in terms of the physical position of the solute particle, $\vec{x}'$, and its internal configuration $\vec{\omega}'$; k_B and T are, as usual, Boltzmann's constant and temperature of the system. Following several manipulations to the equations of motion of the system, which include: application of Newton's third law; taking ensemble and time averages; and relating the force to the pressure as $P = F/A$, the authors arrive at the following relation for the observed pressure difference between the two reservoirs:

$$\Delta P = k_B T \Delta p^0(\vec{x}'), \tag{1.16}$$

where p^0 is the probability density for finding the solute particle at position $\vec{x}'$. A dilute solution is then defined as one which obeys $p^0 = N_A c_s$, where N_A and c_s are the aforementioned Avogadro's number and equilibrium solute concentration. Upon application of this relation, the law of van 't Hoff is recovered.

Whilst the derivation is thorough, it is only valid in dilute systems of inert, non-interacting solute particles. Furthermore, the derivation is rather complicated, making it difficult to extract an intuitive understanding of the phenomenon.

Finally, Atzberger and Kramer [7] have considered several derivations for the osmotic pressure. Considering the concentration of solute particles to be represented by a series of delta functions, a similar derivation for the osmotic pressure to Guell and Brenner is given. In this work, however, the solvent is coarse-grained out and the osmotic pressure is simply established as the solute-wall force. The osmotic pressure is also derived using Stokes' equation in what the authors term a continuum fluid mechanical picture. However, the osmotic pressure once again arises here from consideration of the forces acting on the solute particles and the mechanism of solvent transport across the membrane is not discussed. The authors do find that in finite-size systems, such as virus capsids, the osmotic pressure measured using the solute-wall force is different from the result obtained when considering the local fluid pressure. This is because the length scales of interactions in these systems become larger than the system size itself. Furthermore, as is shown in Figure 1.4, as the size of the system decreases, the resulting osmotic pressure can be markedly different from the value predicted using the van 't Hoff relation (Eq.(1.5)). In this thesis we only consider systems in which the osmotic pressure measured using the local fluid pressure is in agreement with the solute-wall force; see Section 3.2.3.

Thus, the van 't Hoff relation can be derived from mechanical principles, both when

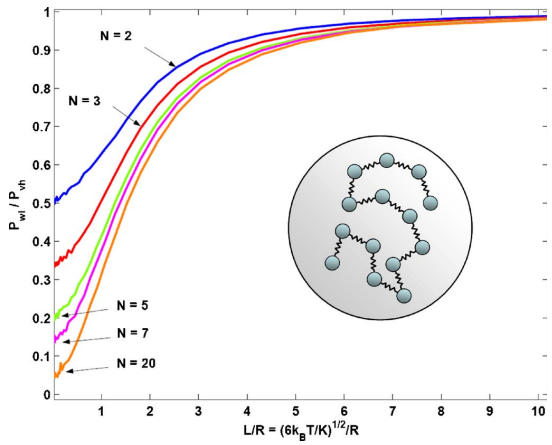

Figure 1.4 The osmotic pressure for a linear polymer confined in a spherical chamber is first computed from the solute-wall pressure. The osmotic pressure as given by van 't Hoff is then computed and the ratio of the two results is plotted as a function of L/R, where $L = (6k_BT/K)^{0.5}$ denotes the length at which the bond energy becomes $3k_BT$, and R is the radius of the chamber. The figure has been taken from [7].

explicitly considering the solvents' motion or from a hydrodynamic, coarse grained perspective. In Chapter 5 an alternative derivation for the osmotic pressure is presented, based on the hopping of solvent particles at the membrane (similar in spirit to the models discussed in Section 1.2.2). Later on in Chapter 7 we observe that the dynamics of the solvent in a non-equilibrium osmotic setup can be heavily influenced by the introduction of active solute particles to the system and that the osmotic pressure is significantly increased using active solute particles.

1.4 Osmotic power and the desalination of water

The mixing of solvent and solute particles at a semi-permeable membrane is associated with an increase in the entropy of the system; the so-called entropy of mixing. It has been known for some time that useful work might be extracted from osmotic systems and, furthermore, that semi-permeable membranes can be used as a means of sifting wanted from unwanted products in a solution. Recently, as a result of rapid improvements in membrane technology, osmosis has begun to be used for these purposes in industry, both in the purification of water and as a sustainable technology for the generation of electricity. Later on in Chapter 7 I consider whether a particular modification to the classic osmosis experiment might be applicable in industry. I therefore present a short section here on current uses of osmosis in industry.

1.4.1 Osmotic power generation

Two different techniques currently exist which harness the energy produced in the mixing of fresh water and salt water. The first method, Pressure Retarded Osmosis (PRO), was patented by Sidney Loeb in 1975 [85]. The process is outlined in [109] and is described in detail in [1, 2, 144]; here I present a brief overview. Salt water and fresh water must first be extensively filtered and brought together at a membrane which permits the flow of the water, but which inhibits the flow of salt. Due to osmosis, some fresh water flows into the salt water compartment, diluting it. This causes an increase in the volume of water on the salt water side of the membrane which is siphoned off and used to turn a turbine that drives a generator. The remaining water is then pumped back into the river/sea; see Figure 1.5(a) for a diagram illustrating this process. By continuously repeating this procedure a steady supply of power can be extracted.

The power density, W, that can be extracted from this process is related to the flux of solvent (J_v) and the pressure gradient (ΔP) across the membrane [2], $W = J_v \Delta P$, which, using Eq.(1.11), can be expressed as $W = A(\Delta\Pi - \Delta P)\Delta P$. By differentiating with respect to ΔP the theoretical maximum value for W can be calculated: $W = A\frac{(\Delta\Pi)^2}{4}$. A recent study concluded that a "thermodynamic extraction efficiency" of 91.1% could, in theory, be achieved for this technology [172]. In practice, the membranes require frequent flushing to remove unwanted minerals and muds from the pores and, furthermore, the effect of unstirred layers around the membrane (see Section 1.2.1) can result in lower osmotic pressures being achieved than anticipated. Preliminary results reported by Staatkraft, the first company attempting to commercially develop this technology, have demonstrated a power output of 0.5 W/m^2 using a 28 m^2 membrane. In a review article, Achilli *et al.* [2] reason that, based on current technologies, membranes need to generate 5 W/m^2 in order that the revenues generated balance the cost of implementation.

Although the concept of generating power by PRO is not new, the membrane technology is not yet at the stage where this method forms a commercially viable renewable method for power generation. In this regard, Staatkraft estimates that 30 osmotic power plants will be built by 2030 [12]. Furthermore, issues concerning the disposal of the chemicals used for cleaning the membranes and the effects of pumping brackish water back into the local ecosystem have been raised [101].

The alternative method, Reverse Electrodialysis (RED), was first proposed in 1954 [113]; however it has only recently been considered as a viable technique for power

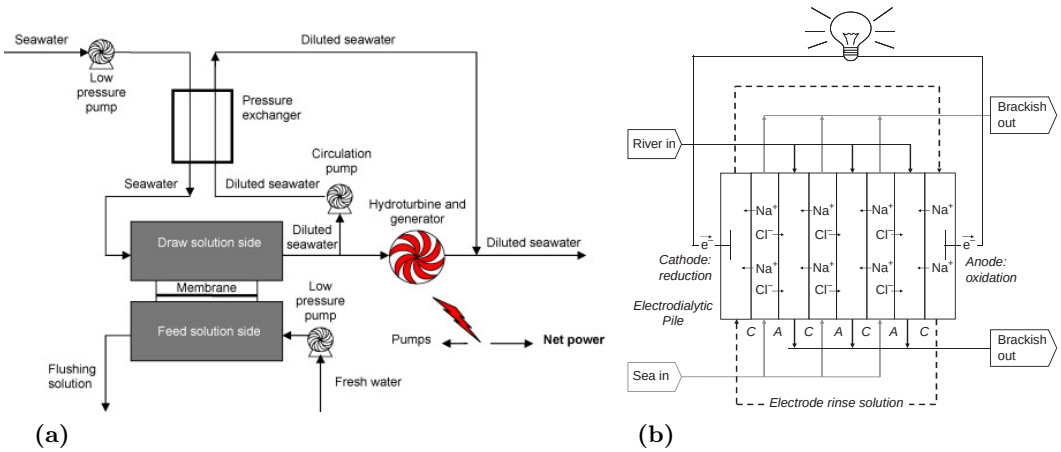

Figure 1.5 Diagrams taken from [1] and [118] illustrating the processes which are necessary in achieving power generation by PRO (panel (a)) and RED (panel (b)) respectively.

generation. The method works as follows. Fresh water from a river and salt water from the sea are pumped into separate compartments within a larger unit containing alternating stacks of cation and anion exchange membranes; see Figure 1.5(b). The ions in the salt water compartments dissociate and travel across the membranes in opposing directions. As a result, cations accumulate in the cathode compartment and anions collect in the anode compartment. A flow of electrons is then established through reduction at the cathode surface and oxidation at the anode surface. This current can be maintained and used to generate electricity by the constant flushing of the resulting brackish water out of the system.

It has been argued that a better performance is achieved when mixing sea water and river water using this technique as opposed to PRO [119]. However, RED has similar limitations to PRO in terms of the efficiency and cost of membrane production, and similar concerns have been raised in relation to the effects on the local ecology [118]. Currently a demonstration project is being conducted in the Netherlands [161] and there are further ambitions to scale-up the use of this technology.

A further technique, based on the flushing of salt and fresh water through a cell containing carbon electrodes, has been proposed by Brogioli [10, 13]. In the future this technique may provide an alternative means of power generation.

1.4.2 The purification of water by reverse osmosis

Another important industrial application of osmotic principles is in the desalination of water by reverse osmosis. The process is used not only in the production of drinking water, but also in industry and agriculture. In the standard osmotic setup, when fresh water and salt water meet at a semi-permeable membrane, some fresh water will flow into the salt water compartment. In the case of reverse osmosis we wish to achieve the opposite, that is we attempt to displace the water from the salt water compartment into the fresh water side, increasing the amount of fresh water available. This can be achieved by "pushing" the water out of the salt water side by applying a pressure (using a piston) which exceeds the osmotic pressure difference across the membrane. Various methods have been developed to best utilise this technique. In a recent industrial trial [126] — so-called NEWater — reverse osmosis plays an important role in the water purification process, removing heavy metals, nitrates, chlorides and sulfates. Reverse osmosis is also heavily employed for water purification in the United States with 69% of plants using reverse osmosis [24]. As a further benefit, portable devices have been developed allowing individual users to generate their own fresh water.

In the development of technologies for clean energy production by osmosis and in the purification of water by reverse osmosis, investment in membrane development is critical. Recent research into nanotube membranes [70, 143, 152] demonstrates that next generation carbon and boron nitride nanotubes could help to resolve some of the issues currently facing these industries, as impressively large solvent fluxes have been reported [63, 70]. Further improvements in these processes may also be achieved (independently of advances in membrane technology) by considering alternative models for osmosis, such as those discussed later on in Chapter 7.

1.5 Thesis outline

In this chapter we have seen that osmosis is a phenomenon of critical importance both in nature and, increasingly, in industrial processes. Yet there remain many unanswered questions in the field. For example, can we derive a *simple* and intuitive description of the steady-state solvent dynamics at the membrane that does not rely on thermodynamic concepts? Also, under what circumstances does the solvent transfer prior to the steady state proceed via a diffusive flow and when via a bulk flow? Motivated by recent experimental developments (see Chapter 7), we can also explore the resulting osmotic pressure and solvent dynamics in an osmotic system in which

the solute particles drive the system out-of-equilibrium. In this thesis minimal models are used to study the fundamentals of osmosis in several scenarios to answer these important yet unresolved issues.

In Chapter 2 I present an overview of the method used to study osmosis throughout this thesis: molecular dynamics simulation. A brief introduction is first given to the MD technique before I discuss some of the analysis methods used, such as the calculation of the diffusion coefficient and the radial distribution function from simulation data. In Chapter 3 I review previous simulations of osmosis, discussing their findings and commenting on possible avenues for future work, following which the different simulation setups used to study osmosis in this thesis are outlined.

Before beginning to study osmosis, a new derivation for the local pressure in molecular dynamics is presented in Chapter 4. Here, I demonstrate that two separate, but equivalent, relations can be used to measure the local pressure and that they are both derivable from a fundamental relation, the "Schweitz virial relation". A closed virial relation is then used to derive a mechanical relation for the osmotic pressure in terms of the various solute-solute and solute-solvent interactions in Chapter 5, where a comprehensive study of the steady-state solvent dynamics and osmotic pressure is conducted for a minimal system with hard-sphere-like solute and solvent particles. In this chapter, a simple model, based on the hopping of the solvent at the membrane, is also presented. The model does not necessitate the entrainment of solvent across the membrane. Nevertheless the role of entrainment is explored by studying in detail the steady-state solvent membrane crossings.

To study the relaxation dynamics of the solvent particles prior to the steady state, a simple, finite barrier, representing the membrane, is introduced for the solvent particles in Chapter 6. Using a finite barrier serves to slow down the system's relaxation to the steady state, allowing us to study in detail the processes and timescales involved here. By studying both the net flow of particles across the barrier and the flux of tracer particles, we are able to derive a simple, diffusive model for the dynamics of the solvent particles which we test against the results from our simulations. An interesting transition in the solvent dynamics is observed to occur for both the net flux of particles and for the mixing of the tracers, for which a qualitative explanation is outlined.

In Chapter 7, the osmotic system is driven out-of-equilibrium by making the solute particles active. Results are presented for the osmotic pressure and the solvent flow in these active simulations, as well as a model which reconciles the solvent dynamics in the period prior to the steady state. The implications that using such a setup may

have for desalination technologies are also discussed.

Finally, I summarise the work presented in this thesis and discuss possible avenues for future work in Chapter 8.

Chapter 2

Molecular Dynamics Simulations and Data Analysis

In this chapter I first discuss the details of the method used to study osmosis in this thesis: molecular dynamics simulation. This was a major task for this PhD because all of the simulation code was written entirely from scratch in the C++ programming language. In the second half of the chapter an overview is given of some general techniques which have been used for data analysis. More general treatments of MD simulations can be found in the excellent books of Allen and Tildesley [4] and Frenkel and Smit [44]; here I focus on those aspects most relevant to this thesis.

2.1 Molecular dynamics

2.1.1 An overview

The molecular dynamics simulation method is based on Newton's second law, $\vec{F} = m\vec{a}$. Where $\vec{F}$ and $\vec{a}$ are the forces and acceleration of a particle at any given time and m is the particle's mass. If the forces are conservative[1] then they may be written as the derivative of a scalar potential U as follows: $\vec{F} = -\vec{\nabla}U$, where $\vec{\nabla}$ is the gradient operator. In simulations of realistic systems, such as proteins and metals, a great deal of effort has gone into the design of intermolecular potentials [4, 98]. However, in this work we are interested in simulating only very idealised model systems and so a simple

[1] This is generally the case in this thesis, although in Chapter 7, when an additional force is applied along the axis of the active swimmers, this condition is no longer true.

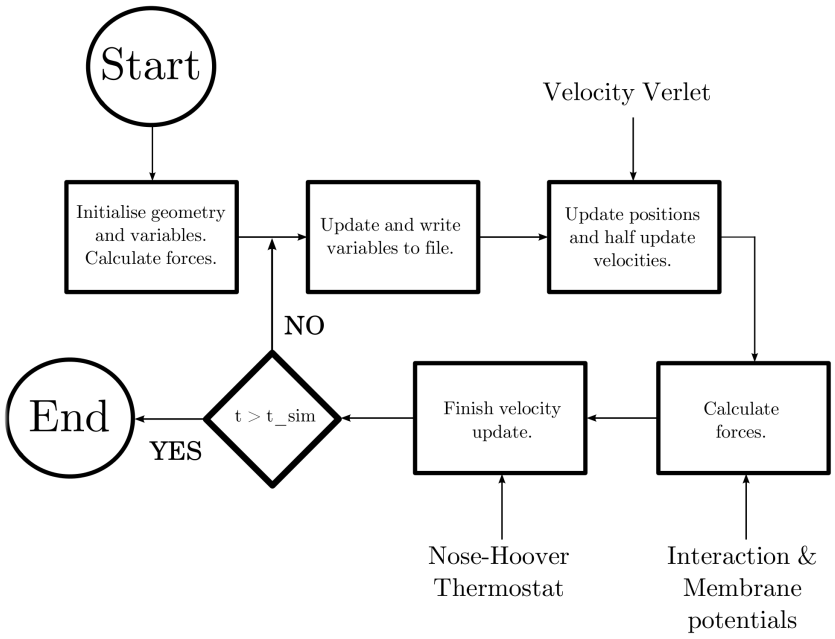

Figure 2.1 Flow diagram illustrating the key processes undertaken during the execution of the main simulation, for which the velocity Verlet algorithm is used.

interaction is used. For further details of the interaction potential see Section 3.2.1 and the simulation details for each of the separate results chapters.

In an MD simulation, Newton's second law is integrated numerically in time for the positions and velocities of all of the particles in the system. In Figure 2.1, a flow diagram illustrates the main tasks undertaken during the execution of my MD code. Although this type of procedure is common to most MD simulations, particular choices must be made with regard to, for example, the integrator used to evolve the positions and velocities and the thermostat used to maintain a fixed temperature. These choices are discussed in the subsequent sections.

2.1.2 Integrators

Many different integrators can be used to propagate the positions and velocities of the particles forwards through time. Here I discuss the integrator employed for this study: the velocity Verlet algorithm, which has been used because it is compatible with the Nosé-Hoover thermostat described later on in this chapter (Section 2.1.3).

The velocity Verlet algorithm essentially consists of a truncated Taylor expansion for the particle's position at the next timestep $t + \delta t$, given its current position:

$$\vec{x}(t+\delta t) = \vec{x}(t) + \vec{v}(t)\delta t + \frac{1}{2}\vec{a}(t)\delta t^2. \tag{2.1}$$

In Eq.(2.1), $\vec{v}(t)$ represents the velocity and $\vec{a}(t)$ is the particle's acceleration at the current timestep. The velocity for the subsequent timestep is obtained in a similar manner:

$$\vec{v}(t+\delta t) = \vec{v}(t) + \frac{1}{2}\delta t\left[\vec{a}(t) + \vec{a}(t+\delta t)\right], \tag{2.2}$$

where we have used the Taylor expansion of the acceleration to obtain Eq.(2.2). To be consistent with the Nosé-Hoover thermostat (see Section 2.1.3), this operation is undertaken in two stages in the code, as shown in Figure 2.1. The first velocity update (over half a timestep) is done at the same time as the position update, giving $\vec{v}(t+\frac{1}{2}\delta t) = \vec{v}(t) + \frac{1}{2}\delta t\vec{a}(t)$. Subsequently, the forces are evaluated based on the positions at time $t+\delta t$, enabling us to complete the velocity update by advancing another half timestep: $\vec{v}(t+\delta t) = \vec{v}(t+\frac{1}{2}\delta t) + \frac{1}{2}\delta t\vec{a}(t+\delta t)$.

2.1.3 Thermostats

The velocity Verlet algorithm conserves energy and therefore the procedure outlined so far would simulate a system in the micro-canonical (NVE) ensemble. To study osmosis, however, we would like to simulate in the canonical (NVT) ensemble – because experiments are carried out at constant temperature, not constant energy. Therefore, we need to employ auxiliary devices to maintain a constant temperature in the system; it is preferable that in doing this the particles' dynamics are only weakly perturbed. In this thesis, the Nosé-Hoover [64, 110, 111], Andersen [6], and Nosé-Hoover Langevin thermostat [79] have been used.

The Andersen thermostat

An Andersen thermostat aims to mimic random collisions with a "heat bath"; for which the probability distribution for the times between collisions is assumed to be

$$P(t) = \nu \mathrm{e}^{-\nu t}, \tag{2.3}$$

in which $P(t)\delta t$ is the probability that a collision will occur in the time window $[t, t+\delta t]$ and ν is the collision frequency. This method is implemented by adding a statement into the velocity update in which, for each particle, you pick a random number between zero and one and check if it is smaller than the product $\nu\delta t$. If it is, then a random new velocity is picked from the Maxwell-Boltzmann distribution:

$$P(v_{\alpha i}) = \sqrt{\frac{m}{2\pi k_B T}} \ \mathrm{e}^{-\frac{m v_{\alpha i}^2}{2k_B T}}, \tag{2.4}$$

where $v_{\alpha i}$ is the α component of the i^{th} particle's velocity, and m, k_B and T are the mass, Boltzmann's constant and the desired temperature of the system, respectively. If, however, the random number is greater than $\nu\delta t$, then you update according to Eq.(2.2). The Andersen thermostat has the following advantages: it samples from the canonical ensemble; it is computationally inexpensive; and it is easy to implement. One particular disadvantage of this thermostat, however, is that, since the algorithm randomly accelerates and decelerates particles (which can violate the weak perturbation condition discussed above), it is not physical; thus, dynamical properties, such as the diffusion coefficient and auto-correlation functions, are not properly reproduced when using this thermostat. Further information on the Andersen thermostat can be found in [6, 44].

The Nosé-Hoover thermostat

The Nosé-Hoover thermostat is more "gentle" than the Andersen method because it does not randomly re-assign particle velocities; instead it "steers" them to the correct temperature. In this method, the Lagrangian for the system is extended to include an artificial co-ordinate, s [44]:

$$\mathcal{L} = \sum_{i=1}^{N} \frac{m_i}{2} s^2 \dot{\vec{r}}_i^{\,2} - U(\vec{r}^{\,N}) + \frac{Q}{2}\dot{s}^2 - \frac{L}{\beta}\log s, \tag{2.5}$$

where L is the number of degrees of freedom of the particles and Q is an effective "mass" [44] associated with s, which determines the strength of the particles' coupling to the heat bath. The resulting (real-space) Hamiltonian for the system can then be derived following the procedure outlined in [44]. The result is:

$$\mathcal{H} = \sum_{i=1}^{N} \frac{\vec{p}_i{}^2}{2m_i} + U(\vec{r}^{\,N}) + \frac{\xi^2 Q}{2} + \frac{L}{\beta}\log s, \tag{2.6}$$

in which $\xi = \frac{d\log s}{dt}$. From a practical point of view, the evolution of the positions and velocities (Eqs.(2.1) and (2.2)) are modified as follows [90]:

$$\vec{x}(t+\delta t) = \vec{x}(t) + \vec{v}(t)\delta t + \frac{\delta t^2}{2}\left[\vec{a}(t) - \vec{v}(t)\xi(t)\right], \tag{2.7}$$

and

$$\vec{v}(t+\delta t) = \vec{v}(t) + \frac{1}{2}\delta t\left[\vec{a}(t) - \vec{v}(t)\xi(t)\right] + \frac{1}{2}\delta t\left[\vec{a}(t+\delta t) - \vec{v}(t+\delta t)\xi(t+\delta t)\right]. \tag{2.8}$$

Because we have $\vec{v}(t+\delta t)$ on both sides of Eq.(2.8), the velocity and the ξ variable are determined iteratively, according to:

$$\begin{aligned} \vec{v}^{k}(t+\delta t) &= \frac{1}{(1+(\delta t/2)\xi^{k-1}(t+\delta t))} \\ &\qquad \times \left\{\vec{v}(t) + \left[\vec{a}(t) - \vec{v}(t)\xi(t) + \vec{a}(t+\delta t)\right]\frac{\delta t}{2}\right\}, \\ \xi^{k}(t+\delta t) &= \xi(t) + \left[\dot{\xi}(t) + \dot{\xi}^{k}(t+\delta t)\right]\frac{\delta t}{2}, \end{aligned} \tag{2.9}$$

where k denotes the current iteration and an initial guess of $\xi^0(t+\delta t) = \xi(t-\delta t) + 2\dot{\xi}(t)\delta t$ is used. Full details of the steps used to implement this thermostat within the velocity Verlet integrator can be found in Appendix 2 of [90]. Using this formalism, and assuming that there are no external forces and that the centre of mass is fixed, a canonical ensemble is simulated and Eq.(2.6) represents a quantity which should be conserved in time.

The Nosé-Hoover thermostat has been proven to generate a canonical ensemble in a variety of systems. It is relatively simple to implement and because the velocities are not randomly re-assigned it is more physical than the Andersen method. However, the Nosé-Hoover thermostat does not work when simulating "stiff" systems – the oft-quoted example is the 1D harmonic oscillator [79, 89]. In these systems ergodicity (a

necessary assumption in demonstrating that we sample from the canonical ensemble) is no longer satisfied, *i.e.* temporal and spatial averages are no longer equivalent.

The Nosé-Hoover Langevin thermostat

Creating a chain of Nosé-Hoover thermostats [89] is the canonical choice for overcoming the ergodicity problems associated with the Nosé-Hoover thermostat. However, for the purpose of this thesis, I was interested in exploring alternative methods. Moreover, the Nosé-Hoover Langevin technique has the distinct advantage over Nosé-Hoover chains that it is very simple to incorporate into a MD code. The key addition in the Nosé-Hoover Langevin method is that the thermostat now evolves stochastically, according to the following Langevin equation:

$$\frac{d\xi}{dt} = \frac{1}{Q}\left(\sum_i \frac{|\vec{p}_i|^2}{m_i} - Lk_BT\right) - \gamma\xi + \sqrt{\frac{2\gamma k_BT}{Q}}\frac{dW}{dt}. \tag{2.10}$$

The first term on the right hand side of Eq.(2.10) is the typical "steering term" carried over from the standard Nosé-Hoover thermostat (T being the desired temperature), the second term damps the thermostat (the strength of the damping is controlled by γ) and the final term, in which W describes a Wiener process [166, 167], involves adding some Brownian noise to the thermostat, similar to $\vec{F}_B$ in Eq.(1.13). In practice this thermostat is implemented by the addition of the following line in the code both before and after the position and velocity update,

$$\xi_{new} = \mathrm{e}^{-\gamma\delta t/2}\xi_{old} + \sqrt{\frac{k_BT}{Q}(1-\mathrm{e}^{-\gamma\delta t})}\eta, \tag{2.11}$$

where η is chosen at random from a normal distribution and γ is set equal to 1.0 when used in this thesis. To test the thermostat has been successfully implemented we can set $\gamma = 0$ and make sure that the standard Nosé-Hoover thermostat is recovered. Furthermore, if the noise has been successfully incorporated into the thermostat, the ξ variable should be distributed according to a Gaussian relation: $\sqrt{\frac{Q}{2\pi k_BT}}\mathrm{e}^{-\frac{Q\xi^2}{2k_BT}}$.

2.1.4 Further technical considerations associated with MD

Periodic boundary conditions

A commonly employed trick in molecular simulations of bulk liquids — for which surface effects can arise due to the nature of the forces at the edge of the simulation box compared to the bulk — is the method of periodic boundary conditions. Using this technique, a particle which is projected to pass through one face of the simulation box at time $t + \delta t$ will in fact re-enter through the opposite face at the next timestep. This means that we are in fact simulating an infinite periodic lattice of replicates of our simulation box. Thus, to compute the interaction between two particles, A and B, the nearest periodic image of B is taken. Care must be taken when using this method, however, that particle interactions do not span a length greater than $L/2$, where L represents the length of the simulation box.

Neighbour lists

A neighbour list is a method for speeding up the time it takes to carry out by far the most time consuming part of almost every MD simulation: the force calculation. Naïvely, we might calculate the force by summing over all pairs of particles contained within our simulation box; an order N^2 operation. A neighbour list provides a significant speed up in this part of the simulation by storing, for each particle, all of the particles that are nearby (within a radius determined by the range of the interaction potential). This list is updated every n timesteps, where $n = 60$ in my simulations. The great benefit of using this method is that, at each timestep, we only have to look over the few particles contained within the list to see if their separation is less than the range of the interaction potential, making the force calculation of order N rather than N^2. In my simulations, using a neighbour list results in a speed-up of about a factor of 3.

Reduced units

Finally, in my simulations I also employ "reduced units". Thus, in all of the simulations the mass of the particles is set equal to one. As a result, the momentum of a particle is equal to its velocity and the force is equal to the acceleration. Other units are defined in terms of parameters associated with the interaction potential – the particle diameter,

Table 2.1 Relation between reduced (*starred*) and real (*unstarred*) units.

Unit	Conversion
Density	$\rho^* = \rho\sigma^3$
Temperature	$T^* = k_B T/\epsilon$
Pressure	$P^* = P\sigma^3/\epsilon$
Time	$t^* = (\epsilon/m\sigma^2)^{1/2}t$
Force	$\vec{f}^* = \vec{f}\sigma/\epsilon$

σ, and the interaction energy, ϵ. To recover the real units we need simply apply the appropriate conversion factors. Table (2.1), taken from [4], demonstrates the conversion of several reduced units to real units.

2.2 Data analysis

2.2.1 Data analysis using Python

During the simulation various quantities, such as the pressure, the temperature, and the numbers of particles in certain regions, are recorded to disk for later analysis. This analysis is conducted using Python. Here I briefly comment on the merits of using this language.

At the core of its philosophy, Python is a language which promotes code readability and whose syntax is clear, yet concise. Simple tasks can be conducted with the minimal amount of code. For example, say we want to read in a file which contains data in a series of columns and then take the average of a particular column; perhaps we are interested in calculating the average pressure in our simulation. On the LHS of Figure 2.2, I have included a screen shot of the code needed to perform part of this operation in C++, and on the RHS of Figure 2.2, the equivalent piece of code necessary to achieve the same result when using Python. Clearly the Python syntax is easier to read; also it does not require the inclusion of the *boost* library. Python also has a vast array of libraries at its disposal, including *SciPy*, which contains modules for statistics, optimisation, integration, linear algebra, Fourier transforms, etc., whereas a detailed knowledge of a textbook such as Numerical Recipes [124] might be required in C++. Finally, string handling in Python is far simpler. For example, in Figure 2.2 we see that the *split*() and *strip*() functions are far more simply implemented in Python than in C++.

```
do{
    string line;
    getline(fi,line);
    if (!boost::starts_with(line, "#") && !line.empty()){
        vector <string> lineparts;
        boost::split(lineparts, line, boost::is_any_of("\t"));
        data.push_back(boost::lexical_cast<double>(lineparts[2]));
    }
} while (fi.good());
```

```
for line in fi:
    if not line.startswith('#') and line.strip():
        data.append(float(line.strip().split()[2]))
```

Figure 2.2 Snippets of the C++ and Python codes used to process a file. On the LHS a segment of C++ code is shown, utilising the *boost* library for string handling as the data is copied into a vector. On the RHS of the figure, the equivalent code required for this operation using Python is shown. No modules need to be imported to perform the equivalent operation in Python.

2.2.2 Measuring structural and dynamical quantities

In later chapters I present results based on the diffusion coefficient and radial distribution functions. Thus, I include here a description of the methods used to calculate these quantities.

The diffusion coefficient

In Section 1.2.1 the diffusion coefficient was discussed as a constant of proportionality in Fick's macroscopic law of diffusion (Eq.(1.10)), where it represented a measure of the rate of transport through space due to thermal processes. However, starting from a microscopic viewpoint and assuming the particles obey a random walk motion, we can derive a new relation in terms of the mean square displacement of a particle $\left\langle |\vec{r}(t) - \vec{r}(0)|^2 \right\rangle$. In three dimensions this is given by:

$$\left\langle |\vec{r}(t) - \vec{r}(0)|^2 \right\rangle = 6Dt, \tag{2.12}$$

where, as in Section 1.2.1, D represents the diffusion coefficient in units of $length^2/time$. In practice we extract values for the mean square displacement in our simulations by recording the trajectories of particles through time. By plotting this quantity versus time we can extract the gradient at times beyond the ballistic regime (*i.e.,* where $\left\langle |\vec{r}(t) - \vec{r}(0)|^2 \right\rangle$ is linear) and thus determine the diffusion coefficient, D.

The radial distribution function

The radial distribution function, $g(r)$, can be used to infer information on the local structure of a fluid. The product $\rho g(r)$, where ρ is the average density in the simulation, can be interpreted as the conditional probability density that a particle be found at a radial separation r given that another particle is situated at the origin. To calculate the $g(r)$, a line can be included in the code when updating the neighbour list (see Section 2.1.4) which increments the number in an array, whereby each element in the array corresponds to the number of particles in the range $[r,\ r + \delta r]$ from a central particle. This is then normalised at the end of the simulation by dividing the number in each bin by the product of: the number of timesteps for which values have been entered into the array for the $g(r)$; the number of particles which would be in the bin were the fluid an ideal gas; and the number of particles for which the $g(r)$ is being calculated.

2.2.3 Estimating errors using the bootstrap technique

Finally in this chapter I discuss the method used to calculate the error on the data presented throughout this thesis, the bootstrap method. The bootstrap method [37, 38] is a statistical technique in which the data set is resampled to determine the uncertainty in a particular value; it is a generalisation of an earlier proposed technique, the jackknife [127, 128]. I illustrate it here with the following example.

We start by measuring some quantity, the temperature, say, very many times, thus obtaining a data set $T_1, T_2, ..., T_N$. This data is then resampled at random until a new data set is obtained, $\bar{T}_1^* = T_2, T_4, T_1, T_4, T_{N-1}, ..,$ which has the same number of entries as the original data set. Also note here that the same value may be picked twice. From this resampled data the mean value, μ_1^*, is calculated and this procedure is repeated many times ($\geq$ 1000 for all of the results presented in this thesis) until a new distributions of means is built up: $\mu_1^*, \mu_2^*, ..., \mu_{1000}^*$. The resulting distribution should, ideally, be normally distributed. From this distribution the standard deviation is calculated and reported alongside the actual average temperature as a measure of our confidence in the average value.

It is advantageous to use this method when calculating the uncertainty in a complex function for which we would normally have to propagate errors. A commonly reported issue with the technique is the time spent resampling the original data set; however, the author has not had such issues in the course of his studies. Additionally, it should

be noted that this technique is not reliable when the variable under consideration does not fluctuate around a consistent mean value.

Chapter 3

Simulating Osmosis

Computer simulations provide a useful tool for studying osmosis, since they allow one to study in detail the motion of, and forces acting on, individual particles. Yet computer simulations of osmosis appear relatively rarely in the literature. In this chapter I first discuss the simulations which have been conducted to date. Broadly speaking, the literature can be divided into studies which have explored the steady-state osmotic pressure and solvent dynamics, and more recent studies into the solvent flow across the membrane prior to the steady state. I then present, in the second half of the chapter, the details of the simulations used throughout this thesis. In particular, I discuss the geometries, particle interactions and the parameters used; a section on measuring the osmotic pressure is also included.

3.1 Previous simulations

3.1.1 Simulations of osmosis during the steady state

Murad and Powles were the first to use MD and Monte Carlo (MC) simulations to study the steady-state osmotic pressure [103–105]. As well as reproducing the van 't Hoff relation, Murad and Powles further demonstrated, in a MC study of a Lennard-Jones (LJ) system [104] (see Section 3.2.1) with different solute:solvent size (σ_B/σ_A) and interaction (ϵ_B/ϵ_A) parameters, that the osmotic pressure can deviate quite markedly from the linear law of van 't Hoff; see Figure 3.1. As discussed in Section 1.2.2 this may be reconciled using a concentration-diffusion model for osmosis, where a larger solute:solvent diameter ratio implies a larger initial solvent density gradient across the

membrane and, thus, a larger resulting osmotic pressure difference. Remarkably, the authors even reported results of negative osmotic pressures (see the data set labeled 4 in Figure 3.1); this claim was later retracted [120] upon the realisation that these particular simulations were not fully equilibrated.

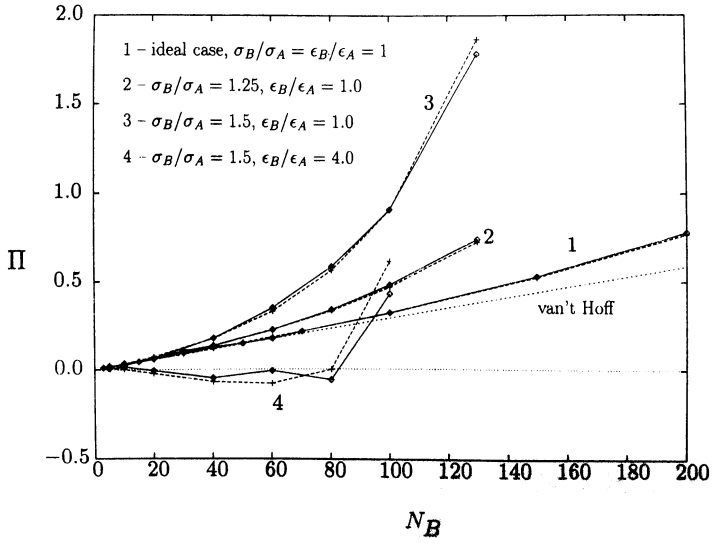

Figure 3.1 The osmotic pressure is displayed as a function of the number of solute particles in the solution for a range of simulation parameters. By adjusting the solute:solvent particle diameter ratios (σ_B/σ_A) and interactions parameters (ϵ_B/ϵ_A), very different results for the osmotic pressure are obtained. The figure is taken from [104].

Although minimal models (*i.e.* simple interaction potentials and membranes) were primarily employed by Murad and Powles, more applied aspects of osmosis were also considered [121, 122]. For example, it was proposed that an osmotic setup could be used to measure the activity coefficient of a solution [121] and it was discovered that the formation and break up (through an electric field) of water clusters in a solution can affect the rate of solvent transfer in osmosis [122]. More recently, the osmotic pressure has been used as a method for testing force fields in simulation packages [87].

The steady-state solvent dynamics in osmosis have been studied by Itano *et al.* [67] using MD simulations of a LJ system. Of particular interest to the authors was the influence that the solvent-solute interactions have on the solvent dynamics at the membrane. They proposed that the inability of the solute to diffuse out of the solution allowed the solvent in the bath, near to the membrane, to exert a net negative force on the solvent in the solution, decreasing the overall pressure in the solution compartment[1]. Thus, a flow of solvent into the solution compartment takes place

[1]This is similar to the previously proposed interaction models of Hammel and Scholander discussed

until the inward and outward pressures are balanced across the membrane – the steady state. In an indirect sense, the role of the solute here is to draw solvent into the solution compartment, as has been proposed by others [54, 130]. However, as we shall see in the next section, osmosis takes place in systems containing hard sphere particles [76] and so any explanation based on the specific interactions between different particles cannot constitute a minimal explanation of the phenomenon. It would nevertheless be of interest to further investigate how the various inter-particle interactions affect the components of the osmotic pressure; for example, comparison could be made between a system which has purely repulsive interactions to one which maintains both attractive and repulsive interactions.

3.1.2 Simulations of the solvent flow prior to the steady state

Recent simulations of osmosis have predominantly concentrated on studying the solvent dynamics across a (typically porous) membrane prior to the steady state. These studies have usually been conducted using the MD method and both realistic setups (*i.e.* taking water as the solvent and a charged salt as the solute) and minimal model systems, in which the particle interactions are kept simple, have been considered. However, perhaps the earliest simulation study, conducted by Flekkoy *et al.* [43], used a lattice gas setup to study the solvent flow in osmosis. By introducing position dependent porosity, a linear relationship between the mass current of solvent particles across the membrane and the increasing concentration of solute particles was recorded. This is to be expected if we consider the Kedem-Katchalsky relation (Eq.(1.11)) discussed in Section 1.2.1 and it is also an experimental fact, see for example [92, 93, 156].

In a significant contribution, Kim *et al.* used MD simulations to study the osmotic flow of hard sphere particles through a straight cylindrical pore [76]. A movable constriction was placed in the pore, which inhibited the flow of solutes past it, and the resulting osmotic flux was recorded as a function of the position at which this was placed; the results are shown in Figure 3.2. The mass current of solvent was observed to vary linearly with increasing solute concentration, as previously noted by Flekkoy *et al.* and others. But these authors further noted that solute permeation into the pore acted to reduce the solvent flux prior to the steady state, from the results labeled $C15$ in Figure 3.2(a) to the results marked $C1$. By varying the solute:pore radius ratio, a transition in the flux was also observed, see Figure 3.2(b), between pores that are permeable to the solute (the region marked P in the figure) and those that are impermeable to the

in Section 1.2.2.

solute (the region marked S in the figure). This is consistent with the predictions of Chou discussed in Section 1.2.2. It is also interesting to note that the flux continues to increase, for increasing solute:pore size ratios, even after the pore becomes impermeable to the solute particles.

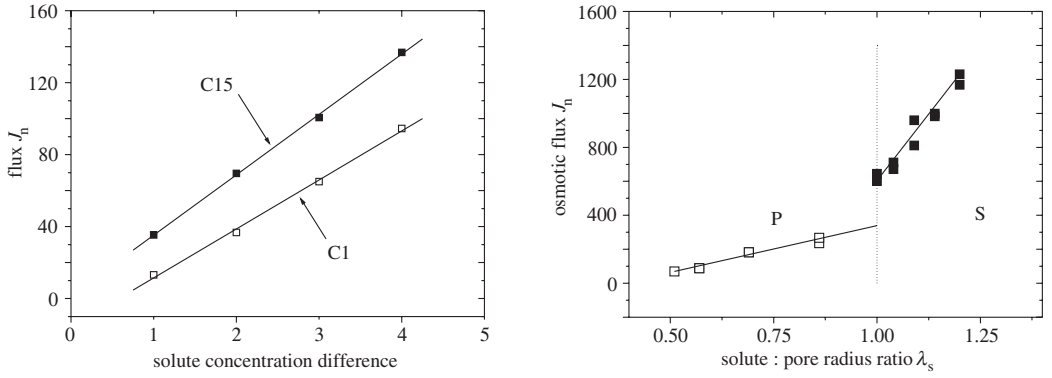

Figure 3.2 Panel (a) shows the osmotic flux versus the solute concentration difference across the membrane. The upper data marked $C15$ represents simulation results where a constriction, inhibiting the flow of solute, has been placed inside the pore, near to the entrance of the solution reservoir. The lower data marked $C1$ represents results from simulations where the same constriction has been placed at the other end of the pore, near to the solvent only reservoir. In panel (b) the osmotic flux has now been plotted as a function of the solute:pore radius ratio, λ_s. Data shown in the region marked P corresponds to those instances where the membrane allows the entry of solute particles into the pore. On the other hand, in the region marked S, the solute is completely excluded from the pore. In each instance, a line of best fit is also plotted alongside the data. Both figures are taken from [76].

The authors then compared the results from their osmotic simulations to those when no solute particles were present in their solution, but a pressure difference existed between the two compartments (see Figure 3.3(a)), and to the results that would be expected for a purely diffusive process (see Figure 3.3(b)). It was subsequently demonstrated that flows driven by a hydrostatic or osmotic pressure difference are equivalent (see Figures 3.2(a) and 3.3(a)) and, by comparison with Figure 3.3(b), that these flows are markedly driven from those that are expected for a purely diffusive process. It would be of interest to further study, using a membrane for which the solvent flux can be accelerated or decelerated, the nature of the transition between diffusive and pressure driven flows in osmosis.

Raghunathan and Aluru also looked at the mechanism of solvent transport prior to the steady state in a more detailed MD study of osmosis using a realistic model for water in combination with a charged porous membrane [131]. It was discovered that the solvent

flow is fastest in this setup when negatively charged pores are used. A later work by the same authors demonstrated that using KF or KCl as the solute particles resulted in a higher osmotic flux of water through a porous membrane than when using NaCl or LiCl [130].

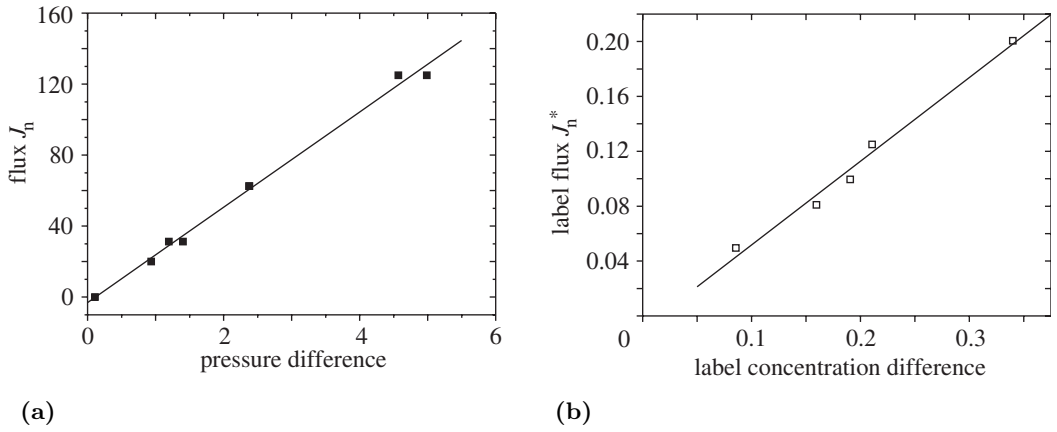

Figure 3.3 The flux of solvent under (a) a hydrostatic pressure gradient and (b) a gradient in the concentration of labeled particles. In the second case the results are for a purely diffusive system as there is no chemical potential gradient across the membrane. The squares represent data taken from simulations and the line indicates a line of best fit. Figures are taken from [76].

In molecularly narrow pores, a further factor can significantly enhance the solvent flow through the membrane. By forming a single-file chain, water has been shown [9, 70, 150, 151] to "slip" through the pore. This effect can be described using a 1D random walk model [70] and provides an explanation for previously reported experimental results [42, 82] (see Section 1.2.1). These results may have important consequences for the use of osmosis in industry [1, 109, 144], as described in Section 1.4.

In conclusion, there have been relatively few simulation studies into osmosis. In this thesis I attempt to address this deficiency. Using a simple minimal model, I consider in detail the nature of the particular particle interactions during the steady state, further exploring how these maintain the total particle density gradient across the membrane. Then, by slowing down the relaxation to the steady state and using a simple model for the membrane, I explore the nature of the solvent flow prior to the steady state, examining the transition between diffusive and non-diffusive flows as the membrane barrier is adjusted. Finally, in a novel take on the classic osmosis experiment, I also consider simulations in which the solute particles are active. These represent a new and interesting avenue for further exploration and, in combination with the work on nanoscale, porous membranes discussed above, may have future industrial applications.

3.2 Simulating osmosis in this thesis

Here I describe the setup used to study osmosis throughout this thesis. Emphasis is placed on simulating osmosis in as simple a setup as possible to isolate those effects which are necessary for osmosis to take place from those which simply facilitate the solvent transfer or increase/decrease the resulting osmotic pressure.

3.2.1 Minimal interactions

We are interested in simulating the simplest possible model of osmosis, avoiding any complications that may arise due to the specific nature of the solvent or solute particles. To this end, in the majority of the simulations presented, the particles interact symmetrically with one another through the Weeks, Chandler, Andersen (WCA) potential. The WCA potential is a shifted and truncated Lennard-Jones potential, defined as follows:

$$U_{WCA} = \begin{cases} 4\epsilon((\frac{\sigma}{r})^{12} - (\frac{\sigma}{r})^{6}) + \epsilon & \text{if } r < 2^{\frac{1}{6}}\sigma, \\ 0 & \text{if } r \geq 2^{\frac{1}{6}}\sigma, \end{cases} \tag{3.1}$$

where ϵ and σ are the interaction energy and diameter of the particles (see Section 2.1.4), respectively. This potential is plotted, alongside the Lennard-Jones potential, in Figure 3.4. The particles interact strongly when they come within a certain distance ($2^{1/6}\sigma$) and do not interact otherwise. Thus, the WCA potential can be thought of as a slightly soft, hard sphere interaction. Indeed it will be shown in subsequent chapters that the results obtained from simulations using this potential are similar in nature to those of an equivalent hard sphere system, for which the Carnahan Starling relation [16], $P/\rho k_B T = (1 + \eta + \eta^2 - \eta^3)/(1 - \eta)^3$, where ρ is the density and η the packing fraction ($= \pi\sigma^3\rho/6$), provides a good approximation to the equation of state. Thus, the Carnahan and Starling relation can be used together with standard thermodynamic relations to derive analytical results (for example for the density difference across the membrane) which can be compared with the results from our simulations of WCA particles.

Osmosis is achieved in our system of WCA particles through the implementation of a semi-permeable membrane, permeable to the solvent particles, but completely impermeable to the solute particles. This membrane divides the simulation box into

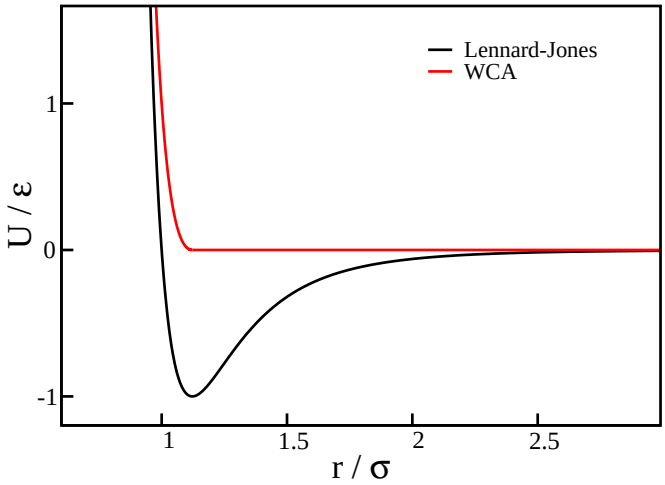

Figure 3.4 The interaction potential felt by two particles as a function of their radial separation. Shown in black is the well-known Lennard-Jones interaction, often used to simulate liquid matter. This potential has been shifted in the $y-axis$ by $+\epsilon$ and cut off at the minimum in the potential, $r = 2^{\frac{1}{6}}\sigma$; the result is the WCA potential shown in red.

a solution and a solvent bath compartment; the solution contains both solute and solvent particles and the bath contains only solvent particles. In this thesis we use two different membrane geometries, referred to from here onwards as the "box in box, invisible membrane" geometry and the "double box, finite membrane" geometry.

3.2.2 Simulation geometries

The "box in box, invisible membrane" setup

This setup is used when studying the steady-state properties of osmosis because it allows for a fast equilibration of the system. We achieve this by placing the solution compartment in the centre of a solvent bath. Periodic boundary conditions, as discussed earlier in Section 2.1.4, are implemented at the edges of the cubic (*i.e.* $L_x = L_y = L_z = L$) simulation box. The solution is separated from the solvent bath by a membrane that takes the form of a continuous potential barrier. To further speed-up the equilibration of the system, the membrane remains visible to the solute particles, but is completely invisible to the solvent particles. The exact form of the barrier potential is $U_{mem} = k_B T(\sigma/d)^9$, where k_B is Boltzmann's constant, T is the temperature, σ is the particle diameter and d is the perpendicular distance between the particle and the boundary of the compartment. The force that the solute particles experience is then obtained from the gradient of the potential, $\vec{F}_{mem} = -\vec{\nabla}U_{mem}$. For the corners, the interactions with each wall are evaluated separately and summed.

An overview of this setup is given in Figure 3.5, which shows a 3D schematic and a 2D slice through the simulation box. Figure 3.6(a) shows the confining potential that a solute particle experiences in the $y - z$ plane, at $x = 0.5L$. Figure 3.6(b) shows the confining potential and force that a solute particle is subject to as it is moved through the box in the x direction at a fixed y and z position ($y = z = 0.5L$) — this corresponds to the centrally located $\odot$ in Figure 3.5(b). In a similar manner, the force and potential have also been tested by moving particles through the simulation box for each of the positions marked as $\otimes$ in Figure 3.5(b) to ensure that the potential is continuous around the solution compartment and that the force returned from the membrane function is the gradient of the potential.

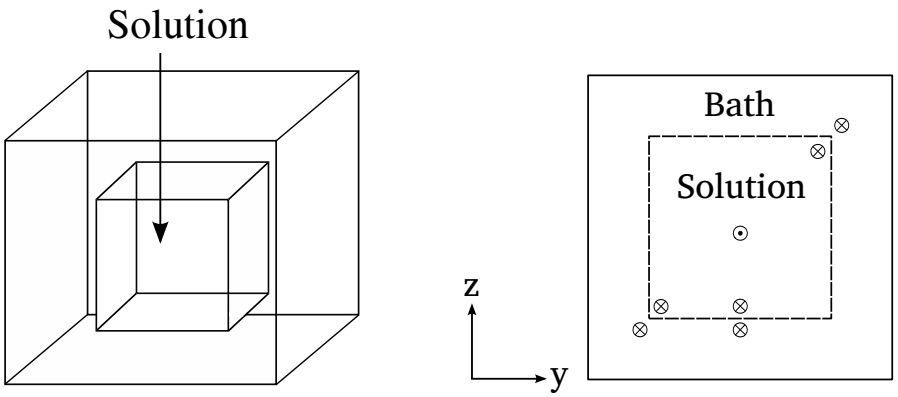

Figure 3.5 (a): A 3D schematic of the setup used. The solution compartment is embedded in a solvent bath. Panel (b) shows a 2D slice through the simulation cell at $x = 0.5\ L$. The barrier has been tested to ensure that the potential is continuous and that the force is the gradient of the potential for all of the positions marked by circles with crosses through them ($\otimes$) in the figure.

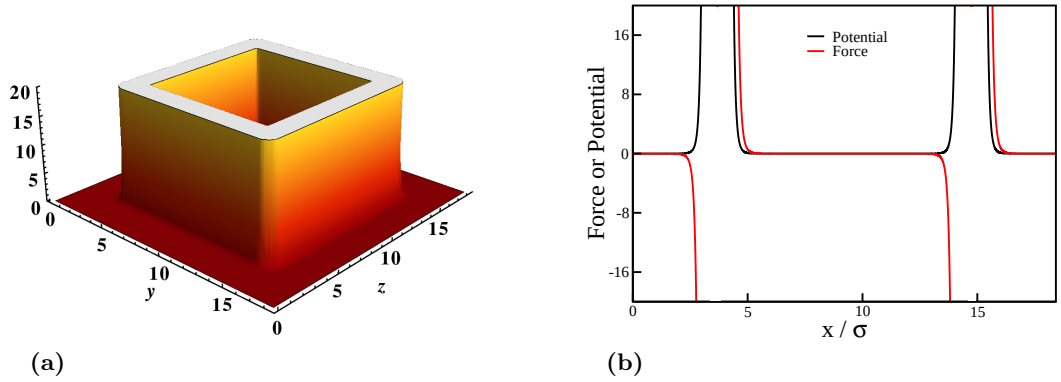

Figure 3.6 (a): The potential experienced by a solute particle as a function of its y and z position for fixed $x = 0.5L$. (b): The potential and force as a function of a particle's position along the x axis; y and z are fixed at $0.5L$ (see central $\odot$ marked in Figure 3.5(b)).

Determining the box in box, invisible membrane solution volume

The solution volume is used later on to compute the concentration of solute particles in the solution, and also to determine the osmotic pressure. However, defining the solution volume is nontrivial because the potential used to confine the solute particles within the centrally located solution compartment is smooth; consequently the probability density for the solute particles decays smoothly close to the confining boundary. The volume is determined by matching the pressure-density relation for a "gas" of solute particles, confined in the solution compartment in the absence of solvent, to that of a system of equivalent particles simulated in a periodic box. The result is shown in Figure 3.7(a); the closed circles show the pressure-density relation of a system of confined particles, for which the volume has been adjusted to match the pressure-density relation for a system of particles in a periodic system (open circles in Figure 3.7(a)). This results in an effective boundary of the solution compartment which lies $0.91^{+0.07}_{-0.02}\sigma$ inside the point where the confining potential diverges. The error on this value has been determined by performing a $t-test$ [22] to ensure that the two pressure-density relations (the periodic and confined) are within statistical agreement of one another relative to the Carnahan-Starling equation of state, which describes the pressure-density relation for hard-spheres – the pressure of a hard sphere system is practically identical to the pressure of a WCA system at lower densities. Further details of this procedure can be found in Appendix A.

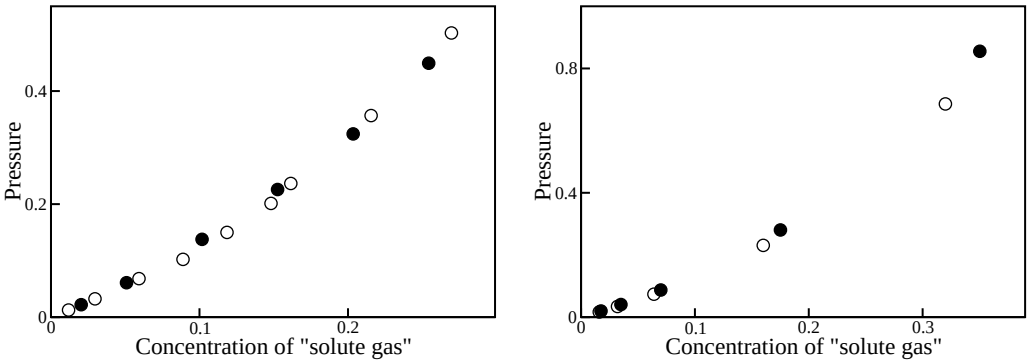

Figure 3.7 The pressure for a gas of solute particles is shown as a function of increasing density in both (a) and (b). In (a) the result is shown for the box in box, invisible membrane setup. The closed circles in the figure have been shifted along the $x-axis$ until they are in agreement with the open circles. The effective volume of the solution compartment is established by measuring the extent to which the confined data must be shifted along the $x-axis$ (see main text). In (b) similar results are shown for the double box, finite membrane setup. The shift along the $x-axis$ for the confined data is, however, here determined by taking the average bulk concentration of solute particles in actual simulations (see main text for further details).

The "double box, finite membrane" setup

The double box, finite membrane setup is used when studying the osmotic relaxation to the steady state. Here we want to slow the solvent dynamics down, using a membrane which is both simple and easy to manipulate so that we can characterise the solvent-membrane interactions in as simple a manner as possible. This is best achieved by dividing the simulation box into two identical compartments, one of which contains both solute and solvent particles, the solution, and the other which contains only solvent particles, the solvent bath. The geometry is illustrated in Figure 3.8(a). The solution and the solvent bath are separated by a barrier that is impermeable to the solute particles (as above); however, in contrast to the previous setup, the solvent particles do not pass freely across the membrane but rather experience a finite potential barrier. This mimics, for example, a membrane with narrow pores through which the solvent has to pass. The barrier divides the simulation box in half along the long axis (barriers are centred at $x = 0 = L_x$ and $x = 0.5L_x$, as illustrated by the dashed lines in Figure 3.8(a)). Periodic boundary conditions are implemented in the x, y and z directions; also note that the double box is symmetric about $x = 0.5L_x$, as $L_y = L_z = 0.5L_x$.

In Figure 3.8(b) the confining potential and the corresponding force which the solvent particles experience are shown for a 15 k_BT barrier. The barrier is implemented as follows:

$$U_{solvent-membrane} = \begin{cases} k_BT(\frac{\sigma}{d})^9 & \text{if } d \geq \Delta, \\ H - \frac{1}{2}\kappa d^2 & \text{if } d < \Delta. \end{cases} \tag{3.2}$$

In Eq.(3.2), H is the barrier height, k_BT and d are defined as previously, Δ represents a distance from the membrane, and κ is a constant. Δ and κ are both carefully chosen so that the potentials and forces are everywhere continuous. This is achieved by setting:

$$\begin{aligned} \Delta &= \frac{11}{2}k_BT\frac{\sigma^9}{H^{\frac{1}{9}}}, \\ \kappa &= 9k_BT\frac{\sigma^9}{\Delta^{11}}. \end{aligned} \tag{3.3}$$

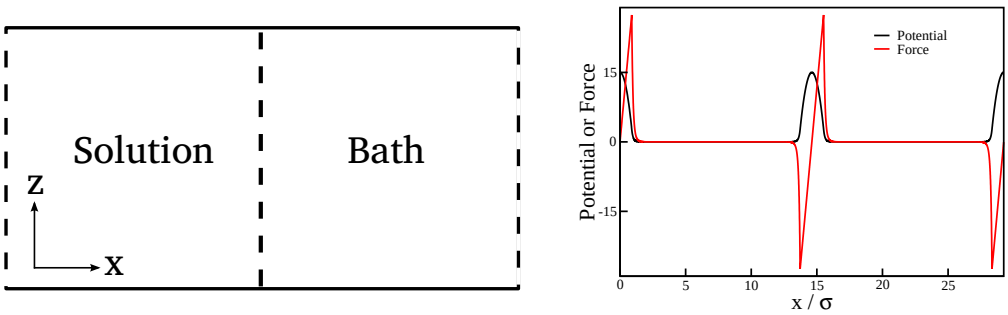

(a) **(b)**

Figure 3.8 Panel (a) contains a diagram illustrating the double box, finite membrane setup. The double box is symmetric in the x direction, as the solvent bath represents a mirror image of the solution. The dashed lines illustrate the positions of the barrier and periodic boundary conditions are implemented in all three directions. In (b) the potential and force that a solvent particle experiences as a function of its x position in the simulation is shown for a $15k_BT$ barrier. As the simulation is periodic in x, the potential and force at $x = 0$ should line up with the potential and force at $x = L_x$. This is indeed the case as illustrated in the figure.

Table 3.1 The effective volume of the solution compartment, as determined from the bulk solute concentration, is displayed alongside the corresponding number of solute particles in the solution, N_S.

N_S	Volume
200	2833.47
400	2821.03
600	2868.12
700	2854.47
800	2857.25
900	2876.00
1000	2848.22
1100	2861.55
1200	2877.67

Determining the double box, finite membrane solution volume

In this setup we define the solution volume by a more straightforward procedure than that used in the box in box, invisible membrane case. First, the local density of solute particles in the bulk region of the solution (*i.e.* well away from the confining potential) is recorded for several solute concentrations. For each solute concentration, the effective volume is then calculated by dividing the total number of solute particles in the solution by this density. The results are displayed in Table 3.1. The resulting effective volume and its associated error is then computed from the average and standard deviation of these values. The final result is that the effective solution boundary lies $(0.63 \pm 0.02)\sigma$ inside the point where the confining potential diverges.

The method presented here for calculating the solution volume is simpler than the matching of the pressure-density relations used in the box in box, invisible membrane setup. We can compare the two methods for determining the solution volume in our double box setup by matching the pressure-density relation for a confined solute gas to the result obtained when simulating a periodic solute gas (where the shift is made according to the above volume definition). In Figure 3.7(b) we see that the two results demonstrate excellent agreement with one another, suggesting that the pressure-density technique would have produced the same result for the volume of the solution compartment in the double box setup as that determined via the bulk solute concentrations method used here.

3.2.3 Measuring the osmotic pressure

The osmotic pressure is a crucial output of the simulations in this thesis, I therefore include a brief description of the two methods used to determine the osmotic pressure here.

The method of planes technique

In the first technique, the local pressure is measured inside and outside the solution compartment and the two values are subtracted to give the difference in pressure across the membrane: the osmotic pressure. The local pressure can be measured using the method of planes (MOP) technique (although in Chapter 4 we consider two alternative approaches). The MOP was first proposed by Irving and Kirkwood [66] and later re-derived by Todd *et al.* [155]. In this method, one defines a plane within a local region of interest and monitors the time-averaged flux of particle momentum normal to the plane (due to particles crossing the plane) and the inter-particle forces normal to the plane, for pairs of particles on opposite sides of the plane (see Figure 3.9). For a plane at position $x = x'$, which extends right across the simulation box in the y and z directions, the pressure P is then given by

$$P = \frac{1}{A}\left[\sum_i \frac{p_{xi}^2}{m_i}\delta(x_i - x') + \frac{1}{2}\sum_i \sum_{j>i} [sgn(x_i - x') - sgn(x_j - x')] f_{xij}\right], \qquad (3.4)$$

where A is the area of the plane, the sum is over all pairs of particles (without double counting), x_i and x_j are the x-components of the particle position ($\hat{\mathbf{x}}$ being the normal

to the plane), and p_{xi} and f_{xij} are the normal components of the momentum of particle i and the force between particles i and j, respectively. This method works well when the plane over which the pressure is computed is large, but leads to poor statistical sampling when computing the local pressure in a small region (*i.e.* over a small plane).

This method has been tested by comparing the total pressure in a homogeneous simulation to that computed across a finite plane located within a local region of the simulation. The results, determined over a range of plane sizes, are shown in Figure 3.10(a). For plane sizes $\gtrsim 3\sigma$ the two methods are in excellent agreement, but the results start to deviate when smaller planes are used.

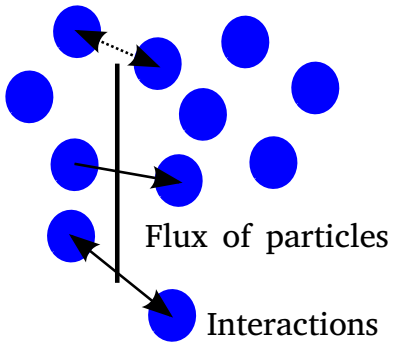

Figure 3.9 Method of planes diagram with a plane of finite extent in the y and z directions. The solid unidirectional arrow indicates those contributions to the pressure as given by Eq.(3.4) from the flux of particles across the plane. Whilst the solid bidirectional arrow denotes those contributions to the interaction part of Eq.(3.4). The contributions from interactions between pairs of particles where the vector joining them does not cross the plane of interest (as in the upper dotted line) do not contribute to the resulting pressure.

The solute-wall force per unit area

The second, arguably simpler method, is to compute the osmotic pressure by summing the forces that the solute particles experience due to the confining membrane (described in Section 3.2.2) and then to divide the result by the membrane area.

The results for the solute-wall force per unit area and the osmotic pressure computed by subtracting the local pressure in the solvent bath from the local pressure in the solution compartment are shown in Figure 3.10(b), when using a box in box, invisible membrane setup, as a function of the solute concentration in the solution. The two methods give results in excellent agreement across the range of solute concentrations considered.

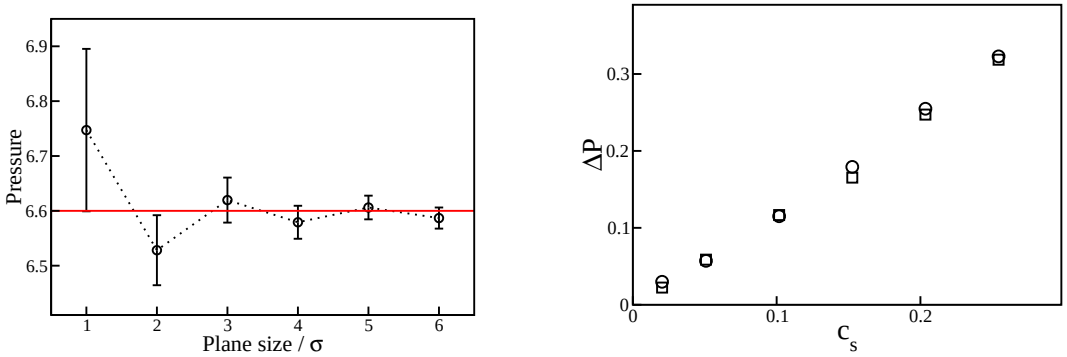

Figure 3.10 In panel (a) the pressure calculated using the method of planes technique (black circles) is shown for a range of plane sizes. For plane sizes $\gtrsim 3\sigma$ the results converge on the "correct" total pressure, the red line in the figure, of the simulation box. In panel (b) a comparison is made between the osmotic pressure as determined by the MOP (black circles) to the solute-wall force per unit area (black squares) for several solute concentrations.

Chapter 4

Measuring the Local Pressure

Before beginning to study osmosis, a detailed investigation into the methods available for measuring the local pressure in MD simulations was first carried out. Such techniques, as well as being of importance in the current work, are also crucial in other systems where knowledge of the pressure in regions of the simulation cell containing perhaps only a few tens of atoms is desired. Examples include calculations of free energies [107, 139], where the difference between the normal and tangential components of the local pressure can be used to deduce the surface tension and thus the free energy in the system, and as a tool for testing coarse-grained hydrodynamic theories [138].

In this chapter I use a fundamental relation, which I denote the "Schweitz virial relation", to derive two equivalent expressions for the local pressure using only simple geometric considerations. The first of these expressions is a well established result (see for example Lutsko [88] and Cormier *et al.* [26]), though its standard derivation is somewhat more complicated than the geometrical method presented here. The second expression is similar in spirit to the method of planes (MOP) pressure of Irving and Kirkwood [66] and Todd *et al.* [155], discussed in the previous chapter (see Section 3.2.3). These expressions are tested using molecular dynamics simulations and are shown to give accurate results for the local pressure in both a homogeneous and in an osmotic setup, even when computed over very small spatial regions. The presentation of the work in this chapter follows closely that published in [83].

4.1 Existing expressions for the pressure

4.1.1 The global pressure in spatially homogeneous systems

For a spatially homogeneous, closed system, the pressure is commonly computed by taking the average of an instantaneous "pressure function":

$$P = \langle \mathcal{P} \rangle = \left\langle \frac{N k_B T}{V} + \frac{1}{3V} \sum_{i=1}^{N-1} \sum_{j>i} \vec{r}_{ij} \cdot \vec{f}_{ij} \right\rangle \tag{4.1}$$

where N, V and T are the number of particles, volume and temperature, k_B is Boltzmann's constant, $\vec{r}_i$ and $\vec{r}_j$ are the positions of particles i and j, $\vec{r}_{ij} \equiv \vec{r}_i - \vec{r}_j$, and $\vec{f}_{ij}$ denotes the force exerted on particle i by particle j [4, 19]; the double sum runs over all pairs of particles, avoiding double counting. The first term in Eq.(4.1) is the kinetic component of the pressure, arising from the particles' kinetic energy. The second term is associated with the inter-particle interactions, which is a function of their instantaneous configuration.

To derive Eq.(4.1) we follow the approach of Allen and Tildesley [4]. We start by defining the following quantity:

$$G = \sum_{i=1}^{N} \vec{r}_i \cdot \vec{p}_i. \tag{4.2}$$

In the above, $\vec{p}_i$ is the momentum and $\vec{r}_i$ the position of particle i. By taking the derivative of Eq.(4.2) with respect to time and assuming we are in the steady state, we arrive at the Clausius virial relation,

$$\left\langle \sum_{i=1}^{N} \frac{|\vec{p}_i|^2}{m_i} + \sum_{i=1}^{N} \vec{r}_i \cdot \vec{F}_i \right\rangle = 0, \tag{4.3}$$

where m_i is the mass of particle i, and $\vec{F}_i$ is the total force acting on particle i, due to the other particles and external forces such as the walls of the container [23, 39]. The first term in Eq.(4.3), $\sum_{i=1}^{N} \frac{|\vec{p}_i|^2}{m_i}$, is then re-written as a function of the particles' temperature using the Equipartition Theorem, which can be expressed as follows:

$$\left\langle \sum_{i=1}^{N} \frac{|\vec{p}_i|^2}{m_i} \right\rangle = 3Nk_BT. \tag{4.4}$$

The second term, $\sum_{i=1}^{N} \vec{r}_i \cdot \vec{F}_i$, is split it into its respective contributions, arising from inter-particle interactions and the confining walls. Upon application of the Divergence Theorem, the average contribution arising from interactions between the confining wall(s) and the particles is re-written as

$$\left\langle \sum_{i=1}^{N} \vec{r}_i \cdot \vec{F}_{iwall} \right\rangle = -3PV, \tag{4.5}$$

where F_{iwall} denotes the wall force on particle i, P is the pressure and V the volume of the cell. This term is taken over to the right hand side of Eq.(4.3) and by dividing through by $3V$ one arrives at the expression for the pressure in the system, Eq.(4.1).

4.1.2 The local pressure in spatially heterogeneous systems

In spatially inhomogeneous systems the pressure in local regions may vary and one must use alternative methods to determine the local pressure. One such method, mentioned in the previous chapter, is the method of planes (MOP) technique (see Section 3.2.3). Alternatively, the local pressure can be measured using a local version of Eq.(4.1). This has the advantage that the region of interest can (in principle) be of arbitrary shape, and that statistical averages are taken over a volume rather than an area. The following local pressure function was proposed by Lutsko [88] and later reformulated by Cormier *et al.* [26] (note that these authors considered the full stress tensor, while, for simplicity here, only the scalar pressure is studied, which is assumed to be locally isotropic):

$$P(\vec{r}) = \frac{1}{3\Omega} \left\langle \sum_{i=1}^{N} \frac{|p_i|^2}{m_i} \Lambda_i + \sum_{i=1}^{N-1} \sum_{j>i} (\vec{f}_{ij} \cdot \vec{r}_{ij}) l_{ij} \right\rangle. \tag{4.6}$$

In Eq.(4.6) Ω is the volume of the region of interest, centred on $\vec{r}$, Λ_i is unity if particle i lies within the volume Ω, and zero otherwise, and l_{ij} is the fraction ($0 \leq l_{ij} \leq 1$) of the line joining particles i and j that lies within Ω (see Figure 4.1). The local pressure expression (4.6) is analogous to the global one (4.1), but with two important differences. Firstly, in the kinetic part of Eq.(4.6), only those particles which are inside the region of

interest (at time t) are included. Secondly, the components of the interaction term are weighted by the fraction of the line joining particles i and j that is inside the region of interest; this highlights the crucial importance of correctly accounting for inter-particle interactions which cross the boundary of the region of interest. Note that particles i and j may both be outside the region yet still contribute to the interaction pressure; see Figure 4.1.

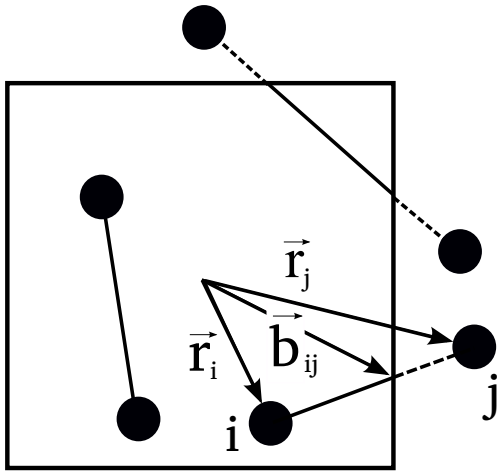

Figure 4.1 Contributions to the interaction part of Eq.(4.6) from different pairs of particles: the fraction l_{ij} of the line joining particles i and j which lies inside the region of interest is shown as a solid line. $\vec{b}_{ij}$ denotes the position where the line joining particles i and j crosses the boundary.

Both Lutsko [88] and Cormier *et al.* [26] derive the stress tensor version of Eq.(4.6) by Fourier transforming the continuity equation for the local momentum flux and applying Newton's second law. In this chapter, a simpler and arguably more intuitive, real space derivation is given, which is directly analogous to the derivation of the global pressure expression, Eq.(4.1), from the Clausius virial relation (4.3).

This derivation leads both to Eq.(4.6) and to a new expression for the local pressure involving the flux of particle momentum across the boundaries of the region of interest, together with cross-boundary interactions. The equivalence between these two expressions shows directly how the relation between surface flux and volume pressure measurements extends to the atomic scale. This approach may also prove useful in future for deriving local pressure expressions for systems with different dynamical rules, such as run-and-tumble swimmers [17] or particles with viscous dynamics [4].

4.2 A new derivation of the local pressure

To compute the local pressure at some position $\vec{r}$ in the system, we consider a local region of fluid, of volume Ω, centred on $\vec{r}$. Particles within this region interact with other particles both inside and outside the region. During a given time interval, particles will enter and leave the region of interest.

4.2.1 The Schweitz virial relation

The starting point for the subsequent derivation is an analogue of the Clausius virial relation (4.3), derived by Schweitz, for open systems [140]. The Schweitz virial relation states that

$$\left\langle \sum_{i=1}^{N} \frac{|\vec{p}_i|^2}{m_i} \Lambda_i(\vec{r}) + \sum_{i=1}^{N} \vec{r}_i \cdot \left(\sum_{j \neq i} \vec{f}_{ij} \right) \Lambda_i(\vec{r}) + \sum_{i=1}^{N} \left(\vec{r}_i \cdot \vec{p}_i \right) \dot{\Lambda}_i \right\rangle = 0, \tag{4.7}$$

where, as above, the function $\Lambda_i(t)$ measures whether or not particle i is within the region of interest at time t, and its time derivative $d\Lambda_i(t)/dt \equiv \dot{\Lambda}_i$ produces a positive or negative δ-function peak at the moment when particle i enters or leaves the region of interest. As noted above, the Clausius virial relation, Eq.(4.3), can be derived by setting the time derivative of the function $\langle G \rangle = \left\langle \sum_{i=1}^{N} \vec{r}_i \cdot \vec{p}_i \right\rangle$ to zero in the steady state. For open systems, the derivation of the Schweitz virial relation follows a similar route, but takes into account the contributions to $\langle G_{local}(\vec{r}) \rangle = \left\langle \sum_{i=1}^{N} (\vec{r}_i \cdot \vec{p}_i) \Lambda_i(\vec{r}) \right\rangle$ from particles entering and leaving the system [140].

The first term in Eq.(4.7), $\left\langle \sum_{i=1}^{N} \frac{|\vec{p}_i|^2}{m_i} \Lambda_i(\vec{r}) \right\rangle \equiv E_{kin}$, is the average kinetic energy of particles in the region of interest and is directly analogous to the first term in Eq.(4.3). The second, interaction, term is analogous to the second term in Eq.(4.3) — we assume that there are no external forces so the total force on particle i is given by the sum of interactions with all other particles in the system. The final term in Eq.(4.7), $\left\langle \sum_{i=1}^{N} \left(\vec{r}_i \cdot \vec{p}_i \right) \dot{\Lambda}_i \right\rangle \equiv \Phi$, accounts for the exchange of particles between the region of interest and its surroundings. Particles entering the region contribute $\vec{r}_i \cdot \vec{p}_i$ while those leaving contribute $-\vec{r}_i \cdot \vec{p}_i$; these do not cancel because the momentum vectors $\vec{p}_i$ for particles entering and leaving are opposite in sign.

The second term in Eq.(4.7) can be split into contributions due to interactions with particles inside and outside the region of interest:

$$\sum_{i=1}^{N} \vec{r}_i \cdot \left(\sum_{j \neq i} \vec{f}_{ij} \right) \Lambda_i(\vec{r}) = \mathcal{V}_{int} + \mathcal{V}_{ext}, \tag{4.8}$$

where $\mathcal{V}_{int} \equiv \left\langle \sum_{i=1}^{N} \sum_{j \neq i} \vec{r}_i \cdot \vec{f}_{ij} \ \Lambda_i \Lambda_j \right\rangle = \left\langle \sum_{i=1}^{N-1} \sum_{j>i} \vec{r}_{ij} \cdot \vec{f}_{ij} \ \Lambda_i \Lambda_j \right\rangle \equiv \left\langle \sum_{\text{in in}} \vec{r}_{ij} \cdot \vec{f}_{ij} \right\rangle$[1] contains contributions where both particles are inside the region of interest and $\mathcal{V}_{ext} \equiv \left\langle \sum_{i=1}^{N} \sum_{j \neq i} \vec{r}_i \cdot \vec{f}_{ij} \ \Lambda_i (1 - \Lambda_j) \right\rangle \equiv \left\langle \sum_{\text{in out}} \vec{r}_i \cdot \vec{f}_{ij} \right\rangle$ contains contributions where particle i is inside the region and particle j is outside. Substituting Eq.(4.8) into Eq.(4.7) allows one to write the Schweitz virial relation as

$$E_{kin} + \mathcal{V}_{int} + \mathcal{V}_{ext} + \Phi = 0. \tag{4.9}$$

4.2.2 Components of the local pressure

Equation (4.9) has been written in a form more suited to deriving expressions for the local pressure. As in the MOP technique (Eq.(3.4)), the local pressure expression will have two components: a kinetic component, $P_{kin}(\vec{r})$, which is given by the normal flux of particle momentum across the boundaries of the region of interest, and an interaction component, $P_{int}(\vec{r})$, which is the surface density of inter-particle forces across the boundary. We now relate these components to the terms in Eq.(4.9). Note that throughout this chapter the normal to the boundary is assumed to point in the outward direction.

Kinetic component

The kinetic component of the local pressure can be related to the component $\Phi \equiv \left\langle \sum_{i=1}^{N} (\vec{r}_i \cdot \vec{p}_i) \dot{\Lambda}_i \right\rangle$ of the Schweitz virial relation. To see this, the particle momentum, $\vec{p}_i$, is split into its components normal and tangential to the boundary: $\vec{p}_i = (\vec{p}_i \cdot \hat{n})\hat{n} + (\vec{p}_i \cdot \hat{t})\hat{t}$, to give

$$\Phi = \left\langle \sum_{i=1}^{N} \dot{\Lambda}_i \left[(\vec{p}_i \cdot \hat{n})(\vec{r}_i \cdot \hat{n}) + (\vec{p}_i \cdot \hat{t})(\vec{r}_i \cdot \hat{t}) \right] \right\rangle. \tag{4.10}$$

[1] Here the fact that $\sum_{i=1}^{N} \sum_{j \neq i} \vec{r}_i \cdot \vec{f}_{ij} = \sum_{i=1}^{N-1} \sum_{j>i} \vec{r}_{ij} \cdot \vec{f}_{ij}$ is used, since $\vec{f}_{ij} = -\vec{f}_{ji}$ [4]. A new notation: $\sum_{\text{in in}} g_{ij} = \sum_{i=1}^{N-1} \sum_{j>i} \Lambda_i \Lambda_j g_{ij}$ has also been introduced. Likewise, the notation $\sum_{\text{out out}} g_{ij} = \sum_{i=1}^{N-1} \sum_{j>i} (1-\Lambda_i)(1-\Lambda_j) g_{ij}$ is introduced and $\sum_{\text{in out}} g_{ij} = \sum_{i=1}^{N} \sum_{j \neq i} \Lambda_i (1-\Lambda_j) g_{ij} = \sum_{i=1}^{N-1} \sum_{j>i} [\Lambda_i (1-\Lambda_j) g_{ij} + \Lambda_j (1-\Lambda_i) g_{ji}]$.

Assuming that the density of particles is uniform across the region of interest, the second term in Eq.(4.10) averages to zero. Next, we note that because $\dot{\Lambda}_i$ is nonzero only when a particle is at the boundary, $\vec{r}_i \cdot \hat{n}$ may be taken outside the summation. Assuming (without loss of generality) that the region of interest is cubic with the origin at its centre and sides of length L, $\vec{r}_i \cdot \hat{n} = L/2$ and the total (outward) momentum flux $\left\langle \sum_i (\vec{p}_i \cdot \hat{n}) \dot{\Lambda}_i \right\rangle$ across each of the 6 faces is $-P_{kin} L^2$. Eq.(4.10) therefore reduces to

$$\Phi = -3\Omega P_{kin}(\vec{r}). \tag{4.11}$$

Interaction component

In a similar way, the interaction component of the local pressure, $P_{int}(\vec{r})$, can be related to the component $\mathcal{V}_{ext}$ of the Schweitz virial relation. The position vector $\vec{r}_i$ may be written as $\vec{r}_i = \vec{b}_{ij} + \vec{r}_{ij} l_{ij}$, where $\vec{b}_{ij}$ denotes the position where the line linking particles i and j crosses the boundary of the region of interest and l_{ij} is the fraction of the line linking particles i and j that lies inside the region of interest (see Figure 4.1). $\mathcal{V}_{ext}$ is then given by

$$\begin{aligned} \mathcal{V}_{ext} &= \left\langle \sum_{\text{in out}} \vec{b}_{ij} \cdot \vec{f}_{ij} + l_{ij} \left(\vec{r}_{ij} \cdot \vec{f}_{ij} \right) \right\rangle \\ &= \left\langle \sum_{\text{in out}} (\vec{f}_{ij} \cdot \hat{n}) \left(\vec{b}_{ij} \cdot \hat{n} \right) \right\rangle + C_t + \left\langle \sum_{\text{in out}} l_{ij} \left(\vec{r}_{ij} \cdot \vec{f}_{ij} \right) \right\rangle, \end{aligned} \tag{4.12}$$

where the second line follows from splitting the inter-particle force $\vec{f}_{ij}$ into its components normal and tangential to the boundary: $\vec{f}_{ij} = (\vec{f}_{ij} \cdot \hat{n})\hat{n} + (\vec{f}_{ij} \cdot \hat{t})\hat{t}$, and $C_t = \left\langle \sum_{\text{in out}} (\vec{f}_{ij} \cdot \hat{t}) \left(\vec{b}_{ij} \cdot \hat{t} \right) \right\rangle$. Focusing on the first term, we note that $\vec{b}_{ij}$ points to the boundary and so (assuming the same cubic geometry as above), $\vec{b}_{ij} \cdot \hat{n} = L/2$. Denoting as σ the average outward normal force per unit area crossing the boundary, due to the $(i\,\text{in}, j\,\text{out})$ interactions, the following result is obtained

$$\left\langle \sum_{\text{in out}} (\vec{f}_{ij} \cdot \hat{n}) \left(\vec{b}_{ij} \cdot \hat{n} \right) \right\rangle = -6 \left(\frac{L}{2} \right) (L^2 \sigma) = -3\Omega\sigma. \tag{4.13}$$

The interaction component of the pressure, $P_{int}(\vec{r})$, is equal to the *total* surface density

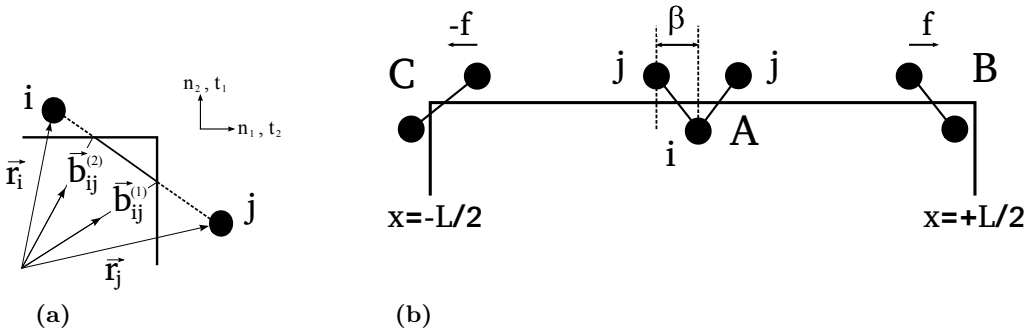

Figure 4.2 (a) Geometric illustration of the case where particles i and j are both outside the region of interest. (b) Illustration of the simplified one dimensional scenario used to show that $C_t = -D_t$.

of normal force crossing the boundary: $P_{int} = \sigma + \xi$, where ξ is the normal contribution due to pairs of particles i and j which are both outside the region of interest (see Figure 4.1).

Let us now consider ξ: the contribution to the interaction component of the pressure made by pairs of particles i and j, in the cases where both particles are outside the region of interest, but (as illustrated in Figure 4.1) the line joining particles i and j crosses the boundary. Starting once again, for simplicity, from the assumption that the region of interest is cubic (with sides of length L and origin at the centre), the line joining particles i and j crosses the boundary on two different faces. These crossing points are denoted by the position vectors $\vec{b}_{ij}^{(1)}$ and $\vec{b}_{ij}^{(2)}$ in Figure 4.2(a), such that $l_{ij}\vec{r}_{ij} = \vec{b}_{ij}^{(2)} - \vec{b}_{ij}^{(1)}$. This allows one to write

$$\left\langle \sum_{\text{out out}} l_{ij} \left(\vec{r}_{ij} \cdot \vec{f}_{ij} \right) \right\rangle = \left\langle \sum_{\text{out out}} \left(\vec{b}_{ij}^{(2)} \cdot \vec{f}_{ij} \right) - \left(\vec{b}_{ij}^{(1)} \cdot \vec{f}_{ij} \right) \right\rangle . \tag{4.14}$$

Resolving $\vec{b}_{ij}^{(1)}$ and $\vec{b}_{ij}^{(2)}$ into components normal and tangential to the boundary on faces 1 and 2 respectively ($\vec{b}_{ij}^{(1)} = (\vec{b}_{ij}^{(1)} \cdot \hat{n}^{(1)})\hat{n}^{(1)} + (\vec{b}_{ij}^{(1)} \cdot \hat{t}^{(1)})\hat{t}^{(1)}$ etc.), and noting that $(\vec{b}_{ij}^{(1)} \cdot \hat{n}^{(1)}) = (\vec{b}_{ij}^{(2)} \cdot \hat{n}^{(2)}) = L/2$, the following result is obtained

$$\left\langle \sum_{\text{out out}} l_{ij} \left(\vec{r}_{ij} \cdot \vec{f}_{ij} \right) \right\rangle = 3\Omega\xi - (D_t^{(1)} + D_t^{(2)}). \tag{4.15}$$

In the above, ξ is the (outward) normal force per unit area crossing the boundary due to particle pairs which are both outside the region of interest, $D_t^{(1)} = \left\langle \sum_{\text{out out}} (\vec{b}_{ij}^{(1)} \cdot \hat{t}^{(1)})(\vec{f}_{ij} \cdot \hat{t}^{(1)}) \right\rangle$ and $D_t^{(2)} = \left\langle \sum_{\text{out out}} (\vec{b}_{ij}^{(2)} \cdot \hat{t}^{(2)})(\vec{f}_{ji} \cdot \hat{t}^{(2)}) \right\rangle$ (note that

$\vec{f}_{ji} = -\vec{f}_{ij}$ has been used). Assuming that particles are homogeneously distributed across the region of interest, $D_t^{(1)} = D_t^{(2)} = D_t/2$ (by symmetry, see Figure 4.2(a)).

We now demonstrate that $D_t = -C_t$, where C_t, as defined above, is the tangential component of the $(i\,\text{in}, j\,\text{out})$ contribution to $\mathcal{V}_{ext}$. This is achieved by studying the simplified one dimensional scenario shown in Figure 4.2(b), in which only particles i and j lying along two lines parallel to the x axis are considered. It is further assumed that interactions are restricted in range, such that each particle i interacts with only two interaction partners j, as shown in Figure 4.2(b), with tangential forces f in opposite directions. These interactions contribute respectively $f(x_i - \beta)$ and $-f(x_i + \beta)$ to the sum $\sum_i \sum_j (\vec{b}_{ij} \cdot \hat{t})(\vec{f}_{ij} \cdot \hat{t})$. The interactions shown in Figure 4.2(b) are added together for the cases where particle i is inside the region of interest ($-L/2 < x_i < L/2$) and the line joining i and j crosses the top face of the region – *i.e.* the contributions to C_t for this face. The result is $f\beta d(\beta - L)$, where d is the number of particles i per unit length along the line[2]. Next, a summation over the contributions for the cases where particle i is *outside* the region of interest, but the line joining i and j still crosses the top face of the region (*i.e.* the contributions to D_t for this face) is made. Contributions $\pm(x \mp \beta)f$ are made by particles i for which $(-L/2 - \beta) < x_i < -L/2$ or $L/2 < x_i < (L/2 + \beta)$ (case C in Figure 4.2(b)). Integrating over these ranges of x_i, a total contribution to D_t of $f\beta d(L - \beta)$ results. Thus the contributions to the $(i\,\text{in}, j\,\text{out})$ tangential term C_t are exactly compensated by the contributions to the $(i\,\text{out}, j\,\text{out})$ tangential term D_t, and Eq.(4.15) reduces to

$$-3\Omega\xi = C_t - \left\langle \sum_{\text{out out}} l_{ij} \left(\vec{r}_{ij} \cdot \vec{f}_{ij} \right) \right\rangle . \tag{4.16}$$

Putting together Eqs.(4.12), (4.13) and (4.16), we can relate P_{int} to $\mathcal{V}_{ext}$ by:

$$-3\Omega P_{int}(\vec{r}) \;\; = \;\; -3\Omega(\sigma + \xi) = \mathcal{V}_{ext} - \mathcal{V}_{corr}, \tag{4.17}$$

where

[2]This result follows from noting that particles i for which $(-L/2 + \beta < x_i < L/2 - \beta)$ have 2 partners and contribute $-2f\beta$ (case A in Figure 4.2(b)), particles for which $-L/2 < x_i < -L/2 + \beta$ have 1 partner and contribute $-(x_i + \beta)f$ while particles for which $L/2 - \beta < x_i < L/2$ have 1 partner and contribute $(x_i - \beta)f$ (case B in Figure 4.2(b)); these contributions are then integrated over $-L/2 < x < L/2$: $df \left[-\int_{-L/2}^{-L/2+\beta} (x + \beta)dx - \int_{-L/2+\beta}^{L/2-\beta} 2\beta dx + \int_{L/2-\beta}^{L/2} (x - \beta)dx \right] = f\beta d(\beta - L)$.

$$\mathcal{V}_{corr} \equiv \left\langle \sum_{\text{in out}} l_{ij} \left(\vec{r}_{ij} \cdot \vec{f}_{ij} \right) + \sum_{\text{out out}} l_{ij} \left(\vec{r}_{ij} \cdot \vec{f}_{ij} \right) \right\rangle . \tag{4.18}$$

4.2.3 Boundary expression for the local pressure

An expression for the local pressure, $P(\vec{r})$, can be obtained by combining Eqs.(4.11) and (4.17):

$$\begin{aligned} P(\vec{r}) &= P_{kin} + P_{int} = -\frac{1}{3\Omega} \left[\Phi + \mathcal{V}_{ext} - \mathcal{V}_{corr} \right] \\ &= -\frac{1}{3\Omega} \left[\left\langle \sum_{i=1}^{N} \left(\vec{r}_i \cdot \vec{p}_i \right) \dot{\Lambda}_i + \sum_{\text{in out}} \left(\vec{r}_i - l_{ij} \vec{r}_{ij} \right) \cdot \vec{f}_{ij} - \sum_{\text{out out}} l_{ij} \vec{r}_{ij} \cdot \vec{f}_{ij} \right\rangle \right] . \end{aligned} \tag{4.19}$$

Equation (4.19) provides a simple prescription for computing the local pressure. The first term sums over all particles which enter or leave the region of interest and is equivalent to the momentum flux density due to particles crossing the boundary, while the remaining terms, which account for the force density at the boundary due to inter-particle interactions, sum over all pairs of particles for which the line connecting the two particles crosses the boundary of the region of interest. In the case where the region of interest is large, $P(\vec{r})$ is dominated by the contributions of Φ and $\mathcal{V}_{ext}$ ($\mathcal{V}_{corr}$ becomes negligible); however, as is shown below in Figure 4.3(b), $\mathcal{V}_{corr}$ makes an important contribution when the region of interest is small. Eq.(4.19) provides an alternative to existing local pressure expressions, and demonstrates explicitly how the relation between surface flux and volume pressure expressions extends to very small regions of space.

4.2.4 Volume expression for the local pressure

The Schweitz virial relation provides a direct route from this "boundary" expression to the more usual expression for the local pressure, Eq.(4.6), which involves a sum over particles *within* the region of interest. Inserting Eq.(4.19) into the Schweitz relation (4.9), we obtain:

$$P(\vec{r}) = \frac{1}{3\Omega}\left[E_{kin} + \mathcal{V}_{int} + \mathcal{V}_{corr}\right] \tag{4.20}$$

$$= \frac{1}{3\Omega}\left\langle \sum_{i=1}^{N} \frac{|\vec{p}_i|^2}{m_i}\Lambda_i(\vec{r}) + \sum_{\text{in in}} \vec{r}_{ij}\cdot\vec{f}_{ij} + \sum_{\text{in out}} l_{ij}\left(\vec{r}_{ij}\cdot\vec{f}_{ij}\right) + \sum_{\text{out out}} l_{ij}\left(\vec{r}_{ij}\cdot\vec{f}_{ij}\right)\right\rangle$$

$$= \frac{1}{3\Omega}\left\langle \sum_{i=1}^{N} \frac{|\vec{p}_i|^2}{m_i}\Lambda_i(\vec{r}) + \sum_{i}\sum_{j>i} l_{ij}\left(\vec{r}_{ij}\cdot\vec{f}_{ij}\right)\right\rangle,$$

where the last line follows from the fact that $l_{ij} = 1$ if both particles are inside the region of interest (assuming the boundary is everywhere concave). Eq.(4.20) is identical to Eq.(4.6), and constitutes a local version of the global instantaneous pressure function, Eq.(4.1).

4.3 Testing the local pressure expressions using simulations

The Schweitz virial relation, Eq.(4.9), as well as the two expressions for the local pressure, Eqs.(4.19) and (4.20), were tested using molecular dynamics simulations in both a homogeneous bath and in an osmotic setup. In the simulations, a periodic box contains 5000 particles at an overall density $\rho = 0.8\ \sigma^{-3}$ (reduced units, see Section 2.1.4), which interact via a WCA potential [165] (described in Section 3.2.1). The particle size $\sigma = 1.0$, the interaction parameter $\epsilon = k_BT = 1.0$ (both in reduced units) and the box length is 18.42 σ. The system is simulated using the velocity Verlet algorithm with timestep $\Delta t = 0.001$ (reduced units) and is maintained in the canonical (NVT) ensemble using a Nosé-Hoover thermostat at temperature, $T = 1.0$ (reduced units). Further details of the simulation setup, particularly the osmotic setup, can be found in Chapters 2 and 3. All of the runs presented here are equilibrated for 40 reduced time units prior to data collection, and data is collected over at least 2000 reduced time units. The bootstrap technique, as outlined in Section 2.2.3, was used to calculate the errors with 1000 replica datasets.

4.3.1 A homogeneous fluid

The local pressure, as measured using expressions 4.19 and 4.20, was first tested in a homogeneous fluid, where comparison with the global pressure (Eq.(4.1)) could be

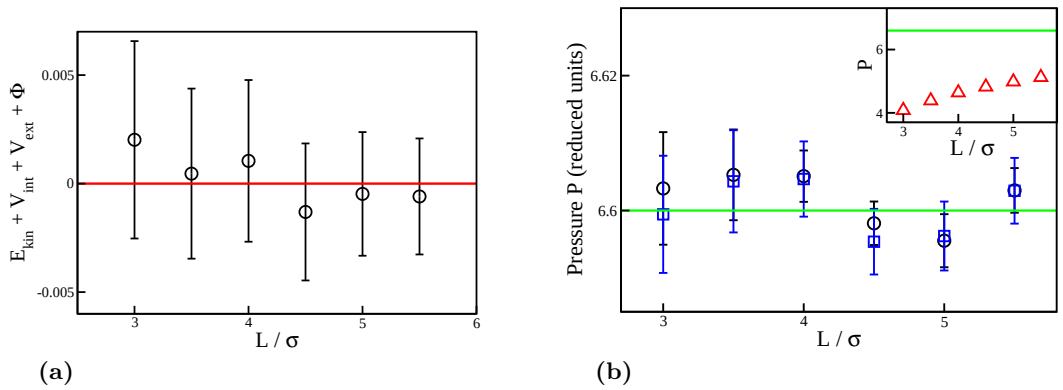

Figure 4.3 Molecular dynamics simulation results for the homogeneous fluid. (a): $E_{kin} + \mathcal{V}_{int} + \mathcal{V}_{ext} + \Phi$ as a function of the size L of the region of interest. (b): Local pressure in the region of interest, computed using Eq.(4.19) (blue squares) and Eq.(4.20) (black circles) as a function of the size L of the region of interest. The apparent correlation between these results arises because the same simulation data set was used in both cases. The green line shows the global pressure computed using Eq.(4.1). The inset shows the pressure computed using Eq.(4.20), not including $\mathcal{V}_{corr}$ (red triangles; note the very different scale on the pressure axis).

made. The Schweitz relation, Eq.(4.9), was also tested using this simple system. A cubic region of interest was defined, located in the centre of the simulation box, whose size L was varied from $L = 5.5\ \sigma$ to $L = 3\ \sigma$. For this smallest value of L, the region of interest contains only ~ 21 particles on average.

Figure 4.3(a) shows $E_{kin} + \mathcal{V}_{int} + \mathcal{V}_{ext} + \Phi$ as a function of the size L of the region of interest. As predicted by the Schweitz relation (4.9), this quantity is zero within the error bars (note that of the individual terms in this sum, two are ~ 5 and the other two are ~ 0.8). Figure 4.3(b) shows the local pressure $P(\vec{r})$ in the region of interest, computed using expressions (4.19) and (4.20), as a function of L. Both expressions give results in excellent agreement with the global pressure across the whole simulation box, computed using Eq.(4.1). The inset to Figure 4.3(b), which shows Eq.(4.20), neglecting the $\mathcal{V}_{corr}$ term, demonstrates the importance of correctly accounting for the boundary terms: neglecting $\mathcal{V}_{corr}$ gives a large error, which increases as L decreases.

4.3.2 An osmotic system

Relations (4.9), (4.19) and (4.20) were also tested using the box in box, invisible membrane osmotic setup, where the local pressure varies within the simulation cell. A brief summary of the osmotic setup used is given here. For full details the reader is referred to Section 3.2.2. A small subset, c_s, of the particles located in the central

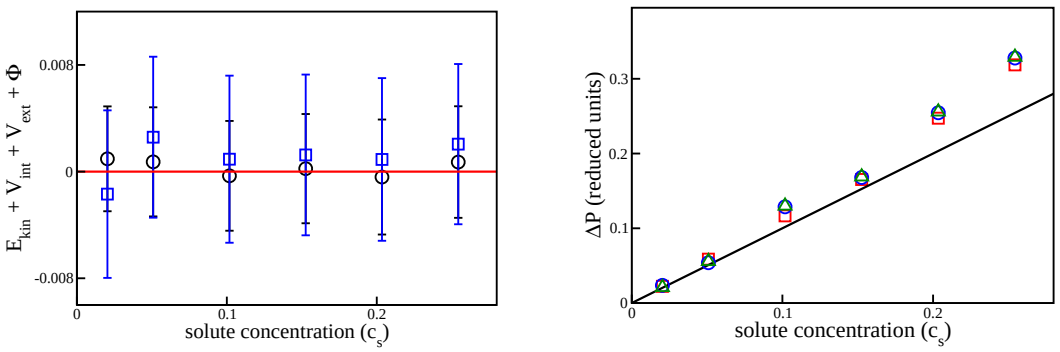

Figure 4.4 Molecular dynamics simulations for the osmotic system. (a): $E_{kin} + \mathcal{V}_{int} + \mathcal{V}_{ext} + \Phi$ as a function of the concentration c_s of solute particles, computed for a small subregion (of dimensions $L_x = L_y = L_z = 6\ \sigma$) within the solution compartment (black circles) and for a small subregion ($L_x = 2\ \sigma$, $L_y = L_z = 7\ \sigma$) outside the solution (blue squares). (b): Osmotic pressure difference ΔP between the solution and its surroundings, computed using Eq.(4.19) (green triangles) and using Eq.(4.20) (blue circles) (for the same subregions). Results are also shown for a direct computation of the normal solute-membrane force per unit area (red squares). Error bars are smaller than the symbols. The prediction of the van't Hoff equation, $\Delta P = k_B T c_s$, is also shown (black line).

region of the simulation are labeled as solute particles and the remaining particles are solvent. The solute particles are confined within a cubic region of volume $V = 786^{+13}_{-32}\ \sigma^3$ in the center of the simulation box by a smooth confining potential; solvent particles do not experience this potential and are free to move throughout the simulation box. The confining potential acts as a semi-permeable membrane, resulting in an osmotic pressure difference, ΔP, between the solution region where the solutes are confined and the rest of the simulation box.

To compute the osmotic pressure, local regions of interest, both inside and outside the solution compartment, are defined (for dimensions see the caption of Figure 4.4). Figure 4.4(a) shows that the Schweitz virial relation (4.9) is obeyed in both of these local regions, over a range of solute concentrations. The pressure in the two local regions is then computed using Eqs.(4.19) and (4.20); subtracting the result in the solution from that in the bath gives the osmotic pressure difference, ΔP. Figure 4.4(b) shows ΔP as a function of the concentration c_s of solute particles in the solution compartment. Both methods for computing the local pressure produce results in excellent agreement with a direct calculation of the osmotic pressure obtained by measuring the average confining force on the solutes, per unit area of the confining box, as discussed in Section 3.2.3.

4.4 Discussion

Accurate methods for computing the local pressure are essential for simulating inhomogeneous soft matter systems. In this chapter two equivalent expressions for the local pressure have been derived and tested in molecular dynamics simulations. The "boundary" expression, Eq.(4.19), involves summation over interactions between particles within and outside the local region of interest and is similar in spirit to the MOP approach of Irving and Kirkwood [66] and of Todd *et al.* [155]. It is believed, however, that Eq.(4.19) is new. The "volume" expression, Eq.(4.20), is a local analogue of the function commonly used to compute the global pressure in homogeneous simulations; this involves summation over interactions between pairs of particles within the region of interest. This expression was previously derived via a Fourier transform method by Lutsko [88] and by Cormier *et al.* [26]; the derivation presented here, based on the Schweitz virial relation, provides a simple real-space alternative. Importantly, both local pressure expressions take careful account of interactions close to the boundary: this is crucial when the region of interest is of the order of the particle size.

This approach may also prove useful in the future for deriving local pressure expressions in systems whose dynamics are more complex: for example systems with viscous dynamics [4], or active matter systems in which particles are self-propelled and/or chemotactic [17]. Here, the Fourier transform derivation of Lutsko and Cormier *et al.* [26, 88] might prove challenging, but it is hoped that the real-space method, presented here, should hold with only minor modifications.

Finally, it is noted that in this chapter the local pressure is assumed isotropic: therefore expressions are derived for the scalar pressure rather than the local pressure tensor, as in previous work [26, 66, 88, 155]. It should be possible to extend the present derivation to obtain the analogous expressions for the pressure tensor, via a tensor analogue of the Schweitz virial relation. For the present, this is left as an interesting avenue for future work.

In the next chapter I will build on the work presented here, using the osmotic setup to conduct a more detailed analysis of the physics of the osmotic steady state, focusing in particular on the nature of the osmotic pressure and the steady-state solvent dynamics at the membrane.

Chapter 5

Osmosis in the Steady State: a Minimal Model

In this chapter the box in box, invisible membrane simulation setup (see Section 3.2.2) is used to analyse in detail the steady-state properties of a minimal model for an osmotic system. As discussed in Chapter 1, osmosis is a well understood phenomenon when considered from a thermodynamic point of view; however, at the molecular level, the nature of the solvent transfer across the membrane remains the subject of some debate. Despite a plethora of proposed mechanisms, there remains no clear consensus in the literature concerning the dynamical mechanisms of solvent flow in osmosis. In realistic systems, factors such as the membrane geometry and the inter-particle interactions will almost certainly influence the solvent dynamics at the membrane. However, osmosis is known to occur in systems comprising hard sphere particles [76] and ones where solvent membrane interactions are absent [67]. The purpose of this chapter is, therefore, to determine the fundamental mechanisms responsible for osmotic density gradients in a minimal system which involves only repulsive inter-particle interactions and in which there are no solvent-membrane interactions.

In a previous simulation work [67], Itano *et al.* studied the relation between the solvent dynamics at the membrane and the solvent-solute interaction in a Lennard-Jones (LJ) system, which includes both repulsive and attractive interactions. In this chapter I will extend on this work by examining the various components of the osmotic pressure in terms of solute-solute and solute-solvent virial contributions to the pressure in both our minimal model, WCA system and, also, a LJ system. In doing so we can separate those effects which arise in systems containing both attractive and repulsive interactions from

those which may in fact be more generic.

A simple hopping model, removed from thermodynamical concepts such as the chemical potential and/or any knowledge of the inter-particle potential, is also proposed as a simple and intuitive explanation for the phenomenon in ideal situations. To ensure that this model suffices in explaining the solvent dynamics in our system, more complex mechanisms, such as solvent entrainment, are tested for by studying the steady-state solvent crossings of the membrane.

To formulate a coherent story, such that theory and simulation are concurrently compared, I first present the simulation setup used throughout this chapter. Results for the steady-state density gradient across the membrane for an equivalent hard sphere system are then derived and compared to the data from simulations. From this we conclude that the system does in fact mimic a system of hard spheres. The resulting osmotic pressure is subsequently studied as a function of the solute concentration in the solution, and a comparison is made to the results from a new derivation for the osmotic pressure, based on the solute particles' virial relation. The virial components of the pressure are then explored in detail, for both the minimal model system and in an equivalent LJ system. Finally, a model for the solvent dynamics at the membrane is presented, based on the hopping of solvent particles at the membrane, from which a further derivation for the osmotic pressure follows. This derivation is based on the density gradients of particles across the membrane and does not involve any complex mechanisms for solvent transport, such as solvent entrainment. To establish that the proposed model suffices as an explanation for the steady-state dynamics of the particles in this study, a more detailed examination of the dynamics of the solvent particles as they cross the membrane is conducted during this period. In particular, correlations between the dynamics of the solute particles at the membrane and the subsequent dynamics of the solvent particles are analysed. From this we are able to test whether or not the solvent entrainment models or micropump models as proposed by Ben-Sasson and Grover [137] (discussed in Section 1.2.2) play a significant role in governing the steady-state solvent dynamics at the membrane for our minimal model system. The results presented in this chapter follow closely those published in [84].

5.1 Simulation details

The simulation setup is described in detail in Chapter 3, Sections 3.2.1 and 3.2.2. Here I briefly restate the key points of the model. A minimal model setup is used,

such that solvent and solute particles interact repulsively with one another in an indistinguishable manner and there are no solvent-membrane interactions. A box in box, invisible membrane setup is implemented by embedding a solution compartment, containing both solvent and solute particles, in a bath containing only solvent particles. A schematic of the setup, as well as a snapshot from a simulation (in which the solution compartment has been isolated), is shown in Figure 5.1.

In our simulations, the solute particles remain confined in the centrally located solution compartment, whereas the solvent particles are free to move between compartments. The confining potential therefore acts like a semi-permeable membrane. Both solvent and solute particles are of unit mass and interact through the repulsive WCA potential, outlined in Section 3.2.1, with parameters $\sigma = 1.0$ and $\epsilon = k_B T = 1.0$. A timestep of $\Delta t = 0.001$ is used in combination with a velocity Verlet algorithm and a Nosé-Hoover thermostat. The system contains 5000 particles in a simulation cell of size $L = 18.42\ \sigma$, so that the overall particle density $\rho_{\text{total}} = 0.8\ \sigma^{-3}$ (the packing fraction $\pi\sigma^3\rho_{\text{total}}/6 = 0.42$).

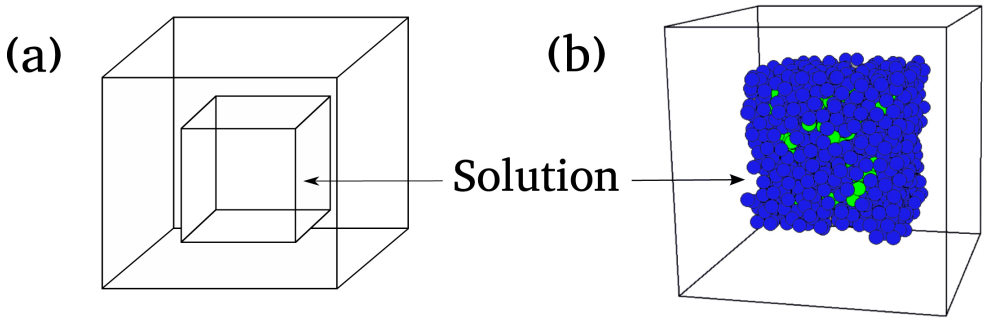

Figure 5.1 (a): Illustration of the model system. Solute particles are confined within a cubic solution compartment located in the centre of the simulation box. (b): Simulation snapshot; solute and solvent particles are coloured green and blue respectively. For clarity only particles located in the solution compartment are shown.

This chapter is concerned with the steady state, thus the simulations are allowed to equilibrate thoroughly for 40 reduced time units before data is collected for a further 2000 reduced time units. We measure the local pressure in the solution and solvent compartments using the method of planes technique [66, 155]. As discussed in Section 3.2.3, this method constitutes a direct measurement of the kinetic and interaction components of the momentum flux across a local plane. The osmotic pressure is then computed by subtracting the local pressure in the solution compartment from that in

the solvent bath. To compute the concentration of solute particles in the solution, we use the definition of the solution volume as described in Section 3.2.2.

5.2 Osmosis in the minimal model system

In this section we explore in detail the nature of the solvent density gradient and the osmotic pressure across the membrane. The results from simulations of particles interacting via the repulsive WCA potential are first compared to a theoretical analysis for the density gradient and osmotic pressure of a hard sphere fluid. A further analysis of the virial components of the pressure is conducted to compare the results between simulations using a WCA (purely repulsive) interaction potential with those in which a LJ (repulsive and attractive) interaction potential is used. This work follows from the preliminary simulations of osmosis conducted in Chapter 4.

5.2.1 Osmotic density gradients from simulations and theoretical considerations

We begin by presenting simulation results for the osmotic density gradient in our model system of WCA particles. Figure 5.2 shows density profiles taken through the middle of our simulation box. As expected, the *total* particle density, solute plus solvent (Figure 5.2(a)), is higher in the solution than in the solvent compartment, demonstrating that osmosis has taken place in our system. In contrast, the *solvent* density is lower in the solution than in the solvent compartment (Figure 5.2(b)). This density imbalance increases linearly with the concentration of solute, c_s, as shown in Figure 5.3. Figure 5.3 also demonstrates that, over the parameter range considered here, the particle density in the solvent compartment remains virtually unaffected by changes in the solute concentration, confirming that the solvent compartment is large enough to be regarded as a reservoir.

If we now approximate the interactions between the particles in the simulations to be hard-sphere-like, it is possible to derive the steady-state density of particles in the solution and solvent bath compartments respectively. In a system comprised of hard sphere particles, liquid state theory [16, 58] tells us that the free energy in the solvent compartment can be expressed as follows:

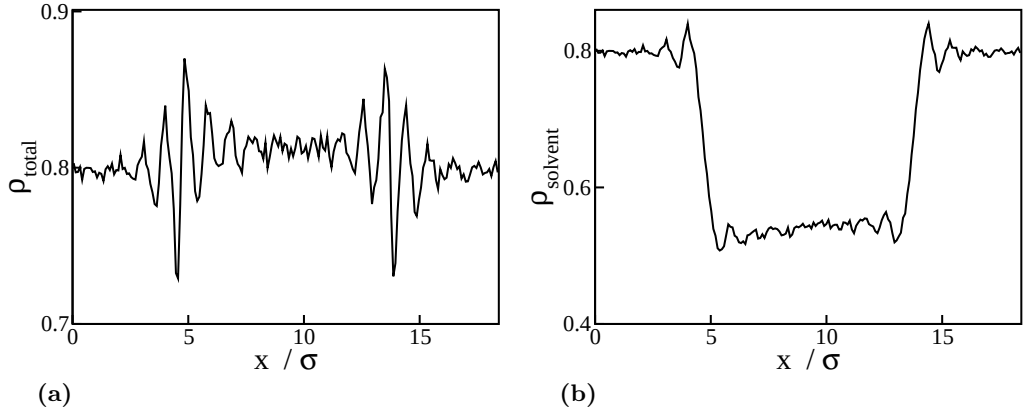

Figure 5.2 Local density profiles $\rho(x)$ (in units of σ^{-3}) measured across the middle of the simulation box, for a solute concentration, $c_{\rm s} = 0.254\ \sigma^{-3}$. Panel (a) shows the total particle density, $\rho_{\rm total}(x)$; panel (b) shows the local solvent density $\rho_{\rm v}(x)$.

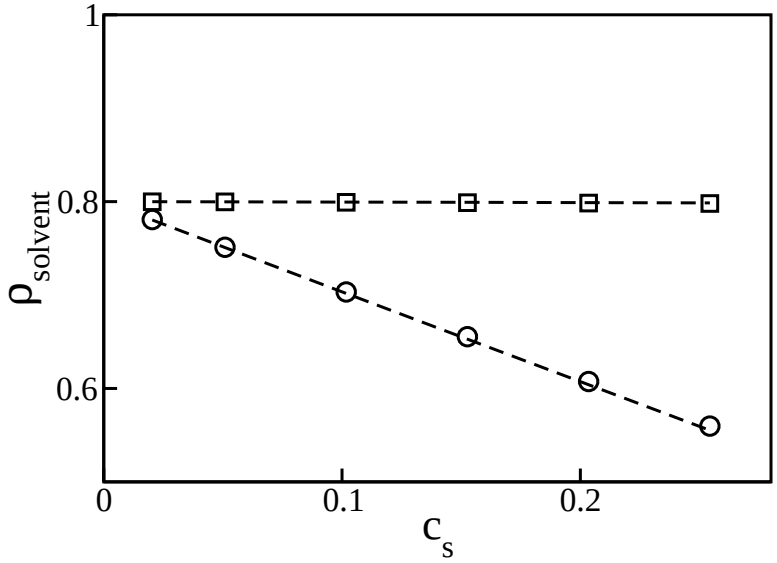

Figure 5.3 Spatially averaged solvent density $\rho_{\rm v}$ as a function of the solute concentration $c_{\rm s}$ (both in units of σ^{-3}), in the solution and solvent compartments (circles and squares respectively). The dashed lines show theoretical predictions, outlined from calculations based on the Carnahan-Starling equation of state (see main text).

$$\begin{aligned} \frac{F^{\rm out}}{k_B T} &= N_{\rm v}^{\rm out}\left[\log\left(\rho_{\rm v}^{\rm out}\Lambda^3\right) - 1 + \eta_{\rm v}^{\rm out}\frac{(4-3\eta_{\rm v}^{\rm out})}{(1-\eta_{\rm v}^{\rm out})^2}\right] \\ &= \frac{6\eta_{\rm v}^{\rm out}V^{\rm out}}{\pi\sigma^3}\left[\log\left(\frac{6\eta_{\rm v}^{\rm out}\Lambda^3}{\pi\sigma^3}\right) - 1 + \eta_{\rm v}^{\rm out}\frac{(4-3\eta_{\rm v}^{\rm out})}{(1-\eta_{\rm v}^{\rm out})^2}\right], \end{aligned} \tag{5.1}$$

where Λ is the de Broglie thermal wavelength and the solvent compartment, of volume $V^{\rm out}$, contains $N_{\rm v}^{\rm out}$ solvent particles, at packing fraction $\eta_{\rm v}^{\rm out}$ (this is related to

the density $\rho_{\rm v}^{\rm out}$ by $\eta_{\rm v}^{\rm out} = \pi\rho_{\rm v}^{\rm out}\sigma^3/6)$. The chemical potential is given by $\mu_{\rm v}^{\rm out} = \partial F^{\rm out}/\partial N_{\rm v}^{\rm out} = (\pi\sigma^3/6V^{\rm out})\partial F^{\rm out}/\partial\eta_{\rm v}^{\rm out}$:

$$\frac{\mu_{\rm v}^{\rm out}}{k_BT} = \log\left(\rho_{\rm v}^{\rm out}\Lambda^3\right) + \eta_{\rm v}^{\rm out}\left[\frac{8-9\eta_{\rm v}^{\rm out}+3(\eta_{\rm v}^{\rm out})^2}{(1-\eta_{\rm v}^{\rm out})^3}\right]. \tag{5.2}$$

The solution compartment on the other hand is of volume $V^{\rm in}$ and contains a mixture of solute particles, at packing fraction $\eta_{\rm s}$, and solvent particles, at packing fraction $\eta_{\rm v}^{\rm in}$. Its free energy is

$$\begin{aligned}\frac{F^{\rm in}}{k_BT} &= N_{\rm s}\left[\log\left(\rho_{\rm s}\Lambda^3\right)-1\right] + N_{\rm v}^{\rm in}\left[\log\left(\rho_{\rm v}^{\rm in}\Lambda^3\right)-1\right] \\ &+ \frac{6V^{\rm in}(\eta_{\rm s}+\eta_{\rm v}^{\rm in})^2}{\pi\sigma^3}\left[\frac{4-3(\eta_{\rm s}+\eta_{\rm v}^{\rm in})}{1-(\eta_{\rm s}+\eta_{\rm v}^{\rm in})^2}\right].\end{aligned} \tag{5.3}$$

The chemical potential, $\mu_{\rm v}^{\rm in} = \partial F^{\rm in}/\partial N_{\rm v}^{\rm in} = (\pi\sigma^3/6V^{\rm in})\partial F^{\rm in}/\partial\eta_{\rm v}^{\rm in}$, can thus be expressed as:

$$\frac{\mu_{\rm v}^{\rm in}}{k_BT} = \log\left(\rho_{\rm v}^{\rm in}\Lambda^3\right) + (\eta_{\rm s}+\eta_{\rm v}^{\rm in})\left[\frac{8-9(\eta_{\rm s}+\eta_{\rm v}^{\rm in})+3(\eta_{\rm s}+\eta_{\rm v}^{\rm in})^2}{(1-(\eta_{\rm s}+\eta_{\rm v}^{\rm in}))^3}\right]. \tag{5.4}$$

As discussed in Chapter 1, the steady state is obtained when the solvent chemical potentials across the membrane are equal. Thus, by setting $\mu_{\rm v}^{\rm in} = \mu_{\rm v}^{\rm out}$, we arrive at the following relation:

$$\begin{aligned}\log\left(\frac{\eta_{\rm v}^{\rm in}}{\eta_{\rm v}^{\rm out}}\right) &+ (\eta_{\rm s}+\eta_{\rm v}^{\rm in})\left[\frac{8-9(\eta_{\rm s}+\eta_{\rm v}^{\rm in})+3(\eta_{\rm s}+\eta_{\rm v}^{\rm in})^2}{(1-(\eta_{\rm s}+\eta_{\rm v}^{\rm in}))^3}\right] \\ &= \eta_{\rm v}^{\rm out}\left[\frac{8-9\eta_{\rm v}^{\rm out}+3(\eta_{\rm v}^{\rm out})^2}{(1-\eta_{\rm v}^{\rm out})^3}\right].\end{aligned} \tag{5.5}$$

Conservation of solvent particle number implies that

$$V^{\rm in}\eta_{\rm v}^{\rm in} + V^{\rm out}\eta_{\rm v}^{\rm out} = \frac{\pi\sigma^3 N_{\rm v}}{6}, \tag{5.6}$$

where $N_{\rm v}$ is the total number of solvent particles. Equations (5.5) and (5.6) may then be solved numerically to obtain $\eta_{\rm v}^{\rm in}$ and $\eta_{\rm v}^{\rm out}$ as functions of the solute packing fraction $\eta_{\rm s}$.

In Figure 5.3 the predictions for a system of hard sphere particles using the procedure outlined above have been included as dashed lines in the figure. Clearly the results from simulation and theory are in excellent agreement, demonstrating that our system of WCA particles can be well-approximated using hard sphere interactions.

5.2.2 The osmotic pressure

The osmotic pressure in our simulations, ΔP (*i.e.* the pressure difference between the solution and solvent compartments), is shown in Figure 5.4 as a function of the solute concentration, $c_{\rm s}$. At low solute concentration, the simulation results (circles) are in good agreement with the van 't Hoff relation (dotted line). At high solute concentration ($c_{\rm s} > 0.1\ \sigma^{-3}$, corresponding to a solute packing fraction greater than 0.05), the osmotic pressure exceeds that predicted by the van 't Hoff relation, as expected in a system with repulsive solute-solute and solute-solvent interactions. Interestingly, however, the osmotic pressure in the system is significantly lower than the pressure that would be obtained for a gas of WCA particles at density $c_{\rm s}$ (dashed line in Figure 5.4; computed using the Carnahan-Starling equation of state). Thus a naïve picture in which one treats the solution simply as a "solute gas", ignoring the solvent (as was done in the solute bombardment models discussed in Chapter 1) does not correctly account for the osmotic pressure. Figure 5.4 also shows the osmotic pressure predicted by a full thermodynamic calculation, for solvent and solute, using the Carnahan-Starling equation of state (dot-dashed line); this prediction agrees well with the results from simulations, as expected for a system of particles with hard-sphere-like interactions.

Standard derivations of the osmotic pressure (including the dot-dashed line in Figure 5.4) rely on thermodynamic principles, *i.e.* on equality of the chemical potential across the membrane. In contrast, my aim in this chapter is to investigate the *mechanical* origins of osmosis. Thus it is of interest to derive expressions for the osmotic pressure from purely mechanical principles, without recourse to thermodynamics. In Chapter 4, I discussed the Clausius virial relation for a system of particles in a closed system. Building on this work, I now derive a virial relation for the osmotic pressure based purely on mechanical principles. In our simulations the solute particles remain confined to the solution compartment and can thus be regarded as being in a closed system.

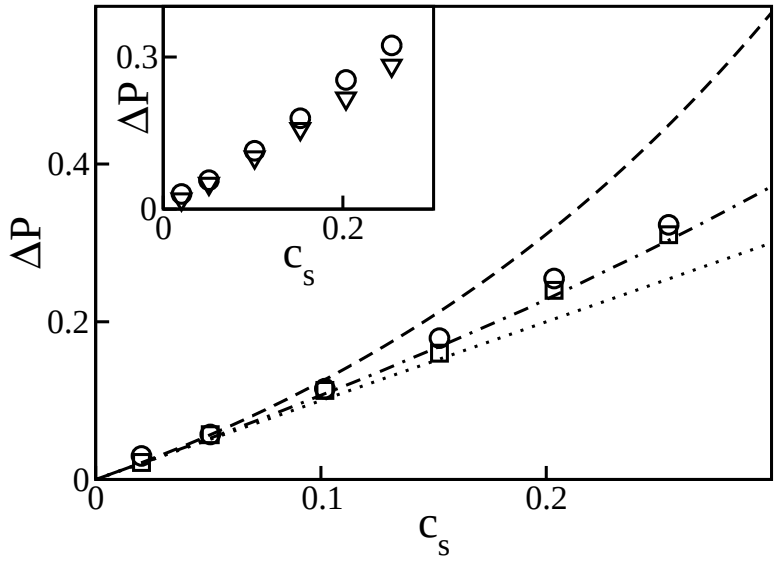

Figure 5.4 Osmotic pressure ΔP (in units of $k_B T \sigma^{-3}$) as a function of solute concentration $c_{\rm s}$ (in units of σ^{-3}). In the main plot, the symbols show simulation results. The circles show direct measurements of ΔP taken from simulations, computed using the method of planes (see Section 3.2.3). The squares show ΔP computed in the simulations using Eq.(5.10). The statistical errors on the symbols are $\pm 3\%$ for c_s (circles and squares) and $\pm 3\%$ for ΔP (squares only) – *i.e.* approximately the size of the symbols. These errors arise mainly from uncertainty in the position of the solution boundary, as discussed in Section 3.2.2. The lines show theoretical predictions. The dotted line shows the van 't Hoff relation, $\Delta P = k_B T c_{\rm s}$. The dashed line shows the pressure of a system of hard spheres at density $c_{\rm s}$, computed using the Carnahan-Starling equation of state. The dot-dashed line shows the osmotic pressure predicted by a full thermodynamic calculation, including solute and solvent, using the Carnahan-Starling equation of state. In the inset, the circles are the same as in the main plot, while the triangles show the prediction of the simple hopping model set out below in Section 5.3.1 (Eq.(5.11): $\Delta P = -k_B T \rho_{\rm v}^{\rm out} \log\left[\rho_{\rm v}^{\rm in}/\rho_{\rm v}^{\rm out}\right]$, where $\rho_{\rm v}^{\rm in}$ and $\rho_{\rm v}^{\rm out}$ are the average solvent densities in the solution and solvent compartments respectively).

Consequently, we can write for the solutes, $d\left\langle \sum_{\rm i_s} \vec{r_i} \cdot \vec{p_i} \right\rangle / dt = 0$ (where the sum is over all solute particles, $\vec{r_i}$ and $\vec{p_i}$ are the position and momentum of particle i, respectively, and the angular brackets denote an ensemble average). Expanding the time derivative and using Newton's equations of motion leads to:

$$\left\langle \sum_{\rm i_s} \frac{|\vec{p_i}|^2}{m_i} \right\rangle + \left\langle \sum_{\rm i_s} \vec{r_i} \cdot \vec{F_i} \right\rangle = 0, \tag{5.7}$$

where, as in Chapter 4, $\vec{F_i}$ is the total force acting on solute particle i, and m_i is its mass. This constitutes a Clausius virial relation for the solutes. Splitting the force $\vec{F_i}$ into the contributions due to interactions with the confining potential, solute-solute

interactions and solute-solvent interactions, and using the equipartition theorem, we arrive at:

$$3N_{\mathrm{s}}k_BT + \sum_{\mathrm{i_s}} \sum_{\mathrm{j_s}>\mathrm{i_s}} \vec{r}_i.\vec{f}_{ij} + \sum_{\mathrm{i_s}} \sum_{\mathrm{j_v}} \vec{r}_i.\vec{f}_{ij} + \sum_{\mathrm{i_s}} \vec{r}_i.\vec{f}_{i,\mathrm{conf}} = 0, \tag{5.8}$$

where $\vec{f}_{ij}$ is the force exerted on particle i by particle j and $\vec{f}_{i,\mathrm{conf}}$ is the confining force on particle i. The first sum is over solute-solute pairs (without double counting), the second sum is over solute-solvent pairs, and the final sum is over interactions between solute particles and the "membrane". Focusing on the final term, we note that, to a good approximation, solute particles only feel the confining force when they are very close to the boundary of the solution compartment. The final term can then be approximated by an integral over a narrow shell at the boundary of the solution compartment. Taking into account also the fact that the osmotic pressure is given by the average normal force per unit area on the membrane, which in our system is equivalent to the magnitude of the confining force on the solute particles per unit area [83], leads to

$$\sum_{\mathrm{i_s}} \vec{r}_i.\vec{f}_{i,\mathrm{conf}} \approx -3V^{\mathrm{in}}\Delta P, \tag{5.9}$$

where ΔP is the osmotic pressure and V^{in} is the volume of the solution compartment. Substituting Eq.(5.9) into Eq.(5.8) leads directly to

$$\Delta P \approx k_BTc_{\mathrm{s}} + \frac{1}{3V}\left(\sum_{\mathrm{i_s}} \sum_{\mathrm{j_s}>\mathrm{i_s}} \vec{r}_i.\vec{f}_{ij} + \sum_{\mathrm{i_s}} \sum_{\mathrm{j_v}} \vec{r}_i.\vec{f}_{ij}\right). \tag{5.10}$$

Since the starting point of this derivation, the Clausius virial relation, follows from Newton's equations of motion in a system at steady state (see Chapter 4), Eq.(5.10) amounts to a purely mechanical description of the osmotic pressure in the system. Figure 5.4 (squares) shows that Eq.(5.10) is indeed in good agreement with the direct measurement of ΔP measured in the simulations (circles), over the full range of solute concentrations tested. To the best of the author's knowledge, Eq.(5.10) is a new result.

Equation (5.10) provides insight into the origins of the deviation of the osmotic pressure from the van 't Hoff relation as the solute concentration increases. This deviation arises from both solute-solute and solute-solvent interactions (the two terms in brackets in

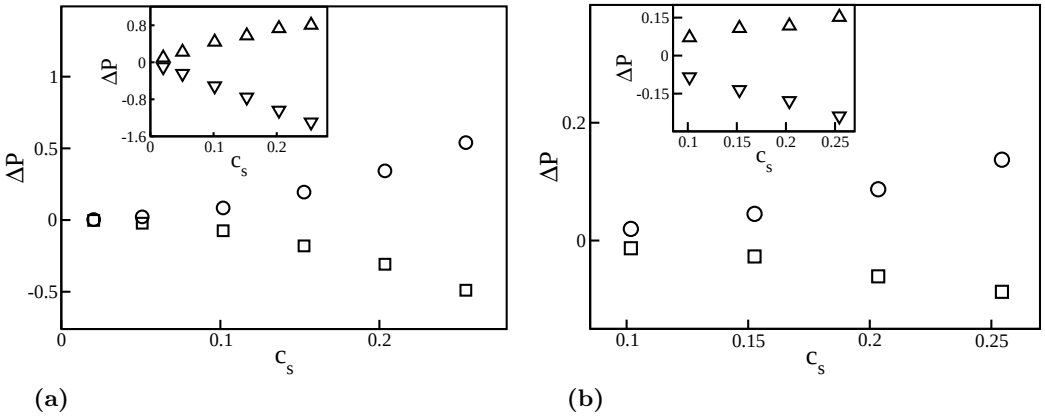

Figure 5.5 Virial contributions accounting for the deviation of the osmotic pressure from the van 't Hoff relation in a system using a WCA interaction potential (panel (a)) and one in which a LJ interaction potential is used (panel (b)). The circles show the solute-solute contribution (the first term in the brackets in Eq.(5.10)) and the squares show the solute-solvent contribution (the second term in the brackets in Eq.(5.10)). The inset splits the solute-solvent contribution into the parts due to interactions with solvent particles inside and outside the solution compartment (upward and downward-pointing triangles respectively).

Eq.(5.10) respectively). These contributions are plotted in Figure 5.5(a) for our system of hard-sphere-like particles: the solute-solute interactions (circles in Figure 5.5(a)) make a positive contribution to the osmotic pressure, as one would expect from a "solute gas" picture, with repulsive solute-solute interactions. However, solute-solvent interactions (squares in Figure 5.5(a)) make a net *negative* contribution, decreasing the osmotic pressure. To understand the origin of this negative contribution, the solute-solvent term is split into contributions due to solvent particles inside and outside the solution compartment. The inset to Figure 5.5(a) shows that solute-solvent interactions *inside* the solution compartment increase the osmotic pressure (upward triangles in the inset), while interactions between solute particles and solvent particles which are *outside* the solution compartment (*i.e.* cross-membrane interactions; downward triangles in the inset) decrease the osmotic pressure. Thus, in the simulations, the solute particles are pushed outwards by interactions with other solutes and with solvent particles in the solution, but at the same time they are pushed inwards by interactions with solvent particles located outside the solution compartment.

To establish whether this behaviour is unique to hard-sphere-like systems, the virial components of Eq.(5.10) have also been studied in an equivalent Lennard-Jones (LJ) system (the LJ potential is shown in Figure 3.4 in Chapter 3), which contains both attractive and repulsive interactions, over several solute concentrations; see Figure 5.5(b). The behaviour of each of the virial components as a function of the solute

Table 5.1 The ratio of the osmotic pressures in the WCA and LJ systems (as calculated using the MOP technique) are shown for several solute concentrations.

c_s (σ^{-3})	Osmotic pressure ratio
0.10	0.96
0.15	0.93
0.20	0.99
0.25	0.99

concentration, shown in Figures 5.5(a) and (b), appears almost identical across the two systems studied. This suggests that the behaviour of the virial components of the osmotic pressure in the LJ system, as a function of increasing solute concentration, are dictated by the repulsive component of the interaction potential. Indeed the qualitative form of the virial relations may be common to many systems whose interactions contain both an attractive and a repulsive component. This may also be true for the osmotic pressure. In Table 5.1, the ratio of the osmotic pressure in the LJ and the WCA systems is almost equal to one for each of the solute concentrations presented.

Expression (5.10) makes an interesting connection with "effective single-component" descriptions of osmotic systems, as used, for example, for colloidal dispersions. Here, one aims to coarse-grain the system of solute and solvent particles, representing it by a single-component fluid of solute particles which interact via an effective potential that takes into account the effects of the solvent. This works well for colloidal dispersions where the colloids (solutes) are orders of magnitude larger than the solvent molecules and the effective interactions are well-represented by a pairwise inter-colloidal potential $V(r)$. Here, by analogy with atomic systems, the osmotic pressure, Π, is written as $\Pi = nk_BT - \frac{2\pi}{3}n^2 \int_0^\infty r^3 g(r)\,(dV/dr)\,dr$ (see Section 1.1), where n is the number density of colloidal particles and $g(r)$ is the radial pair distribution function [11, 58, 136]. This expression can also be derived from a purely dynamical description of colloidal motion (see Section 1.3), taking account of Brownian motion and hydrodynamic interactions [11]. Equation (5.10) provides an analogous expression for the osmotic pressure, for a system in which the solvent degrees of freedom are treated explicitly and on the same footing as those of the solute.

5.3 Maintaining the solvent density gradient

Having established that our minimal model reproduces osmosis and with a better understanding of the contributions that the various solute-solute and solute-solvent interactions make to the osmotic pressure, we now study the dynamical mechanisms

which maintain the steady-state density gradient of particles across the membrane in osmosis.

5.3.1 Balance between outward and inward fluxes

Using molecular dynamics simulations allows us to explore in detail the balance of solvent forces at the membrane which produce the imbalance in the density of solvent particles between the solution and solvent compartments. Figure 5.6 shows the net force per particle, acting on the solvent particles, as a function of position x, in a slab through the middle of the simulation box. Solvent particles close to the boundaries of the solution compartment are on average pushed out of the solution, towards the solvent compartment. This net force arises from the fact that the total density inside the solution compartment is higher than that in the solvent compartment (as shown in Figure 5.2(a)) – thus, we expect solvent particles at the boundary to experience more collisions from the solution side than from the solvent side.

Why then is there no net flow of solvent out of the solution compartment in response to the net outward force? The answer lies in the solvent density profiles. As shown in Figure 5.2(b), the density of *solvent* particles is higher in the solvent compartment than in the solution. This should create a diffusive flux of solvent particles into

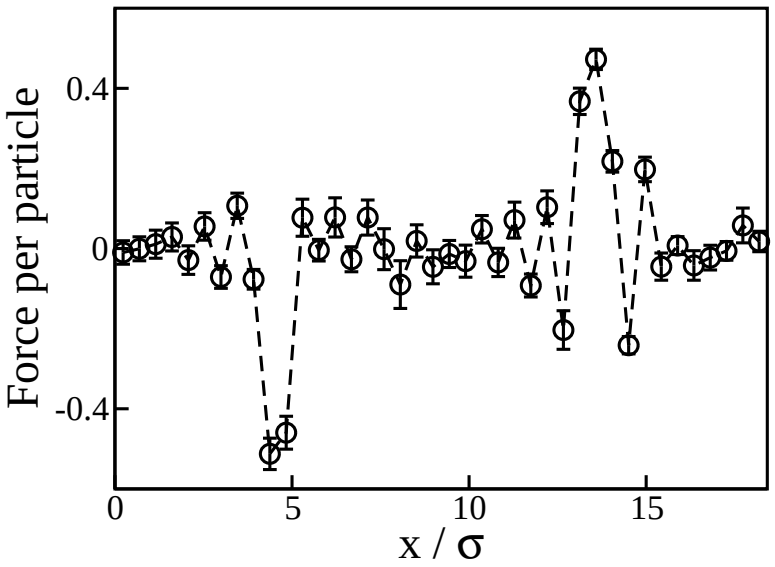

Figure 5.6 Net force per particle, normal to the membrane (in units of $k_BT\sigma^{-1}$), acting on the solvent particles, as a function of position x, in a slab taken through the middle of the simulation box, for solute concentration, $c_s = 0.254\ \sigma^{-3}$. Solvent particles close to the boundaries of the solution compartment tend to be pushed out of the solution.

the solution, which counteracts the outward flux caused by the net outward force. Considering, rather simplistically, the "hopping" of solvent particles between layers next to the membrane on the solvent and solution sides (see Figure 5.7), we expect that, due to the outward pushing force, an individual particle on the solution side has a high probability of leaving the solution (*i.e.* to hop from the solution to the solvent compartment). Meanwhile, an individual particle on the solvent side has only a low probability of entering the solution (*i.e.* to hop from the solvent to the solution compartment). However, there are more solvent particles on the solvent side and consequently more attempts to hop into the solution than out of it. Thus the net fluxes of solvent particles inward and outward are equal and the solvent density imbalance is maintained. This picture has much in common with the classic colloidal sedimentation equilibrium, in which an inhomogeneous colloidal density profile is maintained by the balance of a downward flux driven by the gravitational field and an upward diffusive flux. This analogy between osmosis and sedimentation was also noted by Soodak and Iberall [146].

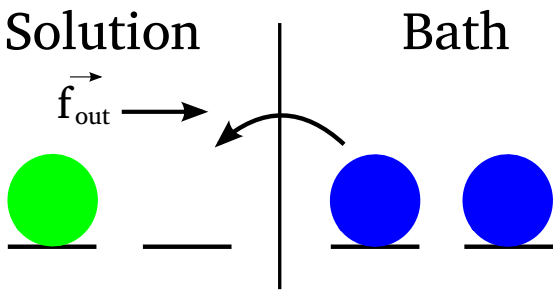

Figure 5.7 Hopping model illustrating that particles which hop from the bath into the solution compartment must overcome an energy penalty, $\vec{f}_{\rm out}$. The solvent particles on the solution side, meanwhile, are assisted by this outward force, increasing the hopping rate from the solution to the bath. Further details of this model are outlined in the main text.

Using this simple "hopping" picture, it is possible to relate the solvent density imbalance to the osmotic pressure by simple mechanical arguments. Let us assume the solvent densities, $\rho_{\rm v}^{\rm in}$ and $\rho_{\rm v}^{\rm out}$ in the solution and solvent compartments respectively, are uniform, with a very sharp density change at the boundary. We now define slabs of width h (of the order of the molecular size) next to the boundary on the solvent and solution sides, and consider the hopping of solvent particles between these slabs. Solvent particles that hop from the solvent side into the solution experience an energy penalty $h\vec{f}_{\rm out}$, where the outward force $\vec{f}_{\rm out}$ arises from the fact that the total density is higher in the solution, and can be related to the osmotic pressure ΔP by $\Delta P = \vec{f}_{\rm out}/a$, where a is the slab area per particle. Setting the fluxes of solvent particle hops equal in the inward and outward directions, we find that

$\rho_{\rm v}^{\rm in} = \rho_{\rm v}^{\rm out} \exp\left[-\vec{f}_{\rm out} h/(k_B T)\right] = \rho_{\rm v}^{\rm out} \exp\left[-ah\Delta P/(k_B T)\right]$. Noting now that ah is the volume per particle, which is approximately the same on both sides of the membrane — *i.e.* that $ah \approx 1/\rho_{\rm total}^{\rm in} \approx 1/\rho_{\rm v}^{\rm out}$, leads to the result

$$\Delta P \approx -k_B T \rho_{\rm v}^{\rm out} \log\left[\frac{\rho_{\rm v}^{\rm in}}{\rho_{\rm v}^{\rm out}}\right]. \tag{5.11}$$

Equation (5.11) is in fact a standard relation, which can be derived via thermodynamic arguments [42, 145], by setting the solvent chemical potential equal across the membrane and making the assumption that $\rho_{\rm total}^{\rm in} \approx \rho_{\rm v}^{\rm out}$. Thus the simple hopping model developed here provides a clear mechanistic description which leads to the same predictions as the thermodynamic/statistical mechanical pictures. The mechanistic description of course relies on the presence of repulsive inter-particle interactions, which generate the "outward pushing force".

Figure 5.4 (inset; triangles) shows that Eq.(5.11) holds in our simulations, even for solute concentrations well beyond the limit of validity of the van 't Hoff relation. The slight discrepancy between the prediction of Eq.(5.11) and the simulation results arises from the assumption $\rho_v^{out} \approx \rho_{total}^{in}$ made in our derivation.

For low solute concentrations, Eq.(5.11) reduces to the van 't Hoff relation. Noting that $\rho_{\rm v}^{\rm in} = \rho_{\rm total}^{\rm in} - c_{\rm s} \approx \rho_{\rm v}^{\rm out} - c_{\rm s}$ leads to:

$$\log\left[1 - \frac{c_{\rm s}}{\rho_{\rm v}^{\rm out}}\right] \approx -\frac{\Delta P}{k_B T \rho_{\rm v}^{\rm out}}. \tag{5.12}$$

The van 't Hoff relation is then recovered when we expand the logarithm to first order in $c_{\rm s}/\rho_{\rm v}^{\rm out}$ (which is small for low solute concentration):

$$\Delta P \approx -k_B T \rho_{\rm v}^{\rm out} \log\left[1 - \frac{c_{\rm s}}{\rho_{\rm v}^{\rm out}}\right] \approx k_B T c_{\rm s}. \tag{5.13}$$

5.3.2 Solvent-solute correlations

The simple picture presented above provides a mechanical description which is consistent with results obtained from thermodynamic arguments, and which is also consistent with the force profiles measured in our simulations. To show that this actually describes what is happening in the simulations, more complex dynamical

mechanisms must be ruled out. A key feature of the simple picture outlined above is that it does not predict any correlations between the configuration of the solute particles and the hops of solvent particles across the membrane – unlike some other proposed mechanisms, for example the solvent entrainment models discussed in Section 1.2.2, in which solvent particles are pulled across the membrane in the wake of nearby solute particles. To look for such effects in the simulations, we must therefore test whether correlations between solute and solvent motion influence the dynamics of solvent particles close to the membrane.

We first ask whether the microscopic flux of solvent particles into the solution compartment is influenced by the presence of nearby solute particles. At time t, we focus on solvent particles which are situated less than 0.001 particle diameters[1] outside the solution compartment. Within the next timestep, some of these solvent particles cross into the solution compartment, while others do not. Figure 5.8(a) shows the distribution of distances to the nearest solute particle, for those solvent particles which do cross in the next timestep (black line) and for those which do not (red line). These distributions are indistinguishable, suggesting that proximity of a solute particle does not make any difference to the chance that a solvent particle, located close to the boundary, will cross into the solution compartment.

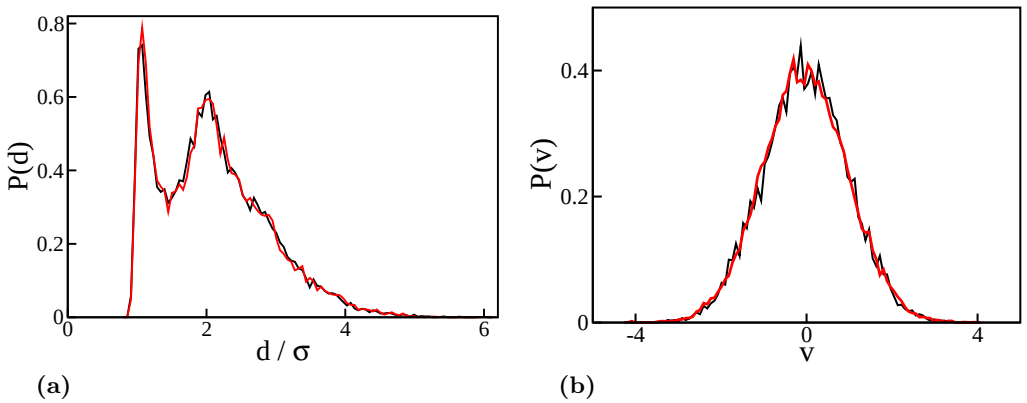

Figure 5.8 Probability distributions for the distance d to the nearest solute particle (a) and the perpendicular velocity v of the nearest solute particle (b), for solvent particles located less than 0.001 particle diameters outside the solution compartment, which do (black lines) or do not (red lines) enter the solution compartment in the next simulation timestep. In these simulations, $c_s = 0.05\ \sigma^{-3}$. The boundary of the solution compartment is defined as described in Section 3.2.2.

One might also suppose that the *velocity* of nearby solute molecules might influence the microscopic flux of solvent particles, *e.g.* a solvent particle could cross into the

[1] This corresponds to a similar distance to that which a particle at temperature $T = 1$ will move in one timestep.

solution in the wake of a nearby solute particle as it rebounds from the membrane. Figure 5.8(b) shows the probability distribution for the velocity of the nearest solute particle (perpendicular to the solution boundary), for solvent particles located close to the solution boundary, which do and do not subsequently cross into the solution. Once again, the two probability distributions are indistinguishable.

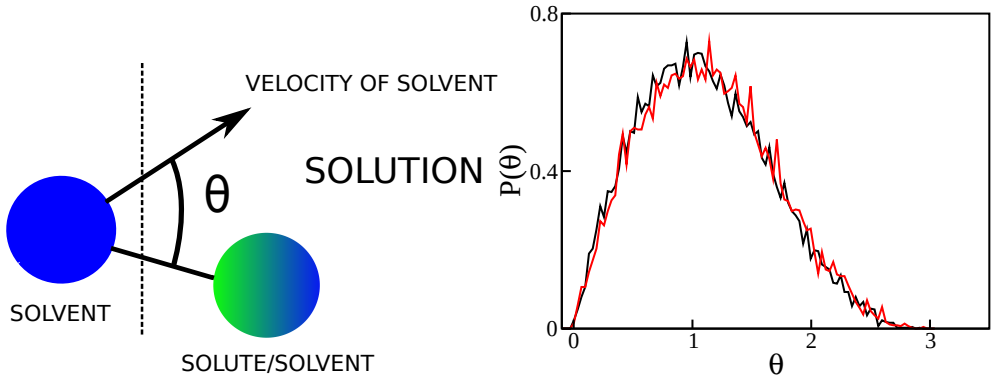

Figure 5.9 (a): A diagram illustrating the angle θ between the instantaneous velocity of a solvent particle i as it enters the solution compartment and the vector joining it to particle j within the solution compartment is shown. (b): The corresponding probability distribution $P(\theta)$ for this quantity is plotted when particle j is defined to be the nearest solute particle (black line) and when particle j is the nearest particle of either solute or solvent (red line). In these simulations, $c_s = 0.05\ \sigma^{-3}$. The boundary of the solution compartment is defined as described in Section 3.2.2.

As a final test, it was ascertained whether solvent crossings occur preferentially in the *direction* of the nearest solute particle. If solute particles tend to "suck" solvent particles across the membrane, solvent crossings should be preferentially oriented towards the nearest solute particle. To determine whether this effect is present in our hard-sphere-like system, the angle θ between the instantaneous velocity $\vec{v}_i$ of a solvent particle, as it crossed into the solution compartment, and the vector $\vec{r}_{ji} = \vec{r}_j - \vec{r}_i$, where $\vec{r}_i$ and $\vec{r}_j$ are the position of the solvent particle and the nearest solute, respectively (see Figure 5.9(a)) was measured. Figure 5.9(b) (black line) shows the probability distribution $P(\theta)$. The calculation was then repeated, but this time allowing particle j to be either solute or solvent (within the solution compartment). The resulting distribution is given by the red line in Figure 5.9(b). Again, the two distributions are indistinguishable, showing that solvent particles do not cross the membrane preferentially in the direction of nearby solute particles. It may therefore be concluded that correlations between solute and solvent dynamics do not play a significant role in determining the microscopic solvent flux in these simulations. This suggests that the simple dynamical picture described above is indeed sufficient to describe osmosis in our simple system.

5.4 Discussion

In this chapter, a minimal model has been used to investigate the dynamical mechanisms underlying the maintenance of equilibrium osmotic pressure and density gradients in a system where solute and solvent particles interact identically, and in which there are no solvent-membrane interactions. For this system, a new expression (Eq.(5.10)) for the osmotic pressure has been derived, in terms of the forces of interaction between solute-solute and solute-solvent pairs of particles. This derivation does not assume any separation of scales between the solvent and solute particles[2]. The components of this virial relation for the pressure were first analysed for the minimal model system, as a function of the solute concentration, and then compared to an equivalent LJ system. Based on the qualitative agreement between the two systems it was concluded that, for the LJ system, the qualitative variation in the virial components with increasing solute concentration is dictated by the repulsive component of the interaction potential. It was further demonstrated that the resulting osmotic pressures for the two systems are in excellent quantitative agreement.

Analysis of the density and force profiles in the simulations led to the development of a very simple picture, in which the density imbalance of solvent particles across the membrane is maintained by a balance between an outward force-driven flux (due to the higher total density in the solution) and an inward diffusive flux (due to the lower solvent density in the solution). It was shown that a simple calculation, based on the mechanics of hopping of solvent molecules across the membrane, can be used to derive the same relation between the solvent density gradient and the osmotic pressure (Eq.(5.11)) as is obtained by standard thermodynamic arguments. For low solute concentrations, this expression reduces to the van 't Hoff relation. No evidence was found for correlations between the solute particles trajectories and the solvent flux, supporting the notion that this simple "hopping" picture is sufficient to describe the dynamical basis of osmosis in the simulations presented. Interestingly, if we consider a hypothetical ideal gas scenario where the solute and solvent do not interact, the hopping model is no longer valid. However, in such a system there would also be no osmotic density imbalance – the solvent density would be equal on both sides of the membrane, thus confirming that hard-sphere-like interactions constitute a minimal model for osmosis.

In previous work (see Section 1.2.2 and [14, 29, 56, 137]), various molecular mechanisms

[2]Of course, one is always free to coarse-grain the solvent particles, treating the solutes as a "gas" with effective interactions which account for the presence of the solvent. But for systems like that treated here, without solvent-solute scale separation, these effective interactions may be many-body.

have been implicated in osmosis, including solute-solvent interactions and correlations between solvent and solute dynamics. In simulations of realistic osmotic systems using porous membranes (as discussed in Section 3.1), the dynamics of the solvent molecules inside the pores [5, 70], interactions with the pore wall [131], interactions between solvent and solute molecules [15, 131], and correlations between solvent flux and the solute dynamics [21] have all been shown to play important roles. It is possible that different dynamical mechanisms are at play in different osmotic systems, all of these being consistent with the known, and universal, thermodynamic relations. Thus, an important topic for further work is to better understand how the conclusions drawn in this work change for more realistic scenarios: *e.g.* when the membrane presents a barrier also to the solvent molecules (via explicit pores or, as will be studied in Chapter 6, via a smooth potential barrier), or when the solute and solvent do not interact identically. My aim in this chapter, however, was to focus on a minimal model system, for which the underlying molecular mechanisms of osmosis could be characterised in detail. For this system, we find that complex mechanisms are not required to understand the basic physics of osmosis.

Chapter 6

The Relaxation to the Steady State

A basic understanding of the mechanism for solvent transport in osmosis during the system's relaxation to the steady state might help us design more efficient osmotic power plants, improve the efficiency of water desalination and better understand the fundamentals of osmosis in biology. However, despite the need for such an understanding, this mechanism remains the subject of some debate.

In an early paper Fick outlined an argument that supported the notion that osmosis is a diffusive flow [41]. Under this assumption, the solvent flow proceeds by the random motion of particles down a chemical potential gradient on an individual particle basis, *i.e.* it is not reliant on the bulk, collective movement of solvent particles. As discussed in Section 1.2.1, this remains, to this day, an oft-cited explanation of the solvent flow across the membrane. It has been known for some decades now, however, that the solvent transfer prior to the steady state across porous membranes proceeds at a rate faster than would be predicted by a solely diffusive mechanism [92]. In fact, osmosis has been shown to proceed, using porous membranes, at an equivalent rate to pressure-driven flows and, as a result, the same membrane filtration coefficient L_p, a constant that relates the pressure gradient to the resulting flux of particles, is used to describe both types of flow (see Section 1.2.1). However, for typical experiments with porous membranes, it is difficult to isolate the effects that processes such as unstirred layers may have on the solvent dynamics [28, 42]. Furthermore, it has been recently discovered that the solvent in molecularly narrow pores can form a single file chain that "slips" through the pore [70]. It therefore seems logical that, in order to gain a clearer understanding

of the solvent dynamics in osmosis in the period prior to the steady state, we should use a bottom up approach, studying the dynamics in a system which uses a simple, minimal model for the membrane barrier. In this chapter we therefore study the solvent transport prior to the steady state in as simple a system as possible: using a double box, finite membrane setup.

In contrast to our previous work, the solvent particles in this chapter do interact with the membrane barrier. Solute particles experience, as before, a steep repulsive potential which confines them to the solution, whereas the solvent particles must cross a finite free energy barrier in order to move between the solution and bath compartments. This is important because the finite barrier slows down the dynamics of the solvent, extending the transient, relaxation period prior to the steady state. This allows us to study in detail the nature of the solvent flow during this period.

The layout of this chapter is as follows. A short review of the simulation setup is first given before a preliminary investigation of the solvent density profiles during the steady state is conducted. We begin our study of the relaxation dynamics of the solvent particles in osmosis by comparing the results of simulation to the prediction of the simplest possible hypothesis, that the process relaxes exponentially to the steady state. However, it is discovered that the simulation results display a more interesting behaviour, with a transition between an early, more rapid rate of solvent transfer to a later, slower rate of solvent transfer across the membrane. The solvent dynamics using an osmotic setup are found to be in agreement with those of an equivalent pressure-driven flow, a result we reconcile by studying the pressure profile across the membrane barrier. To gain better statistics, we then formulate a simple tracer experiment, where we track the flow of solvent particles across the barrier by labeling all of the particles on one side of the membrane at $t = 0$ and subsequently recording their flux into the other compartment. We successfully model the late time dynamics of the tracer particles using Kramers' theory, a diffusive model which describes the rate that individual particles cross a free energy barrier due to Brownian motion. By recording the tracer flux in both directions across the barrier we are able to recover a relation which allows us to apply Kramers' theory to the study of osmotic flows across the membrane. The results of simulation and theory for the net rate of solvent transfer demonstrate some agreement at early times. However, at later times, based on Kramers' theory, we would conclude that the solvent transfer takes place at a rate which is slower than diffusion. The consequences of this result are discussed and a qualitative model for the solvent transfer across the membrane in our simple setup is outlined.

6.1 Simulation details

Since the simulation setup used in this chapter is described in detail in Chapter 3, here only a brief review is given. The solution compartment and the solvent bath are identical, except that the solution compartment contains both solvent and solute particles whereas the solvent bath contains only solvent particles. A schematic of the setup and a snapshot from a simulation are shown in Figure 6.1, in which the solution compartment is on the left hand side (LHS) of the central membrane barrier and the solvent bath is on the right hand side (RHS).

Similar to the box in box, invisible membrane setup, the solute particles are confined to the solution compartment using a steep potential; although here, the confining potential acts only in the $x - direction$ at $x = 0 = L_x$ and $x = 0.5L_x$. The solvent particles, meanwhile, experience a smooth barrier potential at these locations which they must overcome in order to cross the membrane. As previously stated, the presence of a finite barrier slows down the solvent particles' transport across the membrane, extending the transient period prior to the steady state. Periodic boundary conditions, as described in Section 2.1.4, are implemented in the x, y and z directions. The solute and solvent particles interact identically through the WCA potential, outlined in Section 3.2.1, with the typical simulation parameters, $\sigma = 1.0$ and $\epsilon = k_BT = 1.0$. A timestep of $\Delta t = 0.001$ is used in combination with the velocity Verlet algorithm and a Nosé-Hoover Langevin thermostat. A total of 5000 particles are simulated, such that the overall particle density in the simulations is $\rho = 0.8\ \sigma^{-3}$ (the packing fraction $\pi\sigma^3\rho/6 = 0.42$) as in previous chapters.

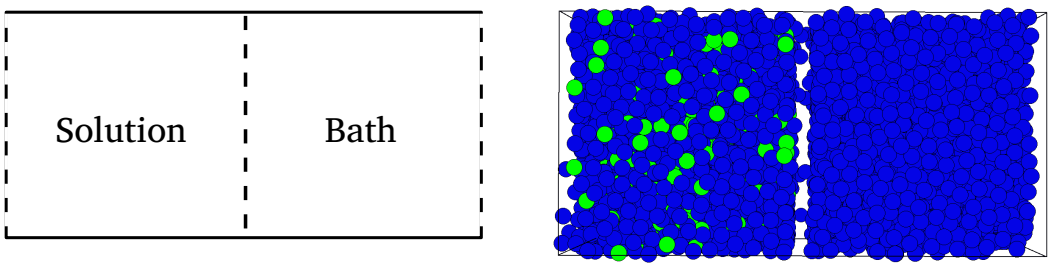

(a) **(b)**

Figure 6.1 (a): Diagram illustrating the setup used. The solution compartment is placed on the LHS of the simulation box and the solvent bath on the RHS. The dashed lines indicate the positions of the membrane and periodic boundary conditions are imposed in the x, y and z directions. (b): A snapshot is shown from the simulations in the transient period before the steady state. A barrier of height $H = 15\ k_BT$ is used in combination with a solute concentration, $c_s = 0.1\ \sigma^{-3}$.

To ensure that the respective compartments are well mixed, the solvent particles experience the same confining potential as the solute particles for 1800 reduced time units — *i.e.* the system is equilibrated with the confining potential for both the solute and solvent particles — before the potential is truncated, such that it now presents a barrier of height H to the solvent particles. Once the barrier has been truncated, the dynamics of the solvent particles are tracked for at least a further 400 reduced time units as the system relaxes to the steady state. Results from this period presented later on in the chapter correspond to average trajectories having conducted a large number (≥ 150) of simulations.

In this chapter we study the flow of solvent in osmosis and, also, the flow of solvent driven by pressure gradients across the membrane, so-called pressure-driven flows. Using an osmotic setup, the presence of impermeant solute particles on the LHS of the membrane ensures a gradient in the solvent chemical potential across the membrane (see Section 5.2.1); however, in these simulations, there is no initial imbalance in the total number of particles on either side of the membrane. In the pressure-driven flows, however, we establish an equivalent chemical potential gradient across the membrane (in the absence of solutes) by placing more particles on the LHS of the membrane than on the RHS. To choose osmotic and pressure-driven systems with equivalent chemical potential gradients we use the statistical mechanical expression for the chemical potential, $\mu/k_BT = \log\left[\rho\Lambda^3\right] + \mu^{ex}(\rho)$, where ρ is the density and μ^{ex} is the excess part of the chemical potential, see Section 5.2.1 or [58] for further details.

6.2 Preliminary investigation: solvent density profiles in the steady state

In previous chapters the membrane was invisible to the solvent particles, whereas in this chapter a finite barrier is used. It is, therefore, of some interest to study the solvent density profiles in the barrier region during the steady state as a function of the barrier height. In Figure 6.2(a) the density profiles for the solvent particles are shown for several barrier heights, $H = 13,\ 15$ and $17\ k_BT$, by the black, red and blue lines, respectively. For the 15 and 17 k_BT barriers the solvent particles are almost entirely excluded from the central membrane region, whereas for the 13 k_BT barrier we observe some solvent occupation of this region. Although it is to be expected that lowering the barrier will result in a gradual "filling" of the membrane barrier, it is of interest that the density profile becomes peaked towards the centre of the barrier region.

This behaviour is explained in Figure 6.2(b), where the steady-state average force (black line) and potential (red line) profiles which a solvent particle experiences due to a 5 k_BT barrier are compared to the total (*i.e.* including the other particles) average force (blue line) that a solvent particle experiences using the same barrier. In our simulations there is an interplay between an inward pushing force, which moves the particles to the centre of the barrier, resulting from the high density of particles on either side of the membrane, and an outward pushing force (pushing the solvent back into the bulk), owing to the repulsive nature of the membrane barrier. For the 5 k_BT barrier we observe peaks in the total force slightly to the left and right of the centre of the barrier. These suggest that the 5 k_BT barrier is low enough that the particles at these positions experience a larger inward than outward pushing force. Therefore, a peak in the density profile observed in Figure 6.2(a) develops. Later on we discuss the effects that decreasing the barrier height, and consequently allowing solvent to accumulate within the membrane, has on the solvent dynamics prior to the steady state.

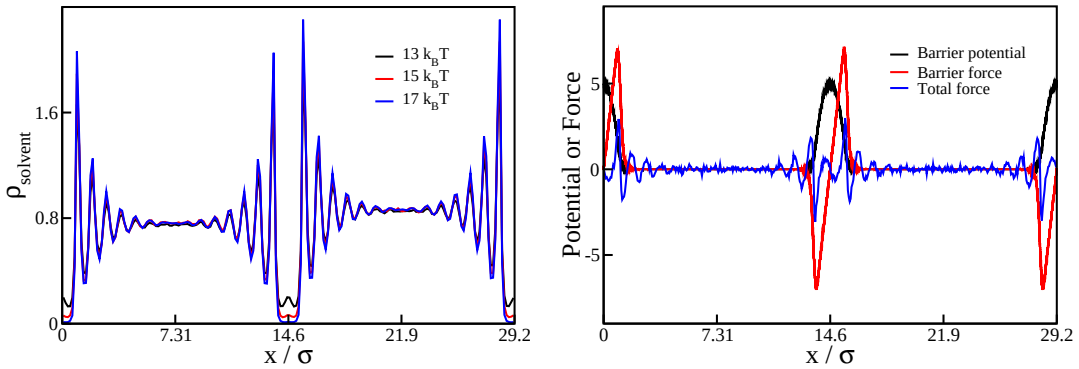

Figure 6.2 Steady-state solvent density profiles are shown for three different barrier heights in panel (a). In panel (b) the steady-state average potential and force profiles that a solvent particle experiences due to the barrier (of height $H = 5\ k_BT$) are shown in black and red. The blue data corresponds to the steady-state average total force that a solvent particle experiences in the simulations with a 5 k_BT barrier.

6.3 Is the osmotic flow an exponential relaxation process?

In this chapter we study the relaxation dynamics of the solvent particles in both osmotic and pressure-driven flows. For the pressure-driven flows we initially place more particles on the LHS of the membrane than on the RHS. Subsequently, the simplest hypothesis that we might conceive of is that the density imbalance across the membrane be redressed by an exponential decay in the number of particles on the LHS of the

membrane:

$$N_L(t) = N_L^{ss} - (N_L^{ss} - N_L^0)\mathrm{e}^{-\lambda_p t}, \tag{6.1}$$

where λ_p is a transport coefficient associated with the net flux of solvent particles across the membrane in the case of a pressure-driven flow. N_L^0 in Eq.(6.1) is the initial number of particles on the LHS of the membrane and N_L^{ss} is the steady-state number of particles on the LHS, $N_L^{ss} = N/2 = 2500$, where N is the total number of particles in the simulation.

Assuming that osmotic flows are similar to pressure-driven flows (see Section 6.4), then Eq.(6.1) can also be used to study the relaxation dynamics in osmosis. In this case, however, equal numbers of particles are initially placed on either side of the membrane, such that $N_L^0 = N/2 = 2500$ and $N_L^{ss} > N_L^0$, and a net number of solvent particles will move from right to left, into the solution compartment, by osmosis prior to the steady state.

By re-arranging Eq.(6.1) slightly we arrive at the following relation,

$$\log\left[\frac{N_L^{ss} - N_L(t)}{N_L^{ss} - N_L^0}\right] = -\lambda_p t, \tag{6.2}$$

which we expect to decrease linearly as a function of time in our simulations, as shown in Figure 6.3(a). The results of Eq.(6.2), measured in our simulations using a barrier height, $H = 15\ k_BT$, are shown in Figure 6.3(b); in the main panel for a solute concentration, $c_s = 0.32\ \sigma^{-3}$, and in the inset using a solute concentration, $c_s = 0.11\ \sigma^{-3}$. For the higher solute concentration we observe two distinct regimes in the solvent dynamics. At early times there is an initial rapid flux of solvent particles into the solution, before the flow settles down at later times ($t > 40t^*$) to a slower flux of particles into the solution. Although this behaviour is not as apparent when using a lower solute concentration (inset to Figure 6.3(b)), it is not completely clear that the dynamics in this case are well described using Eq.(6.2) due to the noise in the data. Thus, for our simple setup, we are not able to determine whether or not Eqs.(6.1) and (6.2) describe the data well at low solute concentrations; at higher solute concentrations these relations certainly do not capture the behaviour of the system, which appears to be more complex.

Whether or not such an expression can be used to describe the relaxation dynamics

prior to the steady state for a pressure-driven flow will be addressed in the next section where we compare the solvents' relaxation dynamics in osmotic and pressure-driven flows.

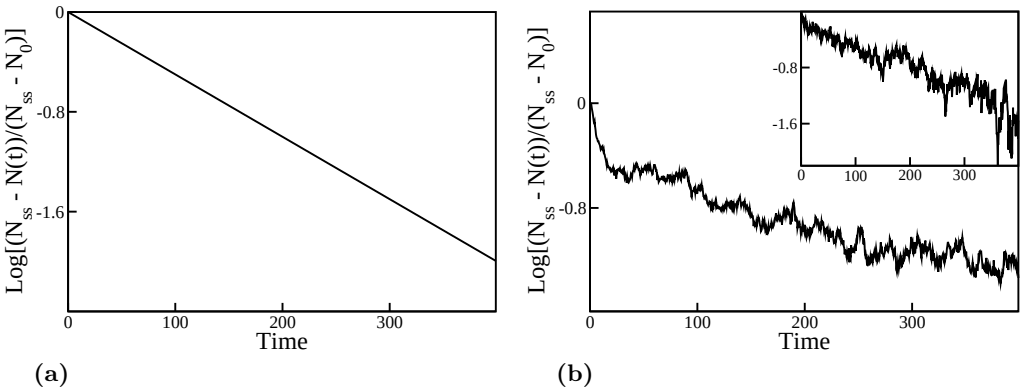

Figure 6.3 Expression (6.2) is shown as a function of time, both assuming the relaxation is exponential and using results from simulations. In panel (a) Eq.(6.2) is plotted as a function of time assuming $N_L^0 = 2500$, $N_L^{ss} = 2509$ and $\lambda_p = 0.05$. In panel (b) results from simulations using a barrier height, $H = 15\ k_BT$, are shown; in the main panel simulations contain a solute concentration, $c_s = 0.32\ \sigma^{-3}$, and in the inset, $c_s = 0.11\ \sigma^{-3}$.

6.4 Equivalence of pressure-driven and osmotic flows

Both experimental [92, 93, 162] and simulation [76] work has suggested that pressure-driven flows through a porous membrane proceed in an equivalent manner to osmotic flows. This is typically demonstrated either by measuring the pressure profile in the pore of the membrane and demonstrating that this is the same for the two setups or, as discussed in the introduction to this chapter, by demonstrating that the two flows proceed at equivalent rates, *i.e.* the same membrane filtration coefficient, L_p, can be used to describe both types of flow. We first test whether our simple system reproduces this result by recording the solvent flow across the membrane using both an osmotic and a pressure-driven setup.

6.4.1 Solvent transfer in the period prior to the steady state

To compare the solvent transfer across the barrier as a function of time in both our osmotic and pressure-driven setups we plot the results of Eq.(6.2) for both types of flow in Figure 6.4. To ensure that a like-for-like comparison can be made, our simulations of osmotic and pressure-driven flows are initialised with the same chemical potential

gradient, *i.e.* N_L^0 is chosen for the pressure-driven flows so that the initial chemical potential gradient, calculated using the standard statistical mechanical relation (see Section 6.1), is the same as in the osmotic simulations, containing a mixture of solute and solvent particles. Simulations have been conducted using three different chemical potential gradients (corresponding to solute concentrations, $c_s = 0.11,\ 0.21$ and $0.32\ \sigma^{-3}$) with a barrier height of $H = 15\ k_BT$. The two flows are in excellent agreement for the duration of the systems' relaxation to the steady state for each of the three chemical potential gradients studied in Figure 6.4, thus demonstrating that the flows proceed at equivalent rates. The agreement of the two types of flow shown in Figure 6.4 means we must also conclude that, as for the osmotic flows, Eqs.(6.1) and (6.2) do not describe the relaxation of the system in the pressure-driven case across a wide range of chemical potential gradients.

Interestingly, Finkelstein and others [42, 92] have suggested that the equivalence of the two types of flow through porous membranes is due to their having equivalent pressure profiles within the pore. If this is true in our setup, *i.e.* the pressure across the membrane is the same for the osmotic and pressure-driven flows, it would explain the results shown in Figure 6.4.

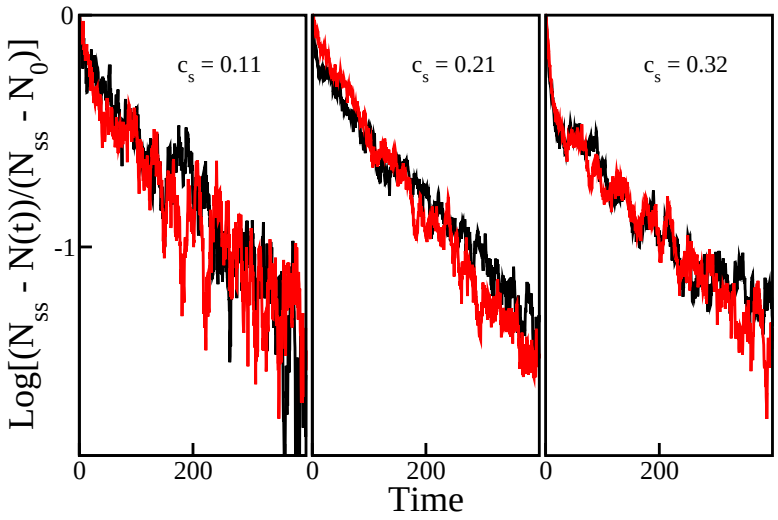

Figure 6.4 The equivalence between flows driven by an osmotic gradient and a hydrostatic pressure gradient is shown by studying the results of Eq.(6.2) as a function of time for both types of flow. The results for the osmotic system, containing solute particles but no initial density gradient across the membrane, are shown by the black lines. The results for the equivalent, pressure-driven system, which contains no solute particles but which is initialised with a density gradient across the membrane, are shown by the red lines. Results for three different gradients in the solvent chemical potential are illustrated; the chemical potential gradient increases from left to right.

6.4.2 Pressure profiles during the relaxation to the steady state

Motivated by this conjecture, pressure profiles across the membrane region in the period prior to the steady state were measured. To compute the pressure, the method of planes technique outlined in Section 3.2.3 was used and seven planes were placed at sequential locations through the membrane (the centre of the membrane corresponds to $x = 14.6\ \sigma$ in Figure 6.2(a)). Using these planes, the pressure profile was recorded at three times for a 15 k_BT barrier and an intermediate chemical potential gradient (corresponding to $c_s = 0.21\ \sigma^{-3}$) for both the osmotic simulations and for the pressure-driven system. These times corresponded to before the barrier was truncated, shortly after the barrier was truncated and at an intermediate point during the system's relaxation to the steady state. The results are shown in Figure 6.5(a). The black data represent the first measurement, the red data the second and the blue data the final measurement; the circles show the results from osmotic simulations and the triangles show results from the pressure-driven simulations. At all times the pressure profile for the osmotic flow is in excellent agreement with the pressure-driven flow. This is emphasised in Figure 6.5(b), where the difference between the pressure profiles for the two setups is plotted. Note the scale on the $y - axis$ in Figure 6.5(b) is significantly reduced in comparison to that in Figure 6.5(a). Thus, as was speculated in the last section, the reason that the two setups demonstrate equivalent flows is likely because the pressure profiles are equivalent for the two systems.

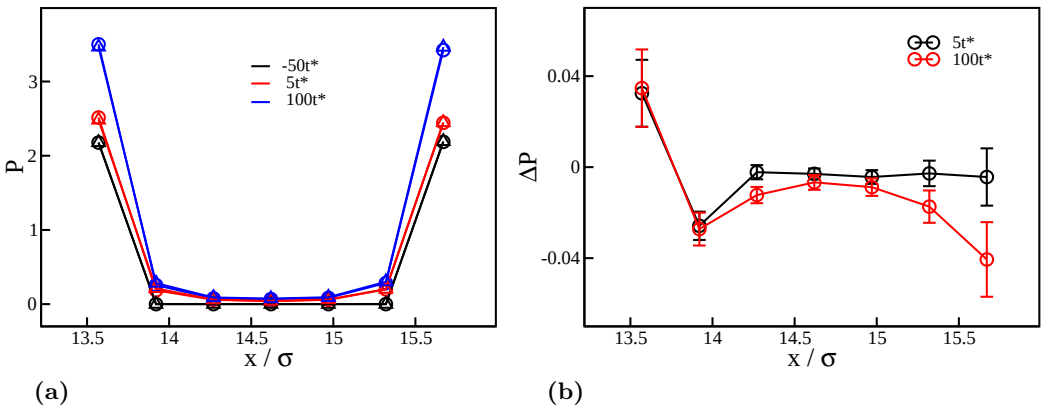

Figure 6.5 Pressure profiles across the membrane are shown at various times for both osmotic and pressure-driven flows. In the figures, $t^* = 0$ corresponds to the time at which the barrier is truncated. Panel (a) shows the total pressure profiles for the two systems at three different times: before the barrier is truncated (black); shortly after the barrier is truncated (red); and at a later time in the system's relaxation (blue). The pressure profile for the osmotic simulations is shown by the circles and the pressure-driven data is shown by the triangles. The two results appear to be almost indistinguishable in the figure. In panel (b) the difference in the pressure profile between the osmotic system and the system containing a pressure-driven flow is shown at two different times in the simulations.

6.5 Theory and simulation of tracer flows

Having established that osmotic and pressure-driven flows are equivalent, we subsequently study only the latter scenario. However, we no longer study the change in the total number of particles on the LHS of our membrane, $N_L(t)$, for our pressure-driven flows, instead we track the flow of tracer particles across the membrane. These have the distinct advantage that better statistics are obtained because we record the net movement of a larger number of particles.

A diagram illustrating the tracer experiment is shown in Figure 6.6; put simply, this experiment measures the rate at which the particles on either side of the membrane mix. We begin our tracer simulations by labeling all of the particles on the RHS of the membrane (the blue particles in Figure 6.6). We then record the fraction of the particles on the LHS which correspond to tracers that have moved across the membrane from the RHS to the LHS, which we denote $\phi_L(t)$, over the course of the simulation. Initially, ϕ_L is zero and in the steady state the tracer particles will distribute themselves evenly across the membrane such that $\phi_L^{ss} = \rho_R^0/2\rho$, where ρ_R^0 is the initial density of particles on the RHS and ρ is the average density in the system $(= (\rho_L(t) + \rho_R(t))/2)$.

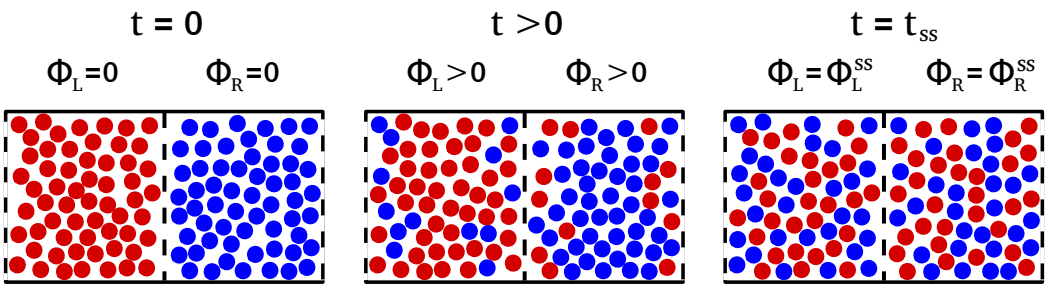

Figure 6.6 Diagram to illustrate the mixing of tracer particles between the left and right compartments. At $t = 0$ the particles on either side of the membrane are labeled (red and blue in the figure). The tracer particles subsequently mix into the opposite compartment as time progresses. During this time we record the fraction of particles on the opposite side of the membrane that are tracers at time t. The steady-state values ($t = t_{ss}$) for $\phi_L(t)$ and $\phi_R(t)$ are outlined in the main text.

Based on what we have observed thus far, we do not necessarily expect the mixing of tracer particles in our pressure-driven flows to obey an exponential relationship. Nevertheless, we use similar expressions to Eqs.(6.1) and (6.2) as, particularly the latter, allows for a clear comparison of the results of simulation with theory (yet to be outlined). The resulting expressions are given below in Eqs.(6.3) and (6.4), where λ_t is a transport coefficient associated with the transfer of tracer particles across the membrane.

$$\phi_L(t) = \phi_L^{ss} - (\phi_L^{ss} - \phi_L^0)\mathrm{e}^{-\lambda_t t}, \tag{6.3}$$

$$\log\left[\frac{\phi_L^{ss} - \phi_L(t)}{\phi_L^{ss} - \phi_L^0}\right] = -\lambda_t t. \tag{6.4}$$

In addition to tracking the movement of tracer particles across the membrane from right to left, we can also track tracer particles which were originally on the LHS of the membrane (the red particles in Figure 6.6). To do this we simply label all of these particles at $t = 0$ and subsequently record the fraction of particles on the RHS which correspond to tracers that have moved from the LHS to the RHS of the membrane at time t, $\phi_R(t)$. As above, $\phi_R = 0$ at $t = 0$ and in the steady state the tracers will distribute themselves evenly across the membrane such that $\phi_R^{ss} = \rho_L^0/2\rho$, where ρ_L^0 is the initial density of particles on the LHS of the membrane. Similar relationships to Eqs.(6.3) and (6.4) can then be written down for $\phi_R(t)$.

Expression (6.3) is plotted as a function of time in Figure 6.7 for two pressure-driven

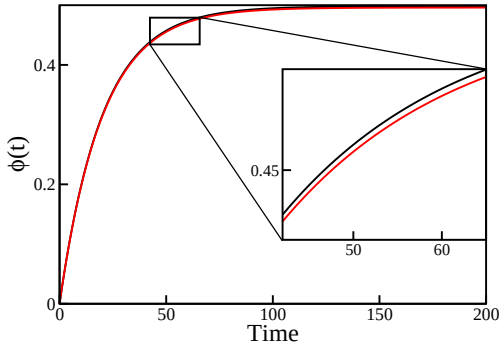

Figure 6.7 The mixing of tracer particles as a function of time is shown by recording the fraction of particles, initially on the opposite side of the membrane to the tracers, that are tracers at time t. The results are shown according to Eq.(6.3) using $\phi_L^0 = 0$ and $\phi_L^{ss} = 0.498,\ 0.496$, corresponding to solute concentrations, $c_s = 0.2$ and $0.4\ \sigma^{-3}$. In the inset a small region of the data has been magnified to highlight the different rates of tracer mixing in the two cases.

flows, equivalent to osmotic flows at solute concentrations, $c_s = 0.2\ \sigma^{-3}$ and $c_s = 0.4\ \sigma^{-3}$, the black and red lines, respectively.

A key objective in this chapter is to determine whether or not the solvent flow across the barrier in the osmotic and pressure-driven flows is diffusive in the period prior to the steady state. To address this question, we need a theoretical prediction for the rate of diffusive flow down a chemical potential gradient in our setup. In the following section we derive a relation for the rate of tracer particle flux across the barrier using Kramers' theory. Later on we will attempt to apply this to the net flow of solvent particles across the membrane in a pressure-driven flow.

6.5.1 Kramers' theory and a theoretical expression for the diffusion of tracer particles across the barrier

Kramers' theory was originally proposed as a method for calculating the rate at which chemical reactions take place – by overcoming potential energy barriers through Brownian motion [78]. However, it has since proved useful in describing a host of other barrier crossing problems, such as protein folding [112], single-molecule force spectroscopy measurements [31] and the kinetics of ion channel gating [142]. Since the solvent particles in our simulations have to overcome a free energy barrier to cross the membrane, it seems appropriate to use Kramers' theory to describe this process. Furthermore, because the particles in Kramers' theory cross the barrier individually, by acquiring sufficient kinetic energy from random fluctuations, it predicts the rate at which barrier crossings occur in the purely diffusive case. Therefore, by obtaining

a prediction for the rate of solvent transfer from this theory and comparing it to simulation data, we should be able to distinguish between diffusive and non-diffusive flows in our simulations.

According to Kramers' theory, the key quantity which affects the rate at which particles cross a barrier from left to right is the difference between the chemical potential at the top of the barrier, μ_B, and the chemical potential to the left of the barrier, μ_L. The rate, κ_{LR}, at which particles cross the barrier from left to right can be expressed as follows: $\kappa_{LR} = P\mathrm{e}^{-(\mu_B-\mu_L)/k_BT}$, where P is assumed to be a constant which is equal for left and right crossings. A similar equation can also be written down for the counter flux of particles from right to left. Applying this approach to our simulations, and noting that the rate of attempted barrier crossings is also proportional to the particle density in a region close to the membrane, we find that the net flux of particles from left to right can be expressed as

$$\begin{aligned} j(t) &= \Delta x \left[\rho_L(t)\kappa_{LR} - \rho_R(t)\kappa_{RL}\right] \\ &= P\Delta x \left[\rho_L(t)\mathrm{e}^{-(\mu_B-\mu_L)/k_BT} - \rho_R(t)\mathrm{e}^{-(\mu_B-\mu_R)/k_BT}\right] \\ &= C \left[\rho_L(t)\mathrm{e}^{\mu_L/k_BT} - \rho_R(t)\mathrm{e}^{\mu_R/k_BT}\right]. \end{aligned} \tag{6.5}$$

In Eq.(6.5), $\rho_L(t)$ and $\rho_R(t)$ are the density of particles on the left and right hand side of the barrier at time t and Δx represents a narrow region near to the barrier. Thus, $\rho_L(t)\Delta x$ is approximately equal to the number of particles per unit area in the region near to the left side of the barrier and $C = P\Delta x\mathrm{e}^{-\mu_B/k_BT}$ is a constant. In Appendix B it is demonstrated that $C = \lambda_d L\mathrm{e}^{-\mu^{ex}(\rho)}/2\rho\Lambda^3$, where $\lambda_d = \lambda_t$ in a purely diffusive tracer experiment, L is the length of the solution/solvent compartment, $\mu^{ex}(\rho)$ corresponds to the excess part of the chemical potential and ρ is the average density in the system ($= (\rho_L(t) + \rho_R(t))/2$). Our goal in this section, therefore, is to derive an expression for the flux of tracer particles across the membrane from Eq.(6.5) which we can integrate over time and compare to the results from our MD simulations.

We begin by writing down an expression for the rate of change in the total density of particles on the LHS of the membrane were this process to take place in a purely diffusive manner. Using Eq.(6.5) we establish the following relation for our pressure driven flows:

$$\frac{d\rho_L(t)}{dt} = -\frac{\lambda_d \mathrm{e}^{-\mu^{ex}(\rho)}}{2\rho}\left[\rho_L^2(t)\mathrm{e}^{\mu_L^{ex}(\rho_L(t))} - \rho_R^2(t)\mathrm{e}^{\mu_R^{ex}(\rho_R(t))}\right], \tag{6.6}$$

where we have substituted $\mu_L/k_BT = \log\left[\rho_L(t)\Lambda^3\right] + \mu_L^{ex}(\rho_L(t))$ in for the chemical potential on the LHS (see Section 6.1) and used an equivalent relation for the chemical potential on the RHS. To study the flux of tracer particles across the barrier we use the relation $\rho_L^{tr}(t) = \rho_L(t)\phi_L(t)$, where $\rho_L^{tr}(t)$ is the density of tracer particles on the LHS of the membrane. We can therefore write

$$\begin{aligned}\frac{d\rho_L^{tr}(t)}{dt} &= \frac{d(\rho_L(t)\phi_L(t))}{dt} \\ &= \phi_L(t)\frac{d\rho_L(t)}{dt} + \rho_L(t)\frac{d\phi_L(t)}{dt} \\ &= -\frac{\lambda_d \mathrm{e}^{-\mu^{ex}(\rho)}}{2\rho}\left[(\rho_L(t)\phi_L(t))^2\mathrm{e}^{\mu_L^{ex}(\rho_L(t))} - (\rho_R(t)\phi_R(t))^2\mathrm{e}^{\mu_R^{ex}(\rho_R(t))}\right].\end{aligned} \tag{6.7}$$

By substituting Eq.(6.6) into Eq.(6.7) we can simplify our expression for the rate of change of $\phi_L(t)$ slightly:

$$\begin{aligned}\rho_L(t)\frac{d\phi_L(t)}{dt} = -\frac{\lambda_d \mathrm{e}^{-\mu^{ex}(\rho)}}{2\rho}\Big[&\rho_L^2(t)\mathrm{e}^{\mu_L^{ex}(\rho_L(t))}(\phi_L^2(t) - \phi_L(t)) \\ &- \rho_R^2(t)\mathrm{e}^{\mu_R^{ex}(\rho_R(t))}(\phi_R^2(t) - \phi_L(t))\Big].\end{aligned} \tag{6.8}$$

Finally, we re-write the densities on the left and right hand sides of the membrane in terms of perturbations from the average density in the system, such that $\rho_L(t) = \rho + \Delta\rho(t)$ and $\rho_R(t) = \rho - \Delta\rho(t)$. We further assume that $\Delta\rho(t)$ is small so that the excess part of the chemical potential can be expanded to first order[1] about the average density in the system. This enables us to cancel the leading order term in the expansion of $\mathrm{e}^{\mu^{ex}(\rho\pm\Delta\rho(t))}$ with the excess chemical potential at the front of Eq.(6.8). The final result for the rate of change of $\phi_L(t)$ is, therefore,

[1] Higher order terms make a negligible contribution to the overall result.

$$\frac{d\phi_L(t)}{dt} = -\frac{\lambda_d}{2\rho(\rho+\Delta\rho(t))}\Big[(\rho+\Delta\rho(t))^2(\phi_L^2(t)-\phi_L(t))\mathrm{e}^{\frac{d\mu^{ex}(\rho)}{d\rho}\Delta\rho(t)} - (\rho-\Delta\rho(t))^2(\phi_R^2(t)-\phi_L(t))\mathrm{e}^{-\frac{d\mu^{ex}(\rho)}{d\rho}\Delta\rho(t)}\Big]. \quad (6.9)$$

Equation 6.9 constitutes a direct prediction for the diffusive dynamics of the solvent relaxation in terms of tracer particles initially situated on one side of the membrane, provided we know the diffusive transport coefficient λ_d.

6.5.2 Comparison of simulation data with the predictions of theory

We are now in a position to determine whether or not the tracer flow in our MD simulations is diffusive by comparing the numerical integration of Eq.(6.9) to the results from our MD simulations containing labeled tracer particles. First, however, we must determine the value of λ_d corresponding to pure diffusion.

Determining λ_d

To simulate pure diffusion a similar setup to the tracer experiment described above is used, except we now initialise the system with equal numbers of particles on either side of the membrane. We subsequently study the relaxation of the tracer particles across the membrane using Eq.(6.4). In Figure 6.8, Eq.(6.4) is shown as a function of time using the data for $\phi_L(t)$ from our MD simulations. The different colours correspond to three different barrier heights ($H = 13,\ 15$ and $17\ k_BT$). A line of best fit is then drawn through the data shown in Figure 6.8 and the value of λ_d associated with the diffusive transport of particles across the three barriers is determined. The results are shown in Table 6.1.

Table 6.1 The different values for λ_d, computed from Figure 6.8 are shown along with their corresponding errors for the 13, 15 and 17 k_BT barriers studied in this chapter.

Barrier Height (k_BT)	λ_d (1/t*)	Error
13	2.1e-3	1.9e-6
15	1.2e-3	9.6e-7
17	4.1e-4	2.5e-7

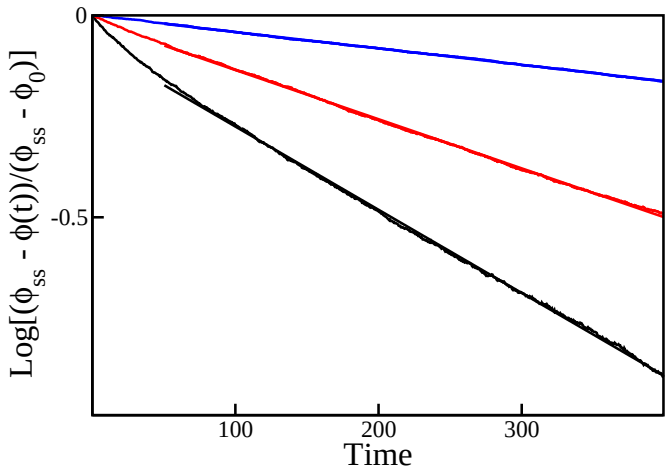

Figure 6.8 Expression (6.4) is shown subsequent to the membrane's truncation for the solvent particles in a purely diffusive system with no initial chemical potential gradient, but in which all of the particles on one side of the membrane are initially labeled as tracer particles. Subsequently, the fraction of particles on the opposite side of the membrane that are tracers is monitored. Results are shown are for three different barrier heights: $H = 13\ k_BT$ (black), $15\ k_BT$ (red) and $17\ k_BT$ (blue). By fitting lines of best fit to the data, the diffusive transport coefficient, λ_d, can be computed for each of the barrier heights shown.

Comparing theoretical prediction to simulations for the pressure-driven flow

Equation (6.9) can now be solved numerically using Euler's method [55] and inserting the value of λ_d obtained from our purely diffusive simulations (see Table 6.1). In Figure 6.9(a) we compare the predictions of Eq.(6.9), based on the diffusive transfer of solvent particles, to our MD simulations of pressure-driven flows, having initially labeled all of the particles on the RHS of the membrane as tracers. Results are shown for three different chemical potential gradients (corresponding to solute concentrations, $c_s = 0.11,\ 0.21$ and $0.32\ \sigma^{-3}$) with a barrier height of $15\ k_BT$. In the inset to the figure the theoretical and MD results for a chemical potential gradient equivalent to $c_s = 0.11\ \sigma^{-3}$ have been isolated and magnified to clarify the agreement between the simulation data and the prediction of theory. Thus, for each of the chemical potential gradients studied, the prediction of theory agrees well with the results of MD simulations, supporting the notion that the transfer of particles across the membrane prior to the steady state is a diffusive process. Furthermore, it would appear that, based on the results presented in Figure 6.9, the magnitude of the initial chemical potential gradient does not play a significant role in driving the transfer of tracer particles across the membrane. This result is perhaps somewhat counter-intuitive. However, as can be observed in the results shown in Figure 6.11, modifying the chemical potential gradient does in fact have some effect on the rate of change of $\phi_L(t)$; though it would appear that for the

tracer experiments this effect is small.

In Figure 6.9(b) we plot the same result for a system in which the chemical potential gradient is held fixed (equivalent to $c_s = 0.21\ \sigma^{-3}$), but for which we now vary the barrier height. Once again the agreement between theory and simulation at later times is good. However, for the lower barrier heights (in particular the 13 k_BT barrier), the dynamics of the solvent particles in our MD simulations do not match the prediction of theory at early times. Instead, the solvent particles cross the barrier more rapidly than is predicted by the diffusive model.

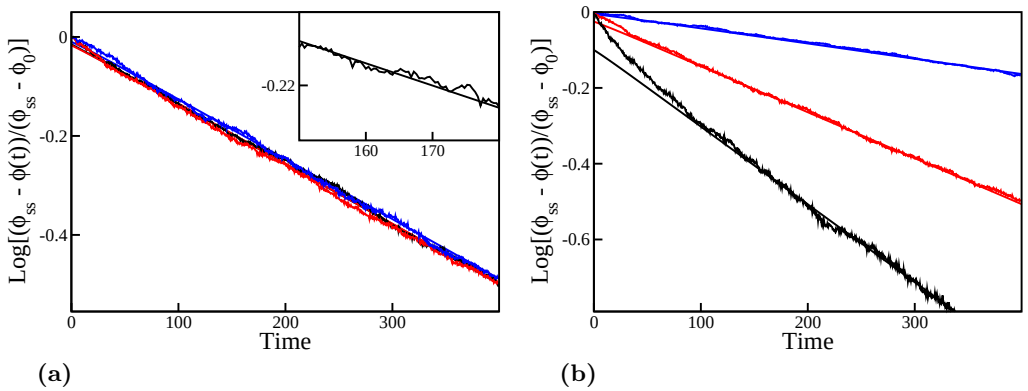

Figure 6.9 In panel (a) the results of theory and MD simulation are presented alongside one another for the fraction of RHS tracers which are in the left hand compartment as a function of time. A 15 k_BT barrier is used and three different chemical potential gradients have been studied. The black data corresponds to a solute concentration, $c_s = 0.11\ \sigma^{-3}$, the red data to $c_s = 0.21\ \sigma^{-3}$ and the blue data to $c_s = 0.32\ \sigma^{-3}$. The theoretical predictions in black, red and blue have been shifted down slightly so that they fit the results from the MD simulations. In the inset, the data equivalent to a solute concentration, $c_s = 0.11\ \sigma^{-3}$, has been isolated to emphasise the agreement between simulation and theory. In panel (b) similar results are shown for a fixed chemical potential gradient, corresponding to $c_s = 0.21\ \sigma^{-3}$, but over three different barrier heights, $H = 13$, 15 and 17 k_BT in black, red and blue, respectively. Once again, the results from the theoretical computations have been shifted down the $y-axis$ to highlight the agreement in the gradients at later times between simulation and theory.

It is worth considering whether this effect is also apparent for the solvent flow in the opposite direction, from the LHS to the RHS. We therefore study the equivalent relation for the tracers on the opposite side of the membrane, $\phi_R(t)$. The results in Figures 6.10(a) and (b) demonstrate that the effect is indeed also apparent for the flow from left to right and that the theory, as it stands, does not adequately reproduce the dynamics of the solvent particles in those times shortly after the barrier is truncated.

Interestingly, as is shown in Figure 6.8, the discrepancy between the tracer dynamics and Kramers' theory is also observed at early times for the purely diffusive scenario,

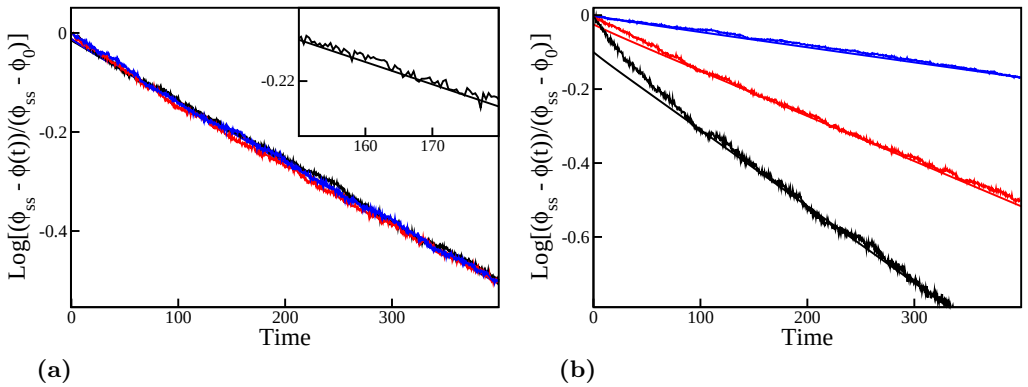

Figure 6.10 Similar results to those described in Figure 6.9 are presented, except here we study the fraction of tracer particles initially situated on the LHS of the membrane which are now on the RHS of the membrane. As in Figure 6.9, the data in panel (a) has been taken over three different chemical potential gradients at a fixed barrier height, whereas the data in panel (b) has been taken over three different barrier heights using a fixed chemical potential gradient. Similar offsets to those described in the caption to Figure 6.9 are applied here.

in the absence of a chemical potential gradient. The effect becomes most pronounced for lower barrier heights and its origins will be further discussed in Section 6.6. Were one able to factor this effect into Kramers' theory, it might be possible to reconcile the discrepancies in the tracer dynamics observed during the early times in Figures 6.9 and 6.10.

6.5.3 Does Kramers' theory capture osmosis?

At first glance, the predictions of Kramers' theory for the solution and bath tracers shown in Figures 6.9 and 6.10 appear to be linear (when plotted on a log-linear plot) with identical gradients, such that $d\phi_R(t)/dt = d\phi_L(t)/dt$. If this were in fact the case, then Kramers' theory would not capture the net movement of particles across the membrane from left to right prior to the steady state in the pressure-driven flows studied above. In Figure 6.11 we isolate the predictions of Kramers' theory for three different chemical potential gradients (equivalent to $c_s = 0.11,\ 0.21$ and $0.32\ \sigma^{-3}$) with a barrier height, $H = 15\ k_BT$. The results shown in Figure 6.11 reveal that, at early times, Kramers' theory predicts that the mixing of tracer particles into the RHS occurs faster than the counter-flux of tracer particles into the LHS (as expected if we consider Eq.(6.9)). We further note from Figure 6.11 that the difference between the tracer fluxes is dependent on the chemical potential gradient across the membrane, with a greater asymmetry occurring when larger chemical potential gradients are used.

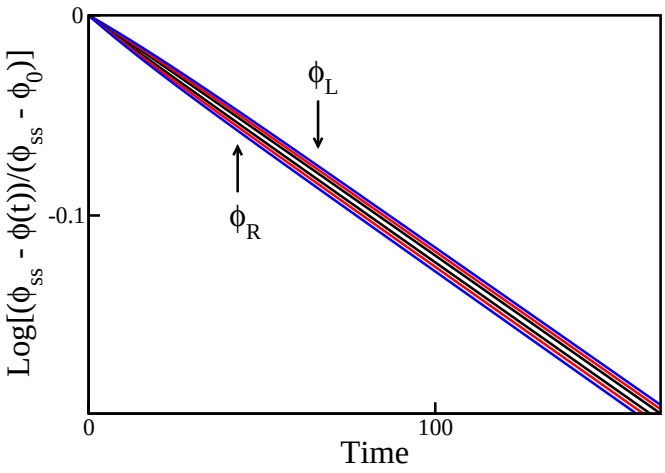

Figure 6.11 The results of integrating Eq.(6.3) over time are shown for both $\phi_R(t)$ and $\phi_L(t)$, where $\phi_R(t)$ represents the fraction of particles on the RHS which are tracers that have moved from the left to the right compartment and $\phi_L(t)$ represents the flux of tracers which have moved from the RHS to the LHS. Results are illustrated for three different chemical potential gradients, corresponding to solute concentrations, $c_s = 0.11,\ 0.21$ and $0.32\ \sigma^{-3}$, by the black, red and blue lines, respectively.

Satisfied that Kramers' theory does in fact predict a net movement of particles across the membrane prior to the steady state, we are now in a position to compare the predictions of Kramers' theory, based on the diffusive transfer of solvent across the barrier, with the results of our pressure-driven simulations. To do this we must first recover the value for $N_L(t)$, the total number of particles on the LHS of the membrane at time t, from the values for $\phi_L(t)$ and $\phi_R(t)$ in our theory. This is achieved using the following relation:

$$N_L(t) = N_L(t)\phi_L(t) + (N_L^0 - N_R(t)\phi_R(t)), \tag{6.10}$$

where $N_R(t)$ is the total number of particles on the RHS of the membrane at time t. In Eq.(6.10) we have simply stated that $N_L(t)$ is equal to the number of tracers on the LHS at time t that were originally on the RHS of the membrane plus the number of tracers on the LHS at time t that were originally on the LHS of the membrane. Re-arranging Eq.(6.10) slightly we are left with the following form for $N_L(t)$:

$$N_L(t) = \frac{N_L^0 - N\phi_R(t)}{1 - \phi_L(t) - \phi_R(t)}, \tag{6.11}$$

in which N is the total number of particles in the simulations ($= 5000$). This result has been verified using data from simulations.

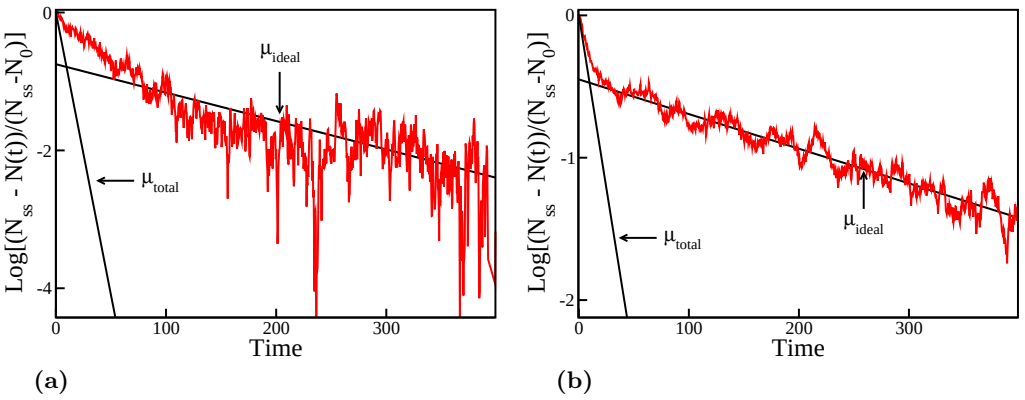

Figure 6.12 Comparison of the prediction from Kramers' theory for the net rate of solvent transfer across the membrane using solvent tracers with data from simulations of a pressure-driven flow. In panel (a) expression (6.2) is plotted as a function of time for the 13 k_BT barrier using a chemical potential gradient equivalent to $c_s = 0.21\ \sigma^{-3}$ (red line in figure). The predictions of theory are also shown having integrated expression (6.9) using both the total chemical potential and having only included the ideal part (black lines in the figure). Similar results are shown in panel (b) for a 15 k_BT barrier and a chemical potential gradient equivalent to $c_s = 0.32\ \sigma^{-3}$.

In Figures 6.12(a) and (b) we compare the results of theory and simulation for the total number of particles on the LHS of the membrane as a function of time for the 13 and 15 k_BT barriers using chemical potential gradients equivalent to $c_s = 0.21\ \sigma^{-3}$ and $c_s = 0.32\ \sigma^{-3}$, respectively. Interestingly, when the theory is integrated including a full evaluation of the chemical potential, *i.e.* taking $\mu_{total} = \mu_{ideal} + \mu_{excess}$, the early time dynamics of the simulations are well reproduced. However, at later times, inclusion of the excess part of the chemical potential predicts a much sharper rate of change in the number of particles than is observed in the simulations. That the simulation data and the predictions of theory are not in agreement is perhaps not surprising considering we derived our value for λ_d from Eq.(6.3); a relation we subsequently demonstrated did not hold for the tracer particles at early times. Rather strangely though, the results of simulation and theory are once again in agreement if we integrate Kramers' theory using only the ideal part of the chemical potential. This would, therefore, seem to suggest that the later transfer of solvent in osmosis proceeds at a rate which is slower than diffusion. It is not clear why this is the case and why the results of Kramers' theory using only the ideal part of the chemical potential produce results in agreement with the later time dynamics of the solvent particles. This finding warrants further investigation as it appears to be a somewhat counter-intuitive result.

6.6 Discussion

Currently, there is no clear understanding of the nature of the solvent transfer across the membrane in osmosis, even in the most simple of systems. By simulating a simple double box, finite membrane setup we have attempted to isolate the underlying nature of the osmotic transport of solvent particles in our setup.

Initially we proposed a very simple hypothesis to explain the relaxation of the system towards the steady state, that is an exponential-type behaviour in the total number of particles on one side of the membrane. By comparing our prediction to the results of simulation, we concluded that the dynamics of the solvent particles in the period prior to the steady state are rather more complicated. At higher solute concentrations a transition occurred between an initial more rapid flux of particles into the solution compartment compared to the later, slower rate of solvent transfer across the membrane. This behaviour was also confirmed for systems driven by a pressure gradient across the membrane and we demonstrated that, in our system, osmotic flows are equivalent to pressure-driven flows. This equivalence was explained by comparing the pressure profiles across the membrane for the two setups.

Using Kramers' theory we outlined a diffusive model for the flow of tracer particles across the membrane, which produced results in excellent agreement with those of simulation data at later times. This is to be expected because, certainly at later times, we do not suppose the transfer of solvent particles across our membrane to proceed by any means other than diffusion. At early times the dynamics in our simulations containing labeled tracer particles demonstrated a slightly faster rate of solvent flow than was predicted by theory. However, this was also apparent in the purely diffusive scenario, where the system was initialised without a chemical potential gradient across the membrane. When we used the tracers to describe the osmotic flow in our system, however, we discovered that the opposite effect was apparent. Here, we observed that the diffusive model somewhat reproduced the early time dynamics of the osmotic flow, but over-predicted the rate of net solvent transfer across the membrane at later times. This latter effect certainly warrants further investigation; possibly it requires us to revisit Kramers' theory and the determination of the value of λ_d that we use to characterise the net solvent transfer in osmosis.

To end the chapter I discuss a simple hypothesis which attempts to explain the transitions in the rate of solvent flows observed between early and late times in our simple double box, finite membrane setup. We begin by considering the simplest

case, in which there is no chemical potential gradient across the membrane, *i.e.* no solute particles and no imbalance in the total density of particles across the membrane. As the barrier is truncated for the solvent particles in this setup, we create some additional volume on either side of the membrane into which the particles can move (equivalent to an increase in the system's entropy). The newly created volume produces an initial rapid flux of particles across the barrier in both directions, equivalent to a wave of particles moving in either direction, thus explaining the deviations from linear behaviour observed for the labeled tracers in Figure 6.8. This hypothesis is also consistent with the observation that these deviations grow larger as the barrier height, H, is reduced in Figure 6.8.

This explanation can also be applied to the pressure-driven flows (in which $\rho_L^0 > \rho_R^0$), provided that we allow for the fact that, upon truncation of the barrier, more particles on the LHS can move into this "gap". Subsequently, we are left with more particles near to the top of the barrier on the LHS of the membrane, creating a slight pressure gradient in the system which pushes these particles more rapidly over the barrier than the counter-flux of particles moving in the other direction. As the density gradient across the membrane increases this effect becomes larger, as shown in Figure 6.4. Eventually, at later times in the simulations, the density imbalance becomes small enough that particles cross the barrier on a single particle basis, at which point the exponential relation, Eq.(6.1), may capture the dynamics of relaxation.

For the osmotic simulations, although we do not start the system off with an initial imbalance in the total number of particles on either side of the membrane, the barrier is only truncated for the solvent particles. Thus, the initial "wave" of particles in this case is more heavily populated by particles moving from the RHS into the LHS, creating an equivalent (but opposite) effect to that present in the pressure-driven simulations. The solute particles can therefore be thought of as blocking the solvents' movement into the newly created volume. The initial more rapid flow of solvent will, therefore, subside once this initial blocking effect is overcome and the density of particles slightly to the left and right hand side of the membrane barrier is redressed. Although measured in the steady state, the density profiles shown in Figure 6.2(a) support the notion that the density of particles on the barrier is influenced by the barrier height used adding credence to our proposed explanation for the transition in the solvent flow between early and late times. Despite the fact that this explanation predicts the transition in the rate of flows between early and late times, it does not, however, account for the net rate of solvent transfer in the pressure-driven/osmotic simulations at later times, which proceeds slower than diffusion.

To test our hypothesis we would need to resolve the pressure profiles across the membrane on a much finer scale than we have done so far. This is because the density gradients that we initially introduce in our system are very small, even for the case of larger solute concentrations.

As a final point, I note that the explanation we have outlined for the initial more rapid flux of solvent particles in osmotic and pressure-driven flows is similar to that proposed by Dainty [28, 29] for porous membranes (see Section 1.2.2), although no such transition between early and late time dynamics was discussed by Dainty. This is likely because the early time dynamics using a porous setup are significantly extended in comparison to our setup, as the solvent particles can only move across the membrane at specific locations, which the solute particles can more readily block. The transition we observe in the solvent dynamics is also consistent with the results of Vegard [162], discussed in Chapter 1, Section 1.2.1, who also observed, albeit using a porous setup, an initial rapid flux of solvent particles into the solution at higher solute concentrations.

Further work should investigate in more detail why Kramers' theory apparently does not predict the osmotic flow observed in our simulations at later times.

Chapter 7

Osmosis in a Non-Equilibrium Active System

Osmosis plays an important role in almost every soft matter and biological system, including those containing active particles such as motile micro-organisms, synthetic swimmers or hot nanoparticles – which are attracting increasing attention in the soft matter physics community. Yet little is known about the basic physics of osmosis in active systems where, because the system is far from equilibrium, the laws of thermodynamics no longer apply. In this chapter we extend our study of osmosis to include systems which are driven out-of-equilibrium by the introduction of active solute particles. Before we begin our study of active osmosis a short review of the relevant active matter literature is presented.

7.1 Active matter and osmosis

7.1.1 Active matter in a biological context

For much of their 3.8 billion year existence, microbial organisms similar to today's *E. coli* are likely to have propelled themselves along using light or ingested nutrients as their energy source. However, until the last century or so, little was known about this propulsion. Pfeffer (who also studied osmosis; see Section 1.1) conducted some of the earliest studies into bacterial chemotaxis [115]. However, it was not until more recently that the mechanism that bacteria use to propel themselves, by rotating their flagella, was elucidated. This elaborate form of motion breaks time reversal symmetry;

a necessary condition (Purcell [125]) that swimmers in a low Reynold's number[1] fluid must satisfy in order that they propel themselves forwards.

It has since become clear that swimming organisms can bring about interesting and nontrivial effects in the behaviour of the surrounding fluid. For example, Wu and Libchaber [169] recorded the collective effects that a colony of swimming bacteria can exert on a collection of micron-scale beads in a freely suspended (quasi-two-dimensional) soap film. A transition in the beads' dynamics was observed between super-diffusive motion at short times and diffusive motion at later times.

The fact that motile bacteria are similar in size to colloidal particles naturally leads to the question of whether manmade micro or nanoscale swimming particles might be artificially synthesised to perform complex tasks, for example as nanomachines [49, 71] or microswimmers for drug delivery [148].

7.1.2 Artificially produced active particles

Purcell discussed in his seminal work "Life at Low Reynold's Number" [125] a hypothetical framework for a model manmade swimmer consisting of two hinges, similar to "a boat with a rudder at both front and back". However, working out the exact details and deriving analytical results for such a swimmer were, due to the complications of solving the Stokes equation ($-\nabla P + \eta \nabla^2 \vec{v} = 0$), anything but simple. Golestanian and Najafi [50] considered, in 2004, a simpler model for a swimmer, based on the work of Purcell, consisting of three spheres connected by two rigid slender arms, see Figure 7.1(a). As reasoned by Purcell, for the swimmer to propel itself forwards, it must perform a cyclical motion which breaks time-reversal symmetry. Several other model swimmers, similar to the three-sphere system, have since been proposed, including a dumbbell whose swimming strokes are out of phase with one another [3]. When arranged collectively, the authors speculate that these swimmers may have applications as micropump devices. However, none of the above mentioned swimmers has been experimentally realised.

Janus particles[2], active colloids which have two distinct faces (see Figure 7.1(b)), have, however, been successfully produced experimentally. In [65], micron sized polystyrene

[1] The Reynolds number, a dimensionless quantity defined as $Re = \frac{a v \rho}{\eta}$, in which a is the size of the object, v its velocity, and ρ and η are the density and viscosity of the medium in which the object is suspended, relates the viscous forces on a body to its inertial forces.

[2] The first reference to the term Janus appears to be in [45], where de Gennes discusses Janus grains which have two sides, one apolar and the other polar.

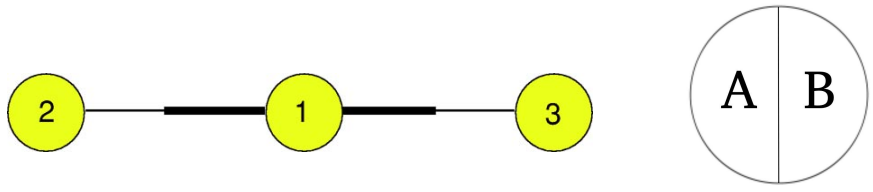

(a) (b)

Figure 7.1 Panel (a): Diagram of a proposed Low Reynolds number swimmer, taken from [50]. Three linked spheres are connected by two arms, for which part of the arm is of fixed length (thick line) and part is of variable length (thin line). Panel (b): Schematic of a Janus particle. A silica/polystyrene sphere is coated on one side (A) with a reactive material, such as platinum for a hydrogen peroxide powered colloid or gold for a laser powered colloid, and the other side (B) is left uncoated. The asymmetry in the colloid results in its elevated Brownian motion through the hydrogen peroxide/laser heated solution.

spheres were coated on one side with platinum and placed in a hydrogen peroxide solution. Using this particular setup, the platinum surface subsequently catalyses the dissociation of hydrogen peroxide to hydrogen and oxygen, producing an asymmetric jet of bubbles which propels the particles in a particular direction. The directed motion is eventually randomised due to Brownian fluctuations. More recently [36], Janus doublets have been formed; particles which are capable of performing an autonomous run and tumble motion, similar to bacteria. Bimetalic nanorods, where one end is coated in platinum and the other in gold, have also been synthesised[3] [114]. And, a different variant of Janus particles, in which one half of a microsphere is coated in gold, can be made active following the application of a defocused laser beam to the system [68].

In addition to Janus particles, active nanoparticles have also been studied [18, 99, 129, 133, 134]. Here one does not necessarily attempt to achieve directed motion through the solution, instead the nanoparticle is heated (using a laser beam for example) such that it moves like a "hot" Brownian particle. In a simulation study, Merabia *et al.* [99] found that gold nanoparticles immersed in octane can decompose into individual metal atoms or small clusters, causing only a minimal disturbance to the surrounding medium. Experimentally, the dynamics of gold coated nanoparticles have been studied in water and glycerol/water mixtures by Radunz *et al.* [129]. In this work, a new spectroscopic method, Photothermal Correlation Spectroscopy (PhoCS), which measures the temperature gradient in the surrounding solvent as a result of the active motion of the nanoparticle, was developed as an alternative to fluorescence correlation spectroscopy (FCS), a technique which requires fluorescent tracers and expensive single

[3] When placed in a hydrogen peroxide solution, the nanorods display similar behaviour to the Janus spheres.

photon counting hardware to achieve single particle sensitivity.

Recently, a great deal of work has focused on studying the collective motion of these self-propelled colloidal particles. Theurkauff *et al.* have reported [153] the clustering of spherical, platinum covered Janus particles with increasing Peclet number[4]. In the case of geometrically confined active colloids, Golestanian [47] has derived analytical expressions demonstrating that thermorepulsive colloids (*i.e.* ones whose Soret coefficient (S_T) is positive – S_T = the ratio of thermal to regular diffusion) can organise into hollow bands, tubes or shells. Meanwhile, for thermoattractive colloids ($S_T < 0$), the colloids organise into ever larger clusters as the extent of the thermoattraction increases; above a critical attraction, the cluster becomes unstable in "an analogous manner to a supernova". McCandlish *et al.* [95] have studied self-propelled rod-like particles using Brownian dynamics simulations in a 2D plane, demonstrating that activity can drive the rods to segregate into various patterns. And, inspired by living organisms such as birds and fish, Mishra *et al.* [100] studied the flocking of self-propelled particles into striped regions of high and low particle density. Thus, active colloids and Janus particles have been shown to demonstrate interesting dynamical behaviour. However, the influence that the active component of such systems has on the passive component, the solvent for example, has not received as much attention. This is the subject of the work presented in this chapter.

7.1.3 Active suspensions and osmotic effects

Recently, attention has turned to the importance of studying osmotic effects in active systems. Brady and Córdova-Figueroa have proposed a hypothetical osmotic motor in which reactions taking place on the surface of a colloid generate a non-uniform distribution of solute particles in the solution [25]. This in turn generates an osmotic force, resulting in the colloidal particle's directed motion through its surroundings. An analytical derivation for the osmotic force is subsequently used to demonstrate that the ratio of the reactants to the products diffusion constants (D_R/D_P) is the dominant factor in controlling the dynamics of the motor.

Valeriani *et al.* [159] have used MC simulations to study how osmotic effects might drive the motion of a colloidal "chucker". In their work, the colloidal "chucker" is driven through the solution by the secretion of solute particles at its surface which, in

[4]The Peclet number ($= va/D_0$, where v is the particle's velocity, a its radius and D_0 a so-called "bare-diffusion coefficient") is a measure of the ratio of heat transport by convection to heat transport by conduction.

turn, generates a force on the colloid, moving it down the concentration gradient of solute particles in the system. Another study [48] has reported that, if the colloidal particle is made permeable to the solvent species, then it may undergo an even faster motion through the solution.

Osmotic effects have also been shown to play a key role in biologically occurring active processes. In a recent study [141], the spreading of bacterial biofilms was shown to be reliant on the secretion of exopolysaccharide, which generated osmotic pressure gradients in the extracellular matrix, driving the surface motility of the cell. Furthermore, lipid vesicles have also been shown to become active in the presence of osmotic gradients, moving down the solute concentration profile [106].

In all of the studies discussed, osmotic effects were used to drive the active motion of the colloidal particles. In this chapter, however, we take a slightly different approach by considering systems in which the solute particles themselves are active. In particular, we focus on how the solutes' activity affects the osmotic pressure and density gradients in the system. However, the results presented herein may be applicable in systems which do not contain a dividing membrane, for example where a depletion interaction exists [117, 171] (in which colloidal particles experience an attractive force due to the exclusion of polymer molecules from their surface), or in describing the collective motion of active solutions.

7.1.4 The concept of an effective temperature for active systems

Systems which contain active particles are intrinsically out-of-equilibrium, thus thermodynamic concepts such as the temperature of the system are no longer valid. To overcome this "problem" the concept of an effective temperature, which maps the non-equilibrium system onto an equivalent equilibrium one, has been proposed. Since I discuss this concept later on in the chapter, I briefly introduce it here.

In equilibrium thermodynamics, the fluctuation-dissipation relation (FDR) connects equilibrium fluctuations to perturbations of the system in the presence of some external field. It can be written down as follows [86]:

$$\chi(t_1, t_2) = \frac{1}{k_B T} \left[C(t_1, t_1) - C(t_1, t_2) \right], \tag{7.1}$$

where C represents the correlation between two observables ($C(t_1, t_2) = \langle O_1(t_1) O_2(t_2) \rangle$),

χ is the linear response to a perturbation, and k_BT is Boltzmann's constant times the temperature of the system. By analogy with Eq.(7.1) we can define an effective temperature for a non-equilibrium system as

$$1/T_{eff}(C) = -d\chi(C)/dC. \tag{7.2}$$

The effective temperature in Eq.(7.2) therefore relates the response to a perturbation to the magnitude of the fluctuations in the absence of this perturbation for a non-equilibrium system. In Figure 7.2(a) results (taken from [27]) are shown for a simulation of 500 particles which interact via a Lennard Jones-like potential and in which some fraction of the particles are coupled to a motor force. The relationship between χ and C is, in this case, indeed linear, supporting the notion that the effective temperature is a meaningful quantity.

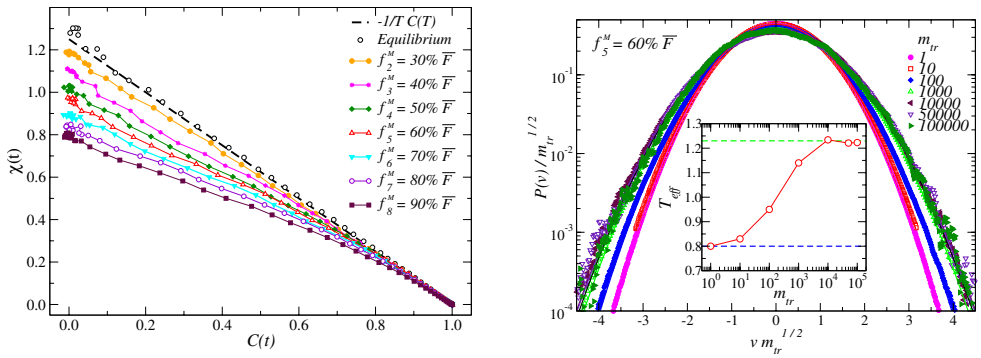

(a) **(b)**

Figure 7.2 Panel (a): The time dependent response [27] to a perturbation $\chi(t)$ is plotted versus the correlation function C(t) for increasingly active suspensions (see legend). The effective temperature is then obtained as the negative reciprocal of the gradient. Panel (b): The velocity distribution for a tracer particle has been plotted [27] for increasingly massive tracer particles (see legend). The inset then shows the results for the effective temperature (obtained from fitting a Maxwell-Boltzmann distribution to the velocity profile) as a function of the tracer particle's mass.

The FDR is not the only way to define an effective temperature, however. An alternative definition for T_{eff} is illustrated in Figure 7.2(b) for the self same system described above. However, in these simulations a massive tracer particle[5], which only interacts with the active particles, has also been included. By matching the velocity distribution for the tracer particle to an equivalent (equilibrium) Maxwell-Boltzmann distribution, the effective temperature of the active particles can thus be inferred.

[5]Its being massive allows for a long internal time scale ($t \sim m^{1/2}$) that captures the long time dynamics of the system instead of simply capturing the fast dynamics of the surrounding bath.

Two other ways to define an effective temperature have been suggested by Joly *et al.* [69]. Firstly, one can define a kinetic temperature, T_K, related to the centre-of-mass velocity of the active particle as $\frac{1}{2}k_B T_K = \frac{1}{2}m\left\langle U_\alpha^2 \right\rangle$, where U_α is the relative velocity between the active particle and the surrounding liquid (in the α direction). This is similar to the method of matching velocity distributions described above, except this method does not make use of a tracer particle to determine the effective temperature of the active particles. Secondly, the "Einstein" temperature (which is related to the FDR), T_E, can be defined as the ratio between the diffusion coefficient, D, and the mobility of the active particle, μ; see Section 2.2.2 for more information on the diffusion coefficient and its calculation. Joly *et al.* measure D using the velocity autocorrelation function and the mobility is measured by applying a constant force to the particle and measuring its velocity in the direction of the force: $\mu = U/F$. In Section 7.4 we will return to these concepts and consider the possibility of defining yet another effective temperature, which we term the osmotic effective temperature.

7.1.5 Chapter outline

Despite the widespread interest in active colloidal systems, to date there exists no systematic investigation into the underlying behaviour of a simple, active osmotic system. This is the objective of this chapter.

I first outline a minimal model to study the basic physics of osmosis in a system containing active solute particles. Two types of active solute particles are studied; these are referred to as "hot solutes" and "swimming solutes" respectively. The osmotic pressure in the system is then measured for several solute activities. At low solute concentrations, the osmotic pressure is, for all of the activities studied, linear. This leads us to the possibility of defining a new osmotic effective temperature, the results of which are compared to the diffusive and kinetic temperature of the solute particles. We also discover an unexpected phenomenon: under some circumstances, active solutes can lead to reverse osmosis. Results for this behaviour in the minimal model are presented and reconciled using radial distribution functions which point to the solvent experiencing an increased "effective density" in the active solution. In the discussion section the relevance of these results to experimental systems is explored and the possibility that an osmotic setup be used for measuring the active component of the stress tensor is considered.

7.2 A minimal model for active osmosis

7.2.1 Simulation overview

As in Chapter 5, the simulations described in this chapter use the box in box, invisible membrane. This setup is described in detail in Chapter 3, Section 3.2.2, thus here I only briefly review the key features of the simulation setup.

A solution compartment, containing both solute and solvent particles, is immersed in a solvent bath, containing only solvent particles (a schematic of the setup is given in Chapters 3 and 5). The solvent and solute particles interact indistinguishably with one another via a WCA interaction (see Section 3.2.1) and there are no solvent-membrane interactions. The solute particles, however, remain in the solution compartment for the duration of the simulations using the steep confining potential outlined in Section 3.2.2. In the absence of activity (as we saw in Chapter 5) this setup results in the net flux of solvent particles into the solution compartment prior to the steady state. Here, we are interested only in the steady-state properties of the system and so the simulations are allowed to thoroughly equilibrate for 100 reduced time units; for a ballistic particle at temperature $T = 1$ this corresponds to approximately 9.5 times the length of the simulation box[6]. A further 3600 reduced time units of equilibrated data are then collected.

As in previous chapters, the parameters σ, ϵ, and m, corresponding to the size of the particles, their interaction energy and their mass, are set equal to one. In all of the simulations, a total of 5000 particles (solvent + solute) are placed in the cubic simulation box, of length $L = 18.42\sigma$, such that the resulting overall particle density is $\rho_{total} = 0.8\ \sigma^{-3}$ (thus, the packing fraction $\pi\sigma^3\rho_{\text{total}}/6 = 0.42$). Positions and velocities are propagated using a velocity Verlet algorithm in combination with a Nosé-Hoover thermostat and a timestep $\Delta t = 0.0005$. The results for the osmotic density gradients and pressure have been reproduced using both an Andersen thermostat and, also, a Nosé-Hoover Langevin thermostat (see Section 2.1.3 for a description of these thermostats). In all of the simulations presented in this chapter, the osmotic pressure is computed as the solute-wall force per unit area, based on the confining potential described above. As in Chapter 5, the solution volume is defined using the method outlined in Section 3.2.2, where the shift along the $x - axis$ necessary to match the pressure-density relation for a confined gas of solute particles to that of a periodic solute

[6]Where we have used the equipartition theorem to relate the temperature of a particle to its velocity, $v = \sqrt{3k_BT/m}$.

gas determines the effective boundary on the solution compartment.

7.2.2 Two models for active solutes

The key difference in the simulations presented here to those presented in Chapter 5 is the introduction of active solutes. This is achieved using two different setups: "hot solutes" and "swimming solutes". We use two different models for the active solutes to ensure that the conclusions we draw are general and not simply a result of having studied a particular type of solute particle. A schematic illustrating the two alternative models is given in Figure 7.3.

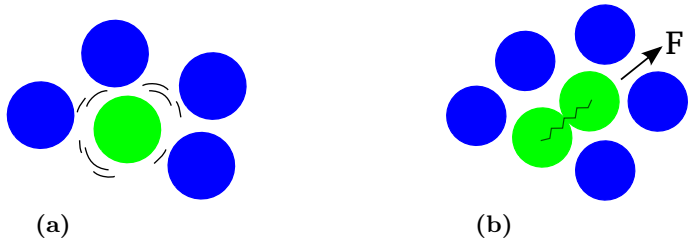

Figure 7.3 Sketch illustrating the active solute setups used in this chapter. Panel (a) illustrates a "hot solute" particle (in green) surrounded by the solvent bath (in blue). In panel (b) pairs of particles are bound together into dumbbell particles (in green) by a FENE spring potential and made active through the application of a force (F) along the long axis of the dumbbell. For further details of these setups see the main text.

Hot solutes

The hot solutes scenario is conceived as a minimal model for the effects of injecting internal energy into an osmotic system. It is inspired by the work outlined above on active nanoparticles. In this scenario the solute particles are coupled to a separate thermostat that maintains them at a higher temperature than the solvent particles, *i.e.* we impose the condition $T_u > T_v$, where T_u denotes the solute temperature and T_v the solvent temperature[7]. A flow of energy is thus established: the solute thermostat imparts energy to the solute particles, speeding them up, this energy is transferred to the solvent particles through solute-solvent collisions and the energy is finally removed from the system through the solvent thermostat.

Because the particles are rather strongly coupled to their respective thermostat,

[7]Results for "cold" solute particles are also presented in Sections 7.3 and 7.5, in which the solutes are coupled to a separate, lower temperature thermostat than the solvent particles.

Maxwell-Boltzmann-like velocity distributions are obtained for both sets of particles, see Figure 7.4(a). In the inset to Figure 7.4(a) the tail of the solvent velocity distribution does, however, appear to deviate slightly (red data) from that of the purely passive system (black data) in the presence of the active solutes – thus demonstrating the dissipation of heat between the active solutes and the passive solvent particles. In reality this effect would be much larger [68] and we would observe broader temperature gradients around the solute particles. However, in this work we are interested in dealing with an idealised scenario. Also note that the results presented later on in the chapter have been reproduced using both an Andersen and a Nosé-Hoover Langevin thermostat, so they are not symptomatic of any particular choice of thermostat.

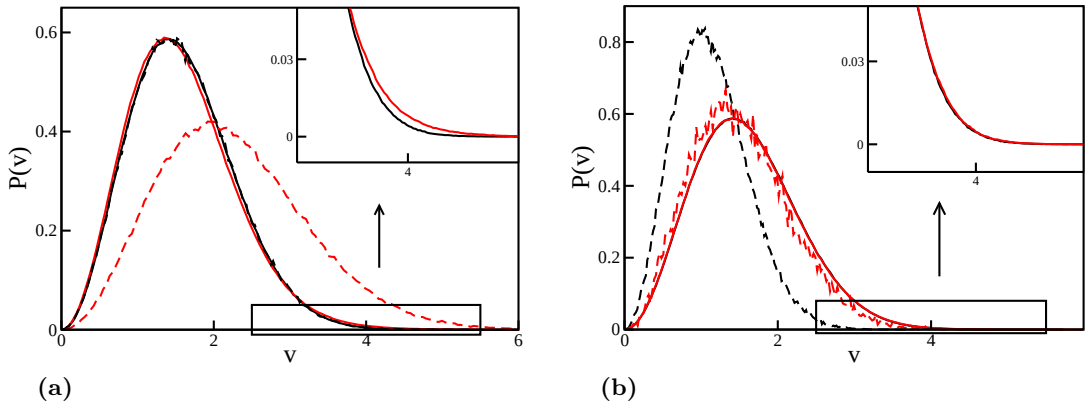

Figure 7.4 Velocity distribution for the hot solutes and swimming solutes. In panel (a) the velocity distribution for the hot solutes is shown by the dashed lines and the solvent velocity distribution is shown by the solid lines, in black (for $T_u = T_v = 1.0$) and in red (for $T_u = 2T_v = 2.0$). In the inset to (a) the slight heating of the solvent particles, for the case that the solutes are active, is shown by a sight broadening in the tail of the solvents' velocity distribution. In panel (b) the same results are plotted for the centre-of-mass velocity of the dumbbell particles and the surrounding solvent, for $F = 0.0$ and $F = 6.0$ ($T_v = 1.0$ in both instances).

Swimming solutes

As an alternative to the hot solutes, swimming solutes have also been considered. The inspiration for using this model comes both from studies of motile bacteria, as discussed in Section 7.1.1, and the Golestanian swimmers work discussed in Section 7.1.2. The model we use is similar to that discussed in [160], in which a solute particle is represented by a dumbbell swimmer. Here we study pairs of particles bound together by a FENE spring [164]. The FENE spring (Finitely Extensible Nonlinear Elastic model) potential takes the form

$$U_{FENE} = \begin{cases} U_{WCA} - \frac{\kappa}{2} R_0^2 \log\left[1 - \left(\frac{r}{R_0}\right)^2\right] & \text{if } r < R_0 \ , \\ \infty & \text{otherwise} \ , \end{cases} \tag{7.3}$$

where U_{WCA} is the usual WCA potential, κ is the spring constant (set = 30.0 here) and R_0 is the maximum extension of the spring (set = 1.5 σ here). Using these values results in a typical bond length of 0.96 σ. The dumbbells are propelled through the solutions by an external force F that acts along the long axis of the dumbbell. The centre-of-mass velocity distribution for the dumbbells is shown in Figure 7.4(b). Although they are not directly thermostatted, the surrounding solvent acts as a thermostat, resulting in Maxwell-Boltzmann-like velocity distributions for the dumbbells. For passive dumbbells (black dashed line in Figure 7.4(b)), the velocity distribution is well represented by a Maxwell-Boltzmann velocity distribution at temperature $T = 1.0$. When the dumbbells are made active (red dashed line in Figure 7.4(b)), the velocity distribution is shifted, but can nevertheless be mapped to a higher temperature Maxwell-Boltzmann distribution. The solvent particles' velocity distribution, on the other hand, shows only a slight variance in comparison to that observed for the hot solutes, see insets to Figures 7.4(a) and (b). The consequences of this on the effective temperature in our simulations will be further discussed in Section 7.4.

7.3 The osmotic pressure of active solutions

The first results I present in this chapter explore how the osmotic pressure in the solution, ΔP, is affected by the solute particles' activity. The van 't Hoff relation, discussed in Chapter 1, states that, in dilute (*i.e.* when the solute concentration is low) equilibrium solutions, the osmotic pressure is linearly proportional to the concentration of solute particles, c_u. In Chapter 5 we saw that the results of passive simulations are consistent with this relation up to solute concentrations, $c_u \sim 0.1\ \sigma^{-3}$, before virial corrections must be included to account for deviations from the van 't Hoff law. Although the systems studied in this chapter are driven out-of-equilibrium, we expect that, as in the passive simulations, the resulting osmotic pressure will be well represented by a linear relationship at low solute concentrations; however, the constant of proportionality may be different from the passive case. In Figure 7.5 we see that this is indeed the case in our simulations. For both the hot solutes and the swimming solutes, the passive case (black circles; $T_u = T_v$ for the hot solutes and $F = 0$ for the swimming solutes) is in good agreement with the van 't Hoff relation (solid black line) at

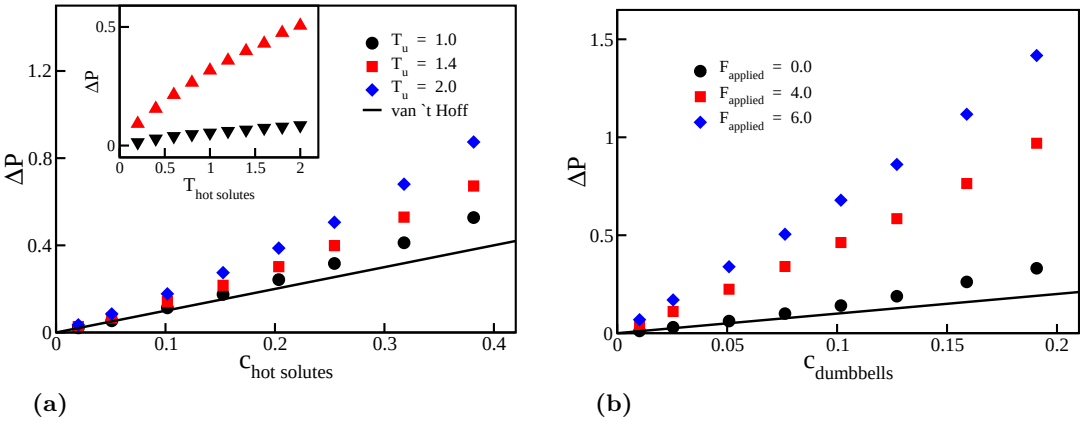

Figure 7.5 Osmotic pressure (measured using the solute-wall force method, see Section 3.2.3) versus the concentration of impermeant species in the solution, for (a) the hot solute system and (b) the swimming solutes system. For each system results are shown for both the passive, equilibrium case (black circles) and for two fixed activities (red squares and blue diamonds). In the passive case, the solute particles are either thermostatted at the same temperature as the solvent, or the force applied along the axis connecting the swimmers is set equal to zero. In panel (b) the dumbbell concentration is shown on the $x-axis$, therefore the actual concentration of solute particles is twice this value as there are two solute particles per dumbbell. In all of the simulations the solvent is thermostatted at $T_v = 1.0$. Similar errors in the solute concentration to those presented in Figure 5.4 apply here. The errors in the measured osmotic pressure are smaller than the symbols.

low concentrations. As the activity of the solutes is increased, the slope in the osmotic pressure versus solute concentration relation remains linear. However, the gradient of the slope increases as the solutes become more active, leading to more rapid deviations from the law of van 't Hoff. Since the constant of proportionality in the gradient of the osmotic pressure versus solute concentration relation was equal to k_BT in our passive simulations, it is natural to define an effective temperature for the active simulations from this same relation in those regions where the osmotic pressure relation remains linear.

7.4 The osmotic effective temperature

The concept of an effective temperature was introduced earlier on in this chapter as a means to map the complex behaviour of non-equilibrium systems onto the better-understood properties of equilibrium systems. The results presented in Figure 7.5 suggest that a new, osmotic temperature T_{eff}^{os} might be defined by mapping the osmotic pressure-solute concentration relation onto a van 't Hoff-like form, $\Delta P = k_B T_{eff}^{os} c_s$, for dilute solutions.

In Figure 7.6 we plot the osmotic effective temperature over several solute activities. As one would expect, it increases with the thermostat temperature for the hot solutes and, in the swimming solutes model, it increases with the swimming force F. It is interesting to compare the osmotic effective temperature with with other measures for the effective temperature of active particles. Here we consider the two effective temperatures defined by Joly *et al.* – the diffusive temperature and the kinetic temperature.

The diffusive temperature is defined using the Einstein relation, $D = \mu k_B T$, where D is the diffusion coefficient and μ is the mobility of the solute particles. Thus, by taking the ratio between the diffusion coefficient in the active case to that measured in the passive case we can determine the diffusive effective temperature of the particles: $T_{eff}^{d} = D_{act} T_{pass} / D_{pass}$. The diffusion coefficients are computed by measuring the mean square displacements of the particles as a function of time; as discussed in Section 2.2.2. The second temperature we consider, the kinetic temperature, is defined using the centre-of-mass velocity of the active solute particles, $\bar{v}$. This is related to the kinetic effective temperature by the relation $\frac{1}{2}\sum_i m_i \bar{v}_i^2 = \frac{3}{2} N k_B T_{eff}^{k}$, where the sum runs over all N hot solutes/dumbbells and m_i is the mass of the i^{th} hot solute/dumbbell particle.

The results in Figure 7.6 demonstrate that, for both setups, T_{eff}^{os} is in good agreement with the diffusive temperature T_{eff}^{d} over a wide range of activities (T_u or F). For the hot solutes simulations, the kinetic temperature T_{eff}^{k} is also in good agreement with both the diffusive and osmotic temperatures; however, for the swimming solutes this is no longer true. Instead, the kinetic temperature is somewhat lower than the diffusive and osmotic effective temperatures. This may be an indication that the kinetic temperature captures the fast dynamics which the surrounding solvent experience (close to the equilibrium FDT), equivalent to the temperature as $C(t)$ approaches one in Figure 7.2(a), whereas the osmotic and diffusive temperatures describe the dynamics corresponding to long time differences in Figure 7.2(a), as $C(t) \to 0$.

At first sight, the apparently good agreement between the diffusive and osmotic effective temperatures suggest that the behaviour of the non-equilibrium osmotic systems might be well represented by mapping to an equivalent equilibrium system. It turns out, however, that this is not the case. Whilst the effective temperature description can capture the osmotic pressure in our simulations, as we shall see in the next section, it fails to reproduce the steady-state density imbalance that is established between the solution and the solvent bath in the presence of active solutes.

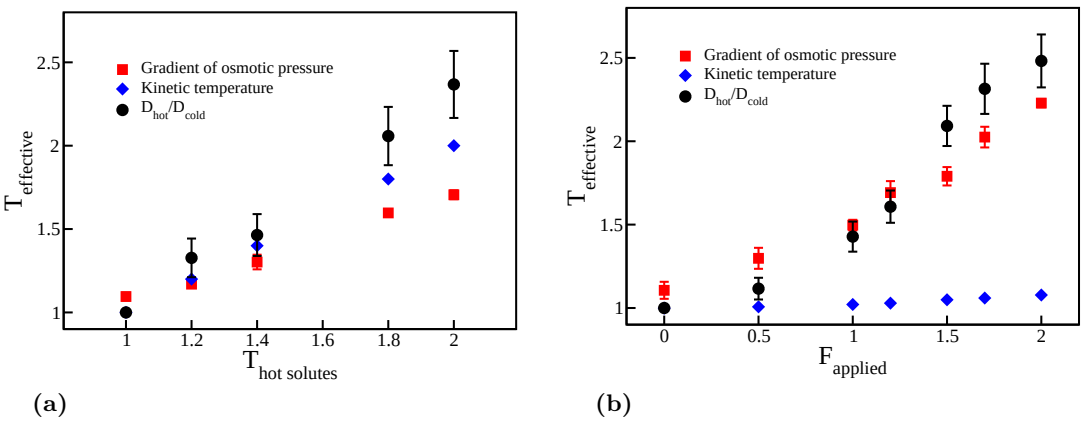

Figure 7.6 Three different methods for measuring temperature are shown as a function of increasing particle activity for (a) the hot solute particles and (b) the swimming solutes. In the figures, the circles show diffusive temperatures, the squares osmotic temperatures and the diamonds the kinetic temperatures.

7.5 Reverse osmosis due to active solutes

In Chapter 5 our simulations of equilibrium osmosis reproduced the well-known result for the steady-state density of particles across the membrane; that is a *higher* total density of particles in the solution compartment compared to the solvent bath. In Figure 7.7 results for the total density profiles are shown for simulations of osmosis, in panel (a) using hot solute particles and in panel (b) using swimming solutes (dumbbells). The black lines shows the results of passive simulations (*i.e.* when the solute activity is set to zero) and the red lines show the results for active solutes. Here, we see that the active simulations exhibit qualitatively different behaviour from the passive systems. In both of the simulation models for active particles, as the activity increases, the total density of particles in the solution compartment decreases, so that the steady-state total density of particles in the solution is now *lower* than in the solvent bath. Thus, the addition of active solutes on one side of the semi-permeable membrane causes solvent particles to be displaced out of the solution compartment (relative to the uniformly distributed case $\rho = 0.8\ \sigma^{-3}$) – in contrast to the equilibrium osmotic situation, where solvent particles are displaced into the solution. Active solutes, therefore, can induce reverse osmosis.

This qualitative behaviour is reproduced over a range of activities and solute concentrations in Figure 7.8. In Figure 7.8(a) an increase in the hot solutes' temperature causes a decrease in the total density difference across the membrane, until eventually the solvent particles begin to move out of the solution compartment prior to the steady

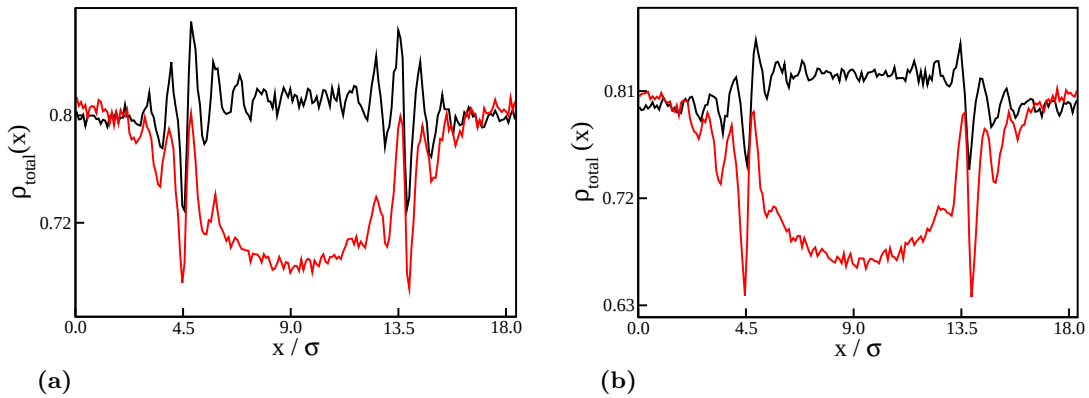

Figure 7.7 Steady-state total density profiles are shown for osmosis simulations using the hot solutes (panel (a)) and the swimming solutes (panel (b)). In panel (a) the simulation contained 200 solute particles, thermostatted at a temperature $T_u = T_v$ (black line) and $T_u = 2.0T_v$ (red line). For the swimming solutes, shown in panel (b), the simulations contained 100 dumbbells and forces $F = 0$ (black line) and $F = 6$ (red line) were applied.

state instead of being drawn into it. A similar behaviour is also observed for the swimming solutes, see Figure 7.8(b).

In the insets to Figures 7.8(a) and (b) the variation in the steady-state total density difference is plotted as a function of the concentration of active particles. In the equilibrium, passive case (black data in the insets), we observe a steady increase in the density difference across the membrane as the concentration of solute particles is increased. As the solute particles are made active (red and blue data in the insets), the density difference in the dilute solutions steadily decreases with increasing solute concentration, producing the aforementioned reverse osmosis ($\Delta\rho_{tot} < 0$) in our simulations. Although we observe reverse osmosis over the whole range of solute concentrations tested here, it is apparent that for very high solute concentrations the amount of reverse osmosis starts to decrease (*i.e.* there is a minimum in the plot of $\Delta\rho_{tot}$ versus solute concentration).

That the active systems studied here demonstrate reverse osmosis is clearly something that cannot be reconciled with the notion of an effective temperature, because simulating an equivalent passive system at an elevated temperature would not result in reverse osmosis – indeed it would result in the opposite effect. Therefore, it appears that qualitatively different physics to that occurring in the passive system is needed to explain this phenomenon. Motivated by this observation, we therefore attempt to construct a simple model that explains the reverse osmosis results illustrated here, and which also captures the non-trivial dependence on the solute concentration shown in the insets to Figures 7.8(a) and (b).

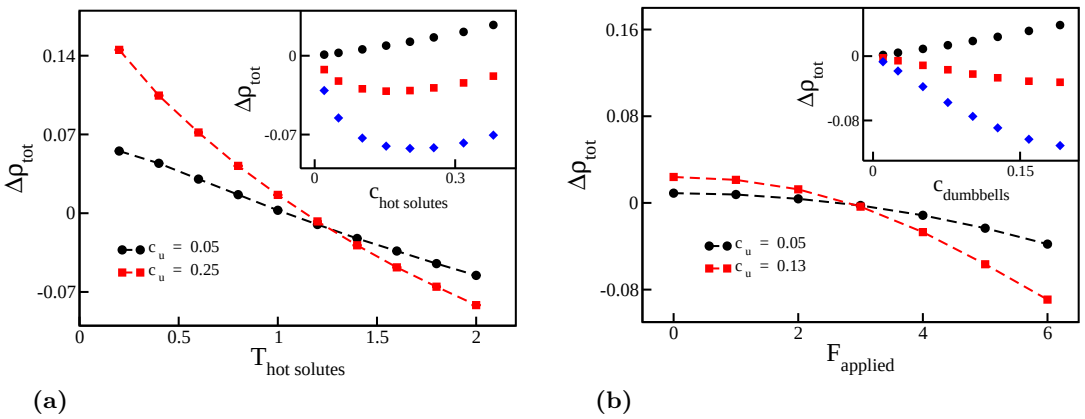

Figure 7.8 The steady-state difference in the total density of particles in the solution compartment and the surrounding bath ($\Delta\rho_{tot} = \rho_{solution} - \rho_{bath}$) is shown as a function of the activity of the hot solutes/swimming solutes and (in the insets) as a function of the concentration of the hot solutes/swimming solutes. (a): $\Delta\rho_{tot}$ is plotted as a function of the hot solutes' temperature. Results are shown for two different concentrations, $c_u = 0.05\ \sigma^{-3}$ and $c_u = 0.25\ \sigma^{-3}$, by the black circles and the red squares, respectively. At high enough activities the density imbalance becomes negative meaning that the introduction of active solutes leads to solvent being expelled from the solution. In the inset the density imbalance is shown as a function of the hot solutes' concentration for three different activities – for the black circles $T_u = T_v$, for the red squares $T_u = 1.4T_v$ and for the blue diamonds $T_u = 2.0T_v$. (b): $\Delta\rho_{tot}$ is shown for the swimming solutes as a function of the force for dumbbell concentrations of $c_u = 0.05\ \sigma^{-3}$ (black circles) and $c_u = 0.13\ \sigma^{-3}$ (red squares). As in panel (a) the inset shows the density imbalance as a function of the concentration of the active particles. Results are shown for $F = 0$ (black circles), $F = 4$ (red squares) and $F = 6$ (blue diamonds). The error bars in the data are smaller than the symbols.

7.6 A collision dynamics model for non-equilibrium osmosis

Based on the hopping model outlined in Chapter 5, an initial attempt at explaining the above results was made using a simple model in which particles on either side of the membrane collide, exchanging momentum as they do so. To this end, a series of idealised two body elastic collisions between particles located on either side of the membrane were simulated, as in Figure 7.9. In doing so, we hypothesise that the transfer of momentum occurring during these collisions might account for the reverse osmosis in our simulations. This is a plausible explanation because, on average, particles inside the solution have a greater kinetic energy than those in the bath (due to the solutes' activity). Therefore, the particle collisions produce a net transfer of momentum out of the solution compartment which should be balanced in the steady state by reducing the density of particles in the solution.

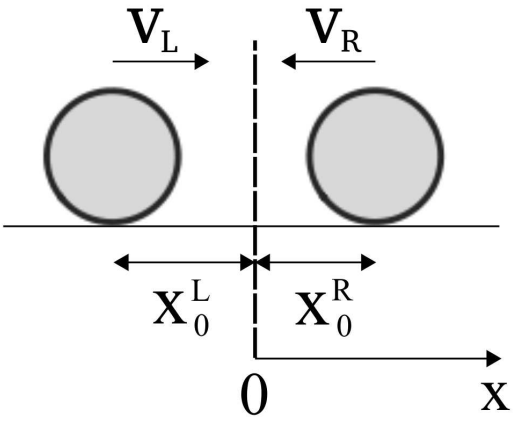

Figure 7.9 Diagram illustrating a head-to-head elastic collision between two particles. In this scenario the particle on the right has a velocity directed towards the left compartment and the the particle on the left has its velocity directed towards the right compartment. Thus, given a sufficient time window, the two particles will collide, swap velocities and subsequently move away from one another.

Our simulations of this highly simplified one-dimensional model proceed as follows. We first specify the density of particles on either side of the membrane. Given this choice, the initial positions of two particles, one on either side of the membrane, are chosen from the following distribution, $p(x_0) = \rho e^{-\rho x_0}$, where x_0 is the initial position and ρ is the density on the left/right hand side of the membrane. The velocities of the two particles are subsequently chosen according to the 1D Maxwell-Boltzmann distribution specified in Eq.(2.4), where the temperature T is set equal to one if the particle is a solvent and $T \geq 1$ if the particle is a solute. Solute particles are chosen on the solution side of the membrane with probability, $p = n_u/n_{solution}$, where n_u is the number of solute particles and $n_{solution}$ is the number of particles in the solution. The positions of the particles are then propagated forward for some time t according to the following relation: $x(t) = x_0 + vt$. From this we can compute the net flux of particles across the membrane due to collisions. Three possible scenarios are possible. In the first instance, the particles may have velocities in opposite directions, in which case they both move away from one another and there is no transfer of momentum across the membrane. Secondly, their velocities may be in the same direction. In this scenario, they may or may not, therefore, collide with one another, depending on whether the time frame t is long enough. If a collision occurs, the particles swap velocities[8] and subsequently transfer momentum across the membrane. Finally, the particles may have velocities directed towards one another, in which case, provided the time frame t is long enough, they will collide, swap velocities and subsequently fly apart (as in Figure 7.9). If the

[8]The exchange of particle velocities is a standard result in elastic collisions.

particle in the solution compartment is chosen to be a solute, it is not allowed to cross the membrane and, in the instance that its projected position crosses the membrane, it performs an elastic collision with the membrane, reversing its velocity as it does so. The osmotic pressure is calculated from summing the momentum flux across the membrane upon solute particle collisions.

This procedure is repeated many times to obtain the average net flux of solvent particles across the membrane for a given choice of particle densities on the left and right hand side of the membrane. By adjusting the density imbalance across the membrane we can determine the steady-state density imbalance – *i.e.* the solvent densities on either side of the membrane that produce zero net flux.

The results from our simulations of this simple model are shown in Figure 7.10. For a passive osmotic system, in which we set the temperatures of the solvent and solute particles to be equal ($T_u = T_v = 1.0$), the results qualitatively follow those expected of an osmotic system. Firstly, the osmotic pressure, shown by the black data in Figure 7.10(a) for a system at overall density $\rho = 0.5$, varies linearly with increasing solute concentration, and, secondly, the density difference across the membrane increases (semi-) linearly with increasing solute concentration (see black data points in Figure 7.10(b)).

Figure 7.10 also shows the results of this simple toy model for active solutes – *i.e.* when

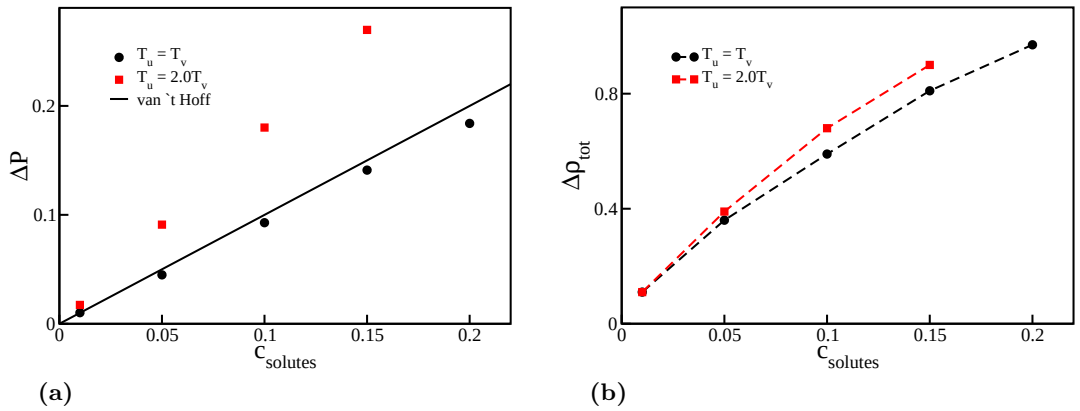

Figure 7.10 Results of collision dynamics simulations for the osmotic pressure and density imbalance across the membrane using both passive and active solute particles. In panel (a) results for the osmotic pressure of the passive (black circles) and active (red squares) 1D collision dynamics simulations are shown. For the active simulations the solute velocities were chosen from a higher temperature MB distribution, such that $T_u = 2.0T_v$. In panel (b) results are shown for the steady-state density imbalance in the same passive (black circles) and active (red squares) simulations for the simple toy model.

the solute particle velocities are chosen from a higher temperature MB distribution to those of the solvent. The red data in Figure 7.10(a) demonstrate that the osmotic pressure is higher in our active simulations and that it still increases linearly with the solute concentration. These results are in agreement with our MD simulations of the full, many particle system, as shown in Figure 7.5. The density imbalance, however, does not behave as in our MD simulations (see Figure 7.10(b)). Instead we observe a net positive $\Delta\rho_{tot}$, rather than the negative $\Delta\rho_{tot}$ observed in our MD simulations, see Figure 7.8. In fact, for this toy model, active solutes actually slightly increase the density of particles on the solution side of the membrane. Thus, reverse osmosis is not captured by a simple one dimensional simulation model of elastic collisions.

Upon closer examination of the fluxes into and out of each of the compartments, it was discovered that the reason for this is related to the second scenario outlined above, when the velocities of the two particles are in the same direction. More specifically when both velocities are directed into the solution compartment. If the solutes' activity is increased then, provided a solute particle is specified in the solution, it will more often create a "vacuum" into which the solvent crossing the membrane can move. This actually facilitates the solvent flow *into* the solution, rather than pushing solvent out. The presence of active solutes does, however, also increase the rejection rate for solvent particles entering the solution compartment – consider the case that the particle velocities are directed towards one another, in a head-to-head collision. However, this effect is not nearly as strong as the former, "vacuum" effect.

The simulation behaves in a similar manner at higher densities and attempts at deriving analytical results, using a similar model to that presented here, were abandoned after it became clear that this model does not reproduce reverse osmosis.

7.7 An alternative explanation for reverse osmosis

The results from our toy 1D collision model suggest that two body collisions at the membrane are not responsible for the reverse osmosis that occurs in our MD simulations. We therefore turn to an alternative, many body explanation. We speculate that, because the solute particles have a higher kinetic energy, they exert a greater "pushing force" on the solvent particles which may cause them to cluster together. As a result, the solvent particles experience a higher local density in the solution compared to the average particle density. Because of this higher local density, in the presence of active solutes, solvent particles tend to move out of the solution – this leads to reverse osmosis

in our simulations. To test this hypothesis, we study the radial distribution function, $g(r)$, of the solvent particles in a mixed system of solvent + active particles. The radial distribution function is a measure for the local structure of the fluid, for further details see Section 2.2.2.

In Figure 7.11(a) I show the radial distribution function for the solvent particles in a bath containing a mixture of both solvent and active particles at a fixed concentration, but over several values for the solutes' activity. The shift in the peak of the $g(r)$ indicates that the solvent particles do indeed experience a higher local density due to the presence of active solute particles. To quantify this effect we compute the integral of the $g(r)$ to the first minimum, $I = \int_0^{r_{min.}} g(r)dr$ [58, 158]. For solids, I is related to the number of neighbours in the first shell around the central atom. Although this relation does not hold for liquids, it nevertheless provides useful information about the local density of the fluid.

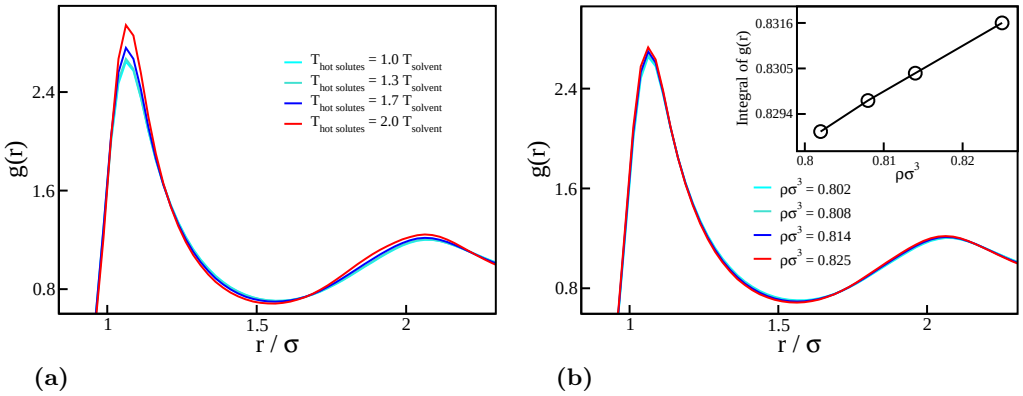

Figure 7.11 The radial distribution function for the solvent particles is shown as a function of increasing solute activity and total particle density for simulations of an active-passive bath and a completely passive bath of particles, respectively. In panel (a) results are shown for an active-passive mixture, in which the activity of the solute particles is varied for a fixed solute concentration, $c_u = 0.15\ \sigma^{-3}$. In panel (b) a passive bath of solvent only particles is simulated and the total density of particles is steadily increased. The inset to panel (b) shows the increase in the value of I (see main text) with increasing total particle density.

In comparison, Figure 7.11(b) shows a series of $g(r)$s for a purely passive system at different total densities. As the density increases, the peak in the $g(r)$ increases, as does the integral I (see the inset to Figure 7.11(b)). By mapping the value of I in a mixture of solvent + active particles to an equivalent value of I in a passive system, we can quantify the effective local density for solvent particles in the active-passive mixture. We anticipate that the active osmotic system will reach a steady state such that the effective local density of solvent in the solution is equivalent to what it would

be in the passive case (with the same concentration of solute particles).

To this end, we compute the steady-state value of I for a passive system at a total particle density equivalent to that of the solution compartment in our passive osmosis simulations (at a specified solute concentration). From our simulations of the active-passive mixtures we then determine the solvent density that corresponds to this value of I in the active case. According to our hypothesis this should correspond to the steady-state solvent density in the solution in the active case. This prediction can then be compared to the results from the MD simulations of the active osmotic system. Figure 7.12 shows the results for the density imbalance across the membrane as a function of increasing solute activity (at fixed solute concentrations) in (a) and as a function of solute concentration (at a fixed activity) in (b). Firstly, we note that the prediction for the density imbalance indeed leads to reverse osmosis, as demonstrated by the negative values of $\Delta\rho_{tot}$ recorded in Figure 7.12(a). Moreover, the qualitative agreement between the predictions from the $g(r)$ approach and the MD simulations is good. In panel (b) using the $g(r)$ approach even manages to reproduce the gradual decrease in reverse osmosis at higher solute concentrations. We speculate that this effect may be due to the break up of solvent clusters by more frequent collisions with active solutes at higher solute concentrations.

Thus, it appears that the reverse osmosis in our simulations is a result of the increased local density of solvent particles, driven by the activity of the solutes. This could also be viewed in terms of the solute particles exerting an active stress on the solvent particles (akin to an "internal piston") which drives them out of the solution.

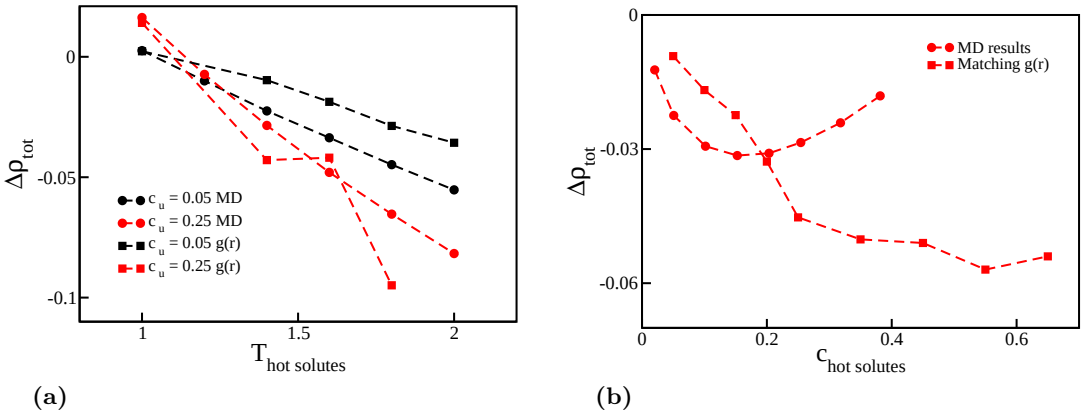

Figure 7.12 The predicted osmotic density imbalance across the membrane is shown in the MD simulations (as in Figure 7.8) and compared to the result obtained by matching the integral of the radial distribution functions of a passive bath at an elevated density (relative to the total density in the osmosis simulations, $\rho = 0.8\ \sigma^{-3}$) and an active bath at a reduced solvent density. In panel (a) results are shown versus the activity of the solute particles for two different solute concentrations. In panel (b) the same quantity is plotted as a function of the solute particle concentration.

7.8 Discussion

In this chapter we have demonstrated that active osmotic systems display qualitatively different behaviour from their equilibrium counterparts. In our simulations solute activity increases the osmotic pressure and, remarkably, can reverse the direction of the osmotic density imbalance. While the former effect can, in principle, be described by an "osmotic effective temperature", such a description cannot capture the latter effect, which is qualitatively distinct from the equilibrium case. A simple collision dynamics model, whilst it reproduces the elevated osmotic pressure, fails to reproduce the active osmotic density gradients. Thus, a simple picture, in which the active solute particles cause the solvent in the solution to experience a higher density than is actually present, has been proposed. By measuring the local density around the solvent particles, through integration of the radial distribution function to the first minimum, we showed that this argument can explain reverse osmosis in our system.

Our objective in this chapter was not to simulate a specific, experimentally realisable, active system, but rather to uncover the basic physical principles using the simplest possible, minimal model osmotic system. For this reason, we set the sizes, masses and interaction parameters of the solvent and solute equal and represented the membrane by a smooth confining potential. The fact that similar results are obtained for two

types of active particle suggests that the phenomena revealed in this study may be generic.

How relevant might these results be to realistic osmotic setups? Could active solutes be used in the desalination of water, as discussed in Section 1.4? There are clearly many differences between the models studied here and the experimentally realised active setups (*e.g.* Janus particles or laser-heated nanoparticles) discussed in the introduction to the chapter. Perhaps most obviously, the active particles in these setups are typically many orders of magnitude larger than the solvent molecules. Based on the work presented in this chapter it is not clear what effect the introduction of larger solute particles would have on the resulting dynamics of the solvent particles. A greater obstacle which stands in the way of possible technological developments using these ideas is the large amount of energy required to heat the solute molecules to a higher temperature than the surrounding solvent; how best to avoid heat conduction between the solute and solvent? It therefore appears that reverse osmosis by active solute particles probably does not currently provide a realistic alternative to current desalination methods.

Although not feasible as a method for the desalination of water, an active osmotic setup may be directly relevant for sifting colloidal systems containing a mixture of active and passive particles. Using such a setup, the passive colloids would assume the role of the solvent and the confinement of other "solute colloids" might be achieved, for example, using electric bottles [80, 81].

Finally, I note that there should be an interesting connection between the osmotic pressure and the active component of the stress in the Navier-Stokes equation. For polarised fields (such as in liquid crystals) the active stress can be measured as $\underline{\underline{\sigma}}^a = -\zeta c \vec{P}\vec{P}$, where ζ is the activity, c is the concentration and $\vec{P}$ is the polarisation of the active particles [59, 154]. In our case the polarisation is zero and we can simply write the active stress as $\underline{\underline{\sigma}}^a \propto -\zeta c \mathbb{1}$ [168]; the scalar pressure then follows from the trace of this relation. However, because the active component of the stress comprises a separate, additive term in the Navier-Stokes equation, we should be able to use our osmotic setup to deduce the value of this quantity in a very simple manner – by simply taking the difference between the active and the passive osmotic pressures.

Chapter 8

Conclusions

In this thesis molecular dynamics simulations have been used to study the fundamental processes which occur during osmosis. I now summarise the most salient results and discuss possible avenues for future work.

In Chapter 4 we began our study by exploring a fundamental virial relation for open systems, which we dubbed the "Schweitz virial relation." We demonstrated that, from this equation, two equations for the local pressure in an MD simulation could be derived. One of these relations was a well-known result; however, the derivation presented, suitable for scalar systems, was based on arguably simpler geometric considerations than the typical derivation. The second relation was new, but similar in spirit to the method of planes technique in that it considers the flux of momentum across a planar surface. Using MD simulations we tested our expressions for the local pressure, firstly in an open system, in which the local and global pressures were shown to be in excellent agreement, and further in an osmotic simulation, where the local pressure expressions were used to measure the osmotic pressure in our simulations. By generalising the Schweitz virial relation to a tensor form, it should be possible to extend on this work and derive the off diagonal components of the stress tensor. This would be of particular interest in systems which experience shear stresses.

In Chapter 5 we used a box in box, invisible membrane setup to study the steady-state properties of a minimal model for osmosis. Using liquid state theory we first confirmed that the results obtained for the density gradient and the osmotic pressure in our simulations using a WCA interaction potential were in good agreement with theoretical predictions for an equivalent hard sphere system. Next, a new formulation for the osmotic pressure, in terms of the various solute-solute and solute-solvent virial

contributions to the pressure, was derived and the nature of the individual terms in the resulting expression were analysed in both a WCA and a LJ system. The two systems demonstrated qualitatively similar behaviour and reproduced almost identical results for the osmotic pressure. Thus, we concluded that the repulsive part of the interaction in these simple systems dominates the osmotic behaviour of the system.

Using a simple, mechanical hopping model for the solvent particles at the membrane we derived a further expression for the steady-state osmotic pressure, similar to an existing expression which is usually derived from thermodynamic considerations. Our mechanical approach suggested that it is the balance between the net outward pushing force, due to the imbalance in the total density of particles at the membrane, and the net inward diffusive flux, due to the imbalance in the solvent density across the membrane, that produces the resulting steady-state density profile and osmotic pressure in our system. In realistic systems using porous membranes, more complicated processes such as solvent entrainment may play a very important role in determining the solvent dynamics in the periods prior to and during the steady state. To determine whether such processes were also at play in our simple model system we examined in detail the nature of the steady-state solvent crossings of the membrane, testing for such entrainment processes. However, no such processes were observed, leading us to conclude that they are not necessary for an understanding of osmosis at the most fundamental level.

It is interesting to point out that, as well as studying the fundamentals of osmosis, the osmotic setup introduced here could also be used to perform MD simulations in the grand canonical, μVT ensemble – by partitioning the system into a region of interest and a solvent reservoir, separated by a membrane barrier, invisible to the solvent. If realised this would be a useful tool, since grand canonical simulations are currently almost always conducted using the Monte Carlo simulation method [44]. Such an MD approach would be useful when one requires dynamical information about the particle trajectories. It would also avoid the need to perform a time-consuming Widom-type particle insertion/deletion scheme [44], as is required for μVT MC simulations. As well as providing a useful MD simulation tool, it is also interesting to consider how future simulations could be conducted in the context of power generation using the principles of osmosis. This is particularly topical given the urgent need for clean energy generation and the recent development of several methods for power generation that are based on osmosis. In particular, it would be of considerable interest to conduct realistic simulations which explore how altering the particle sizes and interaction parameters affects the resulting osmotic pressure, and therefore the total power which can be

generated in such schemes. I note that other authors have already used simulations to investigate the importance of the membrane and solute particle choice in determining the rate at which water flows across a semi-permeable membrane in the period prior to the steady state [130, 131]. Although these studies considered the rate of solvent flow in realistic systems, the underlying mechanism of the solvent flow prior to the steady state in osmosis remains the subject of some debate. In particular, the key factors which determine whether this flow is diffusive or faster than diffusive remain unaccounted for. To explore these effects further it is necessary to first develop a fundamental model for the solvent transfer in osmosis using a simple setup.

In Chapter 6 we proceeded along these lines, using a double box, finite membrane setup to study the solvent dynamics during the period prior to the steady state in osmosis. We found that the resulting solvent flow is not compatible with a model which treats the relaxation of the system to the steady state as a simple exponential process. Instead, the solvent dynamics were observed to be more interesting and a transition occurred in our system, particularly at higher solute concentrations, from an initial, faster rate of solvent transfer to a later, slower transport of solvent particles across the membrane. These results were reproduced in simulations of pressure-driven flows, where a chemical potential gradient was set up across the membrane by imposing an imbalance in the total density of particles across the membrane (but in which zero solute particles were placed). The equivalence of the two flows was demonstrated to be due to the establishment of similar pressure profiles across the barrier.

By studying the movement of labeled, tracer particles across the membrane we were able to derive a diffusive model, based on Kramers' theory, which captured the late-time dynamics of particle mixing in our simulations. Using a simple relation in terms of the fraction of tracer particles on either side of the membrane, we were further able to recover a result for the net solvent transfer across the membrane in our pressure-driven simulations according to Kramers' theory. Comparison of the theoretical prediction for the net movement of solvent particles with simulation data seemed to suggest that the late-time solvent dynamics in pressure-driven flows proceeds at a rate slower than expected by diffusion. It is likely that, to make further progress here, we must first re-examine Kramers' theory, in particular with respect to the determination of the transport coefficient for the tracer particles. Even in the purely diffusive simulations an interesting deviation in the solvent dynamics was observed at early times, where the solvent tracers appeared to cross the barrier in a non-diffusive manner.

Finally, in a novel modification to the osmotic system, we investigated how the physics

of osmosis changed when the solute particles in our osmosis simulations were made active. We found that using active solute particles increased the osmotic pressure and, by analogy with the van 't Hoff expression, we were able to define a new osmotic effective temperature that was in agreement with the diffusive temperature of the active particles. However, the usefulness of the concept of an osmotic effective temperature for mapping between an active osmotic system and an equivalent passive one appears doubtful. This is because simulations of active osmosis display qualitatively different behaviour to their passive counterparts. In particular, the active solute particles produce reverse osmosis – the expulsion of solvent particles from the solution prior to the steady state; a process which does not occur in equilibrium osmosis and so cannot be described by an osmotic effective temperature.

Using a model in which we postulated that the activity of the solute particles causes the solvent particles to experience a higher local density, we were able to explain the behaviour observed in our active simulations. In this picture, the active solute particles can be thought of as an internal piston, driving the system out-of-equilibrium. We further speculated on whether an osmotic system with active solutes could be used in industry, in the desalination of water, for example. However, considering the large amounts of energy required to maintain a temperature gradient in the system, between the solute and solvent particles, we concluded that this process is very likely less efficient than current technologies. An active osmotic setup could, however, be used for sifting a mixture of passive and active colloidal particles. Finally, I speculate that an osmotic setup could also be used to measure the chemical potential of the passive component of an active-passive mixture. This could provide a well-controlled method for investigating phase transitions in out-of-equilibrium active-passive mixtures.

Appendix A

Determining the error on the box in box, invisible membrane volume

In Section 3.2.2 the solution volume is determined by matching the pressure-density relation of a confined system of WCA (see Section 3.2.1) particles to that of an equivalent periodic system. Here, we make use of the fact that the inter-particle interaction is given by the WCA potential to determine the error on the position of the effective solution boundary. At low densities, the pressure of a WCA gas is essentially identical to that of a hard sphere gas, for which an accurate expression for the pressure is that of the Carnahan Starling (CS) equation of state [58]:

$$P = \rho k_B T \left(\frac{1 + \eta + \eta^2 - \eta^3}{(1-\eta)^3} \right). \tag{A.1}$$

In the above, ρ and η are the density and packing fraction ($= \frac{\pi}{6}\sigma^3\rho$) of the particles, and k_B and T are, as usual, Boltzmann's constant and the temperature, respectively. Before determining the error on the boundary of the solution we must first check the goodness of our 'fit-by-eye" procedure to ensure that the fitted, confined data matches the underlying CS relation as well as the periodic data does. To do this we first generate two new distributions made up of (1) the differences between the CS relation and the pressure of the (fitted) confined gas, X_c, and (2) an equivalent distribution for the periodic case, denoted X_p. The level of agreement of the two samples is then compared by means of a $t-test$ [22]. The t value for the two samples can be calculated as follows:

$$t = \frac{\bar{X_c} - \bar{X_p}}{s_{\bar{X_c}-\bar{X_p}}}, \tag{A.2}$$

where the over-bar denotes the mean of the sample and $s_{\bar{X_c}-\bar{X_p}} = \sqrt{s^2_{pooled}(\frac{1}{n_c} + \frac{1}{n_p})}$ compares the samples' variances. The t value as determined through Eq.(A.2) is then tested to ensure the two results are within statistical agreement, *i.e.* that the t value determined through Eq.(A.2) is less than the t value associated with the null hypothesis[1]. In our case, the t value determined through comparison of the two distributions is $t = 0.74$, whereas that associated with the null hypothesis is $t = 2.16$. An upper and lower bound are now placed on the effective solution boundary by varying the volume definition, such that the confined gas pressure shifts to the left and the right in Figure 3.7(a), until the t value as calculated by Eq.(A.2) is larger than $t = 2.16$. This occurs at $L_{solution} = 9.10$ and $L_{solution} = 9.28$, resulting in an effective boundary, with associated errors, of $0.91^{+0.07}_{-0.02}\sigma$.

[1]Determined from the samples' degrees of freedom ($n_{dof} = n_c + n_p - 2 = 13$) and a decision criterion, set here to 0.05.

Appendix B

Computing the prefactor (C) in Kramers' theory for the diffusive flux of tracers across a finite barrier

Our goal in this section is to demonstrate that the prefactor C in Eq.(6.5) can, assuming a diffusive transfer of solvent, be expressed as $C = \lambda_d L \mathrm{e}^{-\mu^{ex}(\rho)}/2\rho\Lambda^3$, where λ_d is the value that λ_t in Eq.(6.3) takes under the purely diffusive transport of solvent across the membrane, L is the length of the solution/solvent compartment, $\mu^{ex}(\rho)$ corresponds to the excess part of the chemical potential and ρ is the average density in the system $(= (\rho_L(t) + \rho_R(t))/2)$. We begin by considering a similar setup to the tracer diffusion experiment described Section 6.5.2, *i.e.* an equivalent density of solvent particles are initially placed (in the absence of solutes) on either side of the dividing barrier in our double box, finite membrane setup. We subsequently label all of the particles on the LHS of the membrane as tracer particles and record the fraction of the particles on the LHS which are tracers, which we denote $\phi_L(t)$, over the course of the simulation. Thus, $\phi_L^0 = 1.0$, where the 0 denotes $t = 0$, and in the steady state the tracers spread themselves evenly across the membrane, such that $\phi_L^{ss} = 0.5$. Starting from Eq.(6.7) and writing the flux, $j(t) \sim -d(L\rho\phi_L(t))/dt$, where ρ is a constant (equal densities exist on either side of the membrane) and L is the length of the solution/bath compartment, we can establish the following relation for the rate of change of $\phi_L(t)$ as a function of time:

$$\frac{d\phi_L(t)}{dt} = -\frac{C\Lambda^3\rho \mathrm{e}^{\mu^{ex}(\rho)}}{L}\left[2\phi_L(t) - 1\right]. \tag{B.1}$$

In Eq.(B.1) we have taken $\mu^{ex}_{L/R}(\rho_{L/R}) \to \mu^{ex}(\rho)$, where $\mu^{ex}_{L/R}(\rho_{L/R})$ is the excess part of the chemical potential on the left/right hand side of the membrane. The solution to Eq.(B.1) is

$$\phi_L(t) = \frac{1}{2}\left(1 + \mathrm{e}^{-\frac{2C\Lambda^3\rho \mathrm{e}^{\mu^{ex}(\rho)}}{L}t}\right). \tag{B.2}$$

For this purely diffusive case we expect the fraction of particles on the LHS that are tracers to decay as an exponential, $\phi_L(t) = \phi_L^{ss} - (\phi_L^{ss} - \phi_L^0)\mathrm{e}^{-\lambda_d t}$. Using the values for ϕ_L^0 and ϕ_L^{ss} stated above, we arrive at the following result for $\phi_L(t)$:

$$\phi_L(t) = \frac{1}{2}\left(1 + \mathrm{e}^{-\lambda_d t}\right). \tag{B.3}$$

Therefore, a simple comparison of relations B.2 and B.3 allows us to establish that the prefactor C from Eq.(6.5) can be expressed as

$$C = \frac{\lambda_d L}{2\rho\Lambda^3}\mathrm{e}^{-\mu^{ex}(\rho)}, \tag{B.4}$$

as required.

Bibliography

[1] Achilli, A., T. Y. Cath, and A. E. Childress. "Power generation with pressure retarded osmosis: an experimental and theoretical investigation." *J. Mem. Science* 343: (2009) 42–52.

[2] Achilli, A., and A. E. Childress. "Pressure retarded osmosis: from the vision of sidney Loeb to the first prototype installation - review." *Desalinisation* 261: (2010) 205–211.

[3] Alexander, G. P., and J. M. Yeomans. "Dumb-bell swimmers." *Euro. Phys. Lett.* 83: (2008) 34,006.

[4] Allen, M. P., and D. Tildesley. *Computer Simulation of Liquids.* Oxford University Press, 1992.

[5] Allen, R., S. Melchionna, and J. P. Hansen. "Intermittent permeation of cylindrical nanopores by water." *Phys. Rev. Lett.* 89: (2002) 175,501.

[6] Andersen, H. C. "Molecular dynamics simulations at constant pressure and/or temperature." *J. Chem. Phys.* 72: (1979) 2384–2393.

[7] Atzberger, P. J., and P. R. Kramer. "Theoretical framework for microscopic osmotic phenomena." *Physical review. E, Statistical, nonlinear, and soft matter physics* 75: (2007) 061,125.

[8] Barrat, J. L., and J. P. Hansen. *Basic concepts for simple and complex fluids.* Cambridge, UK: Cambridge University Press, 2003.

[9] Berezhkovskii, A., and G. Hummer. "Single-file transport of water molecules through a carbon nanotube." *Phys. Rev. Lett.* 89: (2002) 064,503.

[10] Boon, N., and R. van Roij. ""Blue energy" from ion adsorption and electrode charging in sea and river water." *Molecular Physics* 109, 7-10: (2011) 1229–1241.

[11] Brady, J. F. "Brownian motion, hydrodynamics, and the osmotic pressure." *J. Chem. Phys* 98, 4: (1993) 3335–3341.

[12] Braein, S., O. S. Sandvik, and S. E. Skilhagen. "Osmotic power. From prototype to industry - what will it take?" In *International conference on ocean energy.* 2010.

[13] Brogioli, D. "Extracting renewable energy from a salinity difference using a capacitor." *Phys. Rev. Lett.* 103: (2009) 058,501.

[14] von Brucke, E. W. "Beitraege zur Lehre von der Diffusion tropfbarfluessiger Koerper durch poroese Scheidewaende." *Ann. der Phys.* 134: (1843) 77–94.

[15] Cannon, J. "The influence of ion size and charge on osmosis." *J. Phys. Chem. B* 116, 14: (2012) 4206–4211.

[16] Carnahan, N. F., and K. E. Starling. "Equation of state for nonattracting rigid spheres." *J. Chem. Phys.* 51: (1969) 635–636.

[17] Cates, M. E. "Diffusive transport without detailed balance in motile bacteria: Does microbiology need statistical physics?" *Rep. Prog. Phys.* 75: (2012) 042,601.

[18] Chakraborty, D., M. V. Gnann, D. Rings, J. Glaser, F. Otto, F. Cichos, and K. Kroy. "Generalised Einstein relation for hot Brownian motion." *Euro. Phys. Lett.* 96: (2011) 60,009.

[19] Cheung, P. S. Y. "On the calculation of specific heats, thermal pressure coefficients and compressibilities in molecular dynamics simulations." *Mol. Phys.* 33: (1977) 519–526.

[20] Chinard, F. P. "Derivation of an experssion for the rate of formation of Glomerular Fluid (GFR). Applicability of certain physical and physico-chemical concepts." *Am. J. Physiol.* 171: (1952) 578–586.

[21] Chou, T. "Kinetics and thermodynamics across single-file pores: solute permeability and rectified osmosis." *J. Chem. Phys.* 110: (1998) 606–615.

[22] Clarke, G. M., and D. Cooke. *A basic course in statistics.* Arnold Publishers, 1998.

[23] Clausius, R. "On a mechanical theorem applicable to heat." *The London, Edinburgh and Dublin Philosophical Magazine and journal of science* 40: (1870) 122–127.

[24] Cooley, H., P. H. Gleick, and G. Wolff. *Desalination with a grain of salt.* Alonzo Printing Co., 2006.

[25] Cordova-Figueroa, U. M., and J. F. Brady. "Osmotic propulsion: the osmotic motor." *Phys. Rev. Lett.* 100: (2008) 158,303.

[26] Cormier, J., R. J. M., and D. T. J. "Stress calculations in atomistic simulations of perfect and imperfect solids." *J. App. Phys.* 89: (2001) 99–104.

[27] D. Loi, S. M., and L. F. Cugliandolo. "Effective temperature of active matter." *Phys Rev. E* 77: (2008) 051,111.

[28] Dainty, J. *Advances in Botanical Research*, volume 1. London: Academic Press, 1963.

[29] ———. "Osmotic flow." *Symp. Soc. Exp. Biol.* 19: (1965) 75–85.

[30] Dick, D. A. "Osmotic properties of living cells." *Int. Rev. Cytol.* 8: (1959) 387–448.

[31] Dudko, O. K., G. Hummer, and A. Szabo. "Theory, analysis, and interpretation of single-molecule force spectroscopy experiments." *Proc. Nat. Acad. Sci.* 105: (2008) 15,755–15,760.

[32] Durbin, R. P., F. H., and S. A. K. "Water flow through frog gastric mucosa." *J. Gen. Physiol.* 39: (1956) 535–551.

[33] Dutrochet, H. "Nouvelles observations sur l'endosmose et l'exosmose, et sur la cause de ce double phenomene." *Ann. Chim. Phys.* 35, 393.

[34] ———. "De l'endosmose des acides." *Ann. Chim. Phys.* 60, 337.

[35] ———. *Memoires for the service of the anatomical and physiological history of plants and animals.* J. B. Balliere, 1837.

[36] Ebbens, S., R. A. L. Jones, A. J. Ryan, R. Golestanian, and J. Howse. "Self-assembled autonomous runners and tumblers." *Phys Rev. E* 82: (2010) 015,304.

[37] Efron, B. "Bootstrap methods: another look at the jackknife." *Ann. Stat.* 7: (1979) 1–26.

[38] Efron, B., and R. Tibshirani. *An introduction to the bootstrap.* CRC, 1993.

[39] Erpenbeck, J. J., and W. W. Wood. "Molecular dynamics techniques for hard-core systems." *Modern theoretical chemistry* 6: (1977) 1–39.

[40] Ferrier, J. "Osmosis and intermolecular force." *J. Theor. Biol.* 106: (1984) 449.

[41] Fick, A. "Ueber diffusion." *Ann. der Phys.* 170, 1: (1855) 59–86.

[42] Finkelstein, A. "Water movement through lipid bilayers, pores, and plasma membranes theory and reality." John Wiley & Sons, 1987. Distinguished Lecture Series of the Society of General Physiologists Volume 4.

[43] Flekkoy, E. C., J. Feder, and T. Jossang. "Lattice gas simulations of osmosis." *J. Stat. Phys.* 68: (1992) 515–532.

[44] Frenkel, D., and B. Smit. *Understanding Molecular Simulation.* San Diego: Academic Press, 2002.

[45] de Gennes, P.-G. "Soft matter (Nobel Lecture)." *Ang. Chem.* 31: (1992) 842–845.

[46] Gibbs, J. W. "Semi-permebale films and osmotic pressure." *Nature* 55, 1429: (1897) 461–462.

[47] Golestanian, R. "Collective behaviour of thermally active colloids." *Phys. Rev. Lett.* 108: (2012) 038,303.

[48] Golestanian, R., T. B. Liverpool, and A. Ajdari. "Propulsion of a molecular machine by asymmetric distribution of reaction products." *Phys Rev. Lett.* 94: (2005) 220,801.

[49] ———. "Designing phoretic micro- and nano-swimmers." *New J. Phys.* 9: (2007) 1367–2630.

[50] Golestanian, R., and A. Najafi. "Simple swimmer at low Reynolds number: three linked spheres." *Phys Rev. E* 69: (2004) 062,901.

[51] Graham, T. "On the adsorption and dialytic separation of gases by colloid septa." *Philos. Mag.* 32, 218: (1866) 401–420.

[52] Greenlee, L. F., D. F. Lawler, B. D. Freeman, B. Marrot, and P. Moulin. "Reverse osmosis desalination: water sources, technology, and todays challenges." *Water Research* 43: (2009) 2317–2348.

[53] Guell, D. C. *The physical mechanism of osmosis and osmotic pressure; a hydrodynamic theory for calculating the osmotic reflection coefficient.* Ph.D. thesis, Massachusetts Institute of Technology, 1991.

[54] Guell, D. C., and H. Brenner. "Physical mechanism of membrane osmotic phenomena." *Ind. Eng. Chem. Res.* 35: (1996) 3004–3014.

[55] Hairer, E., C. Lubich, and G. Wanner. *Geometric numerical integration: structure preserving algorithms for ordinary differential equations.* Springer, 2002.

[56] Hammel, H. T. "Forum on osmosis I. Osmosis: diminished solvent activity or enhanced solvent tension?" *Am. J. Physiol.* 237: (1979) R95–107.

[57] ———. "Forum on osmosis V: Epilogue." *Am. J. Physiol.* 237: (1979) R123–125.

[58] Hansen, J. P., and I. R. McDonald. *Theory of simple liquids.* Elsevier, 2007, 3 edition.

[59] Hatwalne, Y., S. Ramaswamy, M. Rao, and R. A. Simha. "Rheology of active particle suspensions." *Phys. Rev. Lett.* 92: (2004) 118,101.

[60] Hevesy, G., E. Hofer, and A. Krogh. "The permeability of the skin of frogs to water as determined by D20 and H20." *Skand. Archiv. Physiol.* 72: (1935) 199–214.

[61] Hildebrand, J. H. "Forum on osmosis II: A criticism of solvent tension in osmosis." *Am. J. Physiol.* 237: (1979) R108–109.

[62] van't Hoff, J. H. "Die Rolle der osmotischen druckes in der Analogie zwischen Loesungen und Gasen." *Z. Phys. Chem.* 1: (1887) 481–508.

[63] Holt, J. K., H. G. Park, Y. Wang, M. Stadermann, A. B. Artyukhin, C. P. Grigoropoulos, A. Noy, and O. Bakajin. "Fast mass transport through sub-2-nanometer carbon nanotubes." *Science* 312: (2006) 1034–1037.

[64] Hoover, W. G. "Canonical dynamics: equilibrium phase space distributions." *Phys. Rev. A* 31: (1984) 1695–1697.

[65] Howse, J., R. A. L. Jones, A. J. Ryan, T. Gough, R. Vafabakhsh, and R. Golestanian. "Self-motile colloidal particles: from directed propulsion to random walk." *Phys. Rev. Lett.* 99: (2007) 048,102.

[66] Irving, J. H., and J. G. Kirkwood. "The statisitcal mechanical theory of transport processes IV. The equations of hydrodynamics." *J. Chem. Phys.* 18: (1950) 817–829.

[67] Itano, T., T. Akinaga, and M. Sugihara-Seki. "Molecular dynamics study of solvent transport in nanoscale osmosis." *J. Phys. Soc. Jpn.* 77: (2008) 064,605.

[68] Jiang, H.-R., N. Yoshinaga, and M. Sano. "Active motion of a Janus particle by self-thermophoresis in a defocused laser beam." *Phys Rev. Lett.* 105: (2010) 268,302.

[69] Joly, L., S. Merabia, and J.-L. Barrat. "Effective temperatures of a heated Brownian particle." *Euro. Phys. Lett.* 94: (2011) 50,007.

[70] Kalra, A., S. Garde, and G. Hummer. "Osmotic water transport through carbon nanotube membranes." *PNAS* 100, 18: (2003) 10,175–10,180.

[71] Kapral, R. "Perspective: Nanomotors without moving parts that propel themselves in solution." *J. Chem. Phys.* 138: (2013) 020,901.

[72] Kedem, O., and A. Katchalsky. "Thermodynamic analysis of the permeability of biological membranes to non-electrolytes." *Biochimica et Biophysica Acta* 27: (1958) 229–246.

[73] ———. "A physical interpretation of the phenomenological coefficients of membrane permeability." *J. Gen. Physiol.* 45: (1961) 143–179.

[74] Kiil, F. "Mechanism of osmosis." *Kidney International* 21: (1982) 303–308.

[75] ———. "Molecular mechanisms of osmosis." *Am. J. Physiol.* 256: (1989) R801–808.

[76] Kim, K. S., I. S. Davis, P. A. Macpherson, T. J. Pedley, and A. E. Hill. "Osmosis in small pores: a molecular dynamics study of the mechanism of solvent transport." *Proc. R. Soc. A* 461: (2005) 273–296.

[77] Koefoed-Johnsen, V., and H. H. Ussing. "The contributions of diffusion and flow to the passage of D2O through living membranes." *Acta Physiol. Scand.* 28, 1: (1953) 60–76.

[78] Kramers, H. A. "Brownian motion in a field of force and the diffusion model of chemical reactions." *Physica* 7: (1940) 284–304.

[79] Leimkuhler, B., E. Noorizadeh, and F. Theil. "A gentle stochastic thermostat for molecular dynamics." *J. Stat. Phys.* 135: (2009) 261–277.

[80] Leunissen, M. E., and A. van Bladeren. "Concentrating colloids with electric field gradients. II. Phase transitions and crystal buckling of long-ranged repulsive charged spheres in an electric bottle." *J. Chem. Phys.* 128: (2008) 164,509.

[81] Leunissen, M. E., M. T. Sullivan, P. M. Chaikin, and A. van Blaaderen. "Concentrating colloids with electric field gradients. I. Particle transport and growth mechanism of hard-sphere-like crystals in an electric bottle." *J. Chem. Phys.* 128: (2008) 164,508.

[82] Levitt, D. G. "Kinetics of diffusion and convection in 3.2øA pores." *Biophys. J.* 13: (1973) 186–206.

[83] Lion, T. W., and R. J. Allen. "Computing the local pressure in molecular dynamics simulations." *J. Phys. Condens. Matter* 24: (2012) 284,133.

[84] ———. "Osmosis in a minimal model system." *J. Chem. Phys.* 137: (2012) 244,911.

[85] Loeb, S., 1975.

[86] Loi, D., S. Mossa, and L. F. Cugliandolo. "Non-conservative forces and effective temperatures in active polymers." *Soft Matter* 7: (2011) 10,193–10,209.

[87] Luo, Y., and B. Roux. "Simulation of osmotic pressure in concentrated aqueous salt solutions." *J. Phys. Chem. Lett.* 1: (2010) 183–189.

[88] Lutsko, J. F. "Stress and elastic constants in anisotropic solids: Molecular dynamics techniques." *J. App. Phys.* 64: (1988) 1152–1154.

[89] Martyna, G. J., and M. L. Klein. "Nose-Hoover chains: The canonical ensemble via continuous dynamics." *J. Chem. Phys.* 97, 4: (1992) 2635–2643.

[90] Martyna, G. J., D. J. Tobias, and M. L. Klein. "Constant pressure molecular dynamics algorithms." *J. Chem. Phys* 101, 5: (1994) 4177–4189.

[91] Mason, E. A. "From pigs bladders and cracked jars to polysulfones: an historical perspective on membrane transport." *J. Mem. Sci.* 60: (1991) 125–145.

[92] Mauro, A. "Nature of solvent transfer in osmosis." *Science* 126: (1957) 252–253.

[93] ———. "Some properties of ionic and nonionic semipermeable membranes." *Circulation* 21: (1960) 845–854.

[94] ———. "Forum on osmosis III. Comments on Hammel and Scholander's solvent tension theory and its application to the phenomenon of osmotic flow." *Am. J. Physiol.* 237: (1979) R110–113.

[95] MCCandlish, S. R., A. Baskaran, and M. F. Hagan. "Spontaneous segregation of self-propelled particles with different motilities." *Soft Matter* 8: (2012) 2527–2534.

[96] McMillan, W. G., and J. E. Mayer. "The statistical mechanics of multicomponent systems." *J. Chem. Phys.* 13, 7: (1945) 276–305.

[97] Meir, E., J. Perry, D. Stal, S. Maruca, and E. Klopfer. "How effective are simulated molecular-level experiments for teaching diffusion and osmosis?" *Cell Biol. Educ.* 4: (2005) 235–248.

[98] Mendelev, M. I., S. Han, D. J. Srolovitz, G. J. Ackland, D. Y. Sun, and M. Asta. "Development of new interatomic potentials appropriate for crystalline and liquid iron." *Philos. Mag.* 83: (2003) 3977–3994.

[99] Merabia, S., S. Shenogin, L. Joly, P. Keblinski, and J.-L. Barrat. "Heat transfer from nanoparticles: a corresponding state analysis." *Proc. Nat. Acad. Sci.* 106: (2009) 15,113–15,118.

[100] Mishra, S., A. Baskaran, and M. C. Marchetti. "Fluctuations and pattern formation in self-propelled particles." *Phys Rev. E* 81: (2010) 061,916.

[101] Montague, C. L., and J. A. Ley. "A possible effect of salinity fluctuation on abundance of benthic vegetation and associated fauna in Northeastern Florida Bay." *Estuaries* 16: (1993) 703–717.

[102] Morse, H. N. "The osmotic pressure of aqueous solutions." Technical report, John Hopkins University, 1914.

[103] Murad, S., and J. G. Powles. "A computer simulation of the classic experiment on osmosis and osmotic pressure." *J. Chem. Phys.* 99, 9: (1993) 7271–7272.

[104] Murad, S., J. G. Powles, and B. Holtz. "Osmosis and reverse osmosis in solutions: Monte Carlo simulations and van der Waals one-fluid theory." *Molecular Physics* 86, 6: (1995) 1473–1483.

[105] Murad, S., and J. Powles. "Computer simulation of osmosis and reverse osmosis in solutions." *Chemical Physics Letters* 225: (1994) 437–440.

[106] Nardi, J., R. Bruinsma, and E. Sackmann. "Vesicles as osmotic motors." *Phys. Rev. Lett.* 82: (1999) 5168–5171.

[107] Nijmeijer, M. J. P., A. F. Bakker, C. Bruin, and J. H. Sikkenk. "A molecular dynamics simulation of the Lennard-Jones liquid-vapour interface." *J. Chem. Phys.* 89: (1988) 3789–3792.

[108] Nollet, A. *Leçons de physique expérimentale*, volume v. 1 - 6 of *Leçons de physique expérimentale*. Durand, neveu, 1743-1748.

[109] Norman, R. S. "Water salination: a source of energy." *Science* 186: (1974) 350–352.

[110] Nose, S. "A molecular dynamics method for simulation in the canonical ensemble." *Mol. Phys.* 52: (1984) 255–268.

[111] ———. "A unified formulation of the constant temperature molecular dynamics methods." *J. Chem. Phys.* 81, 1: (1984) 511–519.

[112] Park, P. J., and W. Sung. "Dynamics of a polymer surmounting a potential barrier: The Kramers problem for polymers." *J. Chem. Phys.* 111: (1999) 5259–5266.

[113] Pattle, R. E. "Production of electric power by mixing fresh and salt water in the hydroelectric pile." *Nature* 174: (1954) 660.

[114] Paxton, W. F., K. C. Kistler, C. C. Olmeda, A. Sen, S. K. S. Angelo, Y. Cao, T. E. Mallouk, P. E. Lammert, and V. H. Crespi. "Autonomous movement of striped nanorods." *J. Am. Chem. Soc.* 126: (2004) 13,424–13,431.

[115] Pfeffer, W. "Ueber chemotaktische Bewegungen von Bakterien, Flagellaten und Volvocineen." *Untersuch. Bot. Inst. Tuebingen* 2: (1888) 582–663.

[116] ———. *Osmotische untersuchungen: studien zur zellmechanik*. Van Nostrand Reinhold Co., 1921.

[117] Poon, W. "Colloids as big atoms." *Science* 304: (2004) 830–831.

[118] Post, J. W., C. H. Goeting, J. Valk, S. Goinga, J. Veerman, H. V. M. Hamelers, and P. J. F. M. Hack. "Towards implementation of reverse electrodialysis for power generation from salinity gradients." *Desalinisation and Water Treatment* 16: (2010) 182–193.

[119] Post, J. W., J. Veerman, H. V. Hamelers, G. J. Euverink, S. J. Metz, K. Nymeijer, and C. J. Buisman. "Salinity-gradient power: evaluation of pressure-retarded osmosis and reverse electrodialysis." *J. Mem. Science* 288: (2007) 218–230.

[120] Powles, J. G., B. Holtz, W. A. B. Evans, and S. Murad. "Can osmotic pressure be negative?" *Molecular Physics* 90, 4: (1997) 665–670.

[121] Powles, J. G., S. Murad, and B. Holtz. "A novel pressure route to the activity coefficient of a molecule in a solution." *Chem. Phys. Letters* 245: (1995) 178–182.

[122] Powles, J., and S. Murad. "The simulation of semi-permebale membranes - osmosis, reverse osmosis and electro-osmosis in electrolyte solutions." *Journal of Molecular Liquids* 78: (1998) 225–231.

[123] Prescott, D. M., and E. Zeuther. "Comparison of water diffusion and water filtration across surfaces." *Acta Physiol. Scand.* 28: (1953) 77–94.

[124] Press, W. H., S. A. Teukolsky, W. T. Vetterling, and B. P. Flannery. *Numerical recipes*. Cambridge University Press, 2007, 3rd edition.

[125] Purcell, E. "Life at low Reynolds Number." *Am. J. of Phys.* 45: (1977) 3–11.

[126] Qin, J.-J., K. A. Kekre, G. Tao, M. H. Oo, M. N. Wai, T. C. Lee, B. Viswanath, and H. Seah. "New option of MBR-RO process for production of NEWater from domestic sewage." *J. Mem. Science* 272: (2006) 70–77.

[127] Quenouille, M. H. "Approximate tests of correlation in time-series." *J. Roy. Stat. Soc. B* 11: (1949) 68–84.

[128] ———. "Notes on bias estimation." *Biometrika* 43: (1956) 353–360.

[129] Radunz, R., D. Rings, K. Kroy, and F. Cichos. "Hot Brownian particles and photothermal correlation spectroscopy." *J. Phys. Chem. Lett. A* 113: (2009) 1674–1677.

[130] Raghunathan, A. V., and N. R. Aluru. "Effect of size-asymmetric electrolyte on single file osmosis." *App. Phys. Lett.* 89: (2006) 064,107.

[131] ———. "Molecular understanding of osmosis in semipermeable membranes." *Phys. Rev. Lett.* 97: (2006) 024,501.

[132] Ray, P. M. "On the theory of water movement." *Plant Physiol.* 35: (1960) 783–795.

[133] Rings, D., M. Selmke, F. Cichos, and K. Kroy. "Theory of hot Brownian motion." *Soft Matter* 7: (2011) 3441–3452.

[134] Rings, D., R. Schachoff, M. Selmke, F. Cichos, and K. Kroy. "Hot Brownian motion." *Phys Rev. Lett.* 105: (2010) 090,604.

[135] Ruckner, G., and R. Kapral. "Chemically powered nanodimers." *Phys. Rev. Lett.* 98: (2007) 150,603.

[136] Russel, W. B., D. A. Saville, and W. R. Schowalter. *Colloidal dispersions*. Cambridge University Press, 1989.

[137] Sasson, S. A., and N. B. Grover. "Osmosis: A macroscopic phenomenon, a microscopic view." *Advances in Physiology Education* 27, 1: (2003) 15–19.

[138] Schindler, M. "A numerical test of stress correlations in fluctuating hydrodynamics." *Chemical Physics* 375: (2010) 327–336.

[139] Schrader, M., P. Virnau, D. Winter, T. Zykova-Timan, and K. Binder. "Methods to extract interfacial free energies of flat and curved interfaces from computer simulations." *Eur. Phys. J.* 177: (2009) 103–127.

[140] Schweitz, J. "A classical virial theorem for open systems." *J. Phys. A: Math. Gen.* 10, 4: (1977) 507–515.

[141] Seminara, A., T. E. Angelini, and J. N. W. et al. "Osmotic spreading of Bacillus subtilis biofilms driven by an extracellular matrix." *Proc. Nat. Acad. Sci.* 109: (2012) 1116–1121.

[142] Sigg, D., H. Qian, and F. Bezanilla. "Kramers diffusion theory applied to gating kinetics of voltage-dependent ion channels." *Biophys. J.* 76: (1999) 782–803.

[143] Siria, A., P. Poncharal, A.-L. Biance, R. Fulcrand, X. Blase, S. T. Purcell, and L. Bocquet. "Giant osmotic energy conversion measured in a single transmembrane boron nitride nanotube." *Nature* 494: (2013) 455–458.

[144] Skilhagen, S. E., J. E. Dugstad, and R. J. Aaberg. "Osmotic power - power production based on the osmotic pressure difference between waters with varying salt gradients." *Desalinisation* 220: (2007) 476–482.

[145] Smith, E. B. *Basic Chemical Thermodynamics.* Academic Press, Oxford Science Publications, 1994.

[146] Soodak, H., and A. Iberall. "Osmosis, diffusion, convection." *Am. J. Physiol.* 235: (1978) R3–17.

[147] ———. "Forum on osmosis IV: More on osmosis and diffusion." *Am. J. Physiol.* 237: (1979) R114–122.

[148] Sotiriou, G. A., A. M. Hirt, P.-Y. Lozach, A. Teleki, F. Krumeich, and S. E. Pratsinis. "Hybrid, silica-coated, Janus-like plasmonic-magnetic nanoparticles." *Chem. Mater.* 23: (2011) 1985–1992.

[149] Starr, C., and B. McMilan. *Human Biology.* Cengage Learning, 2008.

[150] Su, J., and H. Guo. "Control of unidirectional transport of single-file water molecules through carbon nanotubes in an electric field." *ACS Nano* 5: (2011) 351–359.

[151] ———. "Effect of nanotube-length on the transport properties of single-file water molecules: transition from bidirectional to unidirectional." *J. Chem. Phys.* 134: (2011) 244,513.

[152] Suk, M. E., A. V. Raghunathan, and N. R. Aluru. "Fast reverse osmosis using boron nitride and carbon nanotubes." *App. Phys. Lett.* 92: (2008) 133,120.

[153] Theurkauff, I., C. Cottin-Bizonne, J. Palacci, C. Ybert, and L. Bocquet. "Dynamical clustering in active colloidal suspensions with chemical signalling." *Phys. Rev. Lett.* 108: (2012) 268,303.

[154] Tjhung, E., and M. E. Cates. "Nonequilibrium steady states in polar active fluids." *Soft Matter* 7: (2011) 7453–7464.

[155] Todd, B. D., D. J. Evans, and P. J. Daivis. "Pressure tensor for inhomogeneous fluids." *Phys. Rev. E* 52, 2: (1995) 1627–1638.

[156] Tombs, M. P., and A. R. Peacocke. *The osmotic pressure of biological macromolecules.* Oxford University Press, 1974.

[157] Traube, M. "Experimente zur Theorie der Zellbildung und Endosmose." *Archiv. Anat. Physiol. wiss Medicin* 87: (1867) 129–165.

[158] Vahvaselka, K. S., and J. M. Mangs. "X-Ray diffraction study of liquid sulfur." *Phys. Scripta* 38: (1988) 737–741.

[159] Valeriani, C., R. J. Allen, and D. Marenduzzo. "Non-equilibrium dynamics of an active colloidal chucker." *J. Chem. Phys.* 132: (2010) 204,904.

[160] Valeriani, C., M. Li, J. Novosel, J. Arlt, and D. Marenduzzo. "Colloids in a bacterial bath: simulations and experiments." *Soft Matter* 7: (2011) 5228–5238.

[161] Veerman, J., M. Saakes, S. J. Metz, , and G. J. Harmsen. "Electrical power from sea and river water by reverse electrodialysis: a first step from the laboratory to a real power plant." *Environ. Sci. Technol.* 44: (2010) 9207–9212.

[162] Vegard, L. "On the free pressure in osmosis." *Proc. Camb. Phil. Soc.* 15: (1908) 13–23.

[163] Vignais, P. V., and P. M. Vignais. *Discovering life, manufacturing life.* Springer, 2010.

[164] Warner, J. H. R. "Kinetic theory and rheology of dilute suspensions of finitely extendible dumbbells." *Ind. Eng. Chem. Fundam.* 11: (1972) 379–87.

[165] Weeks, J. D., D. Chandler, and H. C. Andersen. "Role of repulsive forces in determining the equilibrium structure of simple liquids." *J. Chem. Phys.* 54, 12: (1971) 5237–5247.

[166] Wiener, N. "Differential space." *J. Math. Phys. Soc.* 2: (1923) 131–174.

[167] ———. "The average value of a functional." *Proc. London Math. Soc.* 2: (1924) 454–467.

[168] Wolgemuth, C. W., J. Stajic, and A. Mogilner. "Redundant mechanisms for stable cell locomotion revealed by minimal models." *Biophys. J.* 101: (2011) 545–553.

[169] Wu, X.-L., and A. Libchaber. "Particle diffusion in a quasi-two-dimensional bacterial bath." *Phys Rev. Lett.* 84, 13: (2000) 3017–3020.

[170] Yates, F. E. "Osmosis: a transport of confusion." *Am. J. Physiol.* 235: (1978) R1.

[171] Ye, X., T. Narayanan, P. Tong, J. S. Huang, M. Y. Lin, B. L. Carvalho, and L. J. Fetters. "Depletion interactions in colloid-polymer mixtures." *Phys. Rev. E.* 54: (1996) 6500–6510.

[172] Yip, N. Y., and M. Elimelech. "Thermodynamic and energy efficiency analysis of power generation from natural salinity gradients by pressure retarded osmosis." *Environ. Sci. Technol.* 46: (2012) 5230–5239.

[173] Yoffe, A. "A proposal to investigate the molecular mechanism of osmosis in dense fluids.", 2005. Presented to UCLA Dept. of Chem. and BioChem. doctoral committe.